

**AD-A233 071**



2

GL-TR-90-0201

Title: Weather Radar Technology Development

Authors: F. Ian Harris, Ralph J. Donaldson, Jr., Paul Desrochers, Donald Hamann,  
and Teresa Bals

ST Systems Corporation (STX)  
109 Massachusetts Avenue  
Lexington, MA 02173

15 August 1990

Final Report  
Period Covered: May 16, 1987 to May 15, 1990

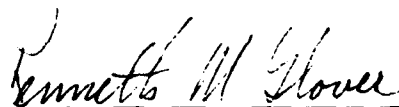
Approval for Public Release; Distribution Unlimited


Geophysics Laboratory  
Air Force Systems Command  
United States Air force  
Hanscom Air Force Base, Massachusetts 01731-5000

DTIC  
ELECTE  
MAR 15 1991  
S B D

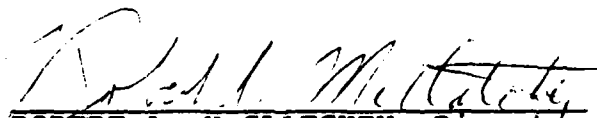
91 3 11 037

"This technical report has been reviewed and is approved for publication"

  
KENNETH M. GLOVER  
Contract Manager

  
KENNETH M. GLOVER, Chief  
Ground Based Remote Sensing Branch  
Atmospheric Sciences Division

FOR THE COMMANDER

  
ROBERT A. McCLATCHEY, Director  
Atmospheric Sciences Division

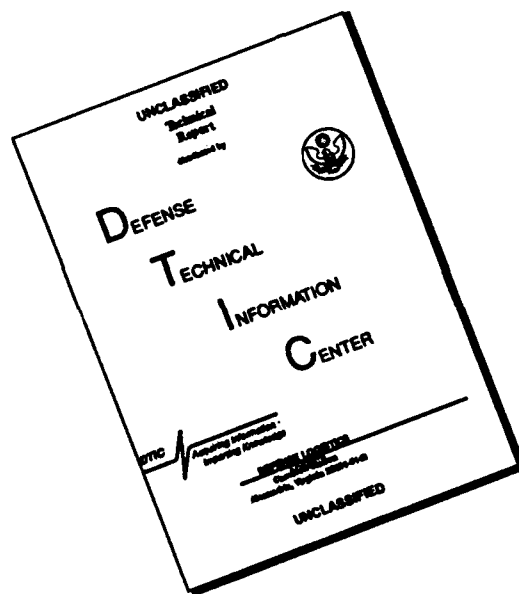
This report has been reviewed by the ESD Public Affairs Office (PA) and is releasable to the National Technical Information Service (NTIS).

Qualified requestors may obtain additional copies from the Defense Technical Information Center. All others should apply to the National Technical Information Service.

If your address has changed, or if you wish to be removed from the mailing list, or if the addressee is no longer employed by your organization, please notify GL/IMA, Hanscom AFB, MA 01731. This will assist us in maintaining a current mailing list.

Do not return copies of this report unless contractual obligations or notices on a specific document requires that it be returned.

# DISCLAIMER NOTICE



THIS DOCUMENT IS BEST QUALITY AVAILABLE. THE COPY FURNISHED TO DTIC CONTAINED A SIGNIFICANT NUMBER OF PAGES WHICH DO NOT REPRODUCE LEGIBLY.

# REPORT DOCUMENTATION PAGE

1. AGENCY USE ONLY		2. REPORT TYPE AND DATES COVERED	
15 August 1990		Final - May 16, 1987 to May 15, 1990	
4. TITLE AND SUBTITLE		5. AUTHOR(5)	
Weather Radar Technology Development		F. Ian Harris, Ralph J. Donaldson, Jr., Paul Desrochers, Donald Hamann, and Teresa Bals	
6. AUTHOR(5)		7. PERFORMING ORGANIZATION NAME(S) AND ADDRESS(ES)	
		ST Systems Corporation 109 Massachusetts Lexington, MA 02173	
8. PERFORMING ORGANIZATION REPORT NUMBER		9. SPONSORING/MONITORING AGENCY NAME(S) AND ADDRESS(ES)	
PE 63707F PR 2781 TA 01 WU AE Contract F19628-87-0124		Geophysics Laboratory Hanscom AFB, MA 01731-5000 Contract Manager: Kenneth Glover/LYR	
10. SPONSORING/MONITORING AGENCY REPORT NUMBER		11. SUPPLEMENTARY NOTES	
GL-TR-90-0201			
12a. DISTRIBUTION/AVAILABILITY STATEMENT		12b. DISTRIBUTION CODE	
Approved for public release; distribution unlimited			
13. ABSTRACT (Maximum 200 words)			
<p>Techniques have been developed to automatically analyze Doppler weather radar data to detect, assess, and predict weather that adversely affects Air Force operations. Focus has been on severe wind events associated with tornadic storms and hurricanes, wind shear events, large hail, and tracking of precipitation. The energetics of mesocyclones within severe storms have been estimated and used to improve the probability of detection and reduce the false alarm ratio for tornadoes and to discriminate storms producing violent, strong, or weak tornadoes. This rotational intensity and the divergence provide very good guidance in determining the potential of large hail production. Of several tested parameters, Potential-Vortex Fit has been found to accurately discriminate the behavior of hurricanes. This parameter is relatively insensitive to storm location. A new technique for gradient detection has been developed to detect synoptic scale fronts and gust fronts. It is also used with a contour extraction routine based on the Freeman Chain code to monitor and track precipitation regions. These techniques require further research. An efficient and effective two-dimensional velocity dealiasing technique has been developed that successfully treats more than 99% of the data.</p>			
14. SUBJECT TERMS		15. NUMBER OF PAGES	
Doppler radar, tornadoes, hurricanes, gust fronts, synoptic fronts, hail, mesocyclones, precipitation, velocity dealiasing, automated detection		102	
16. PRICE CODE		17. SECURITY CLASSIFICATION OF REPORT	
		Unclassified	
18. SECURITY CLASSIFICATION OF THIS PAGE		19. SECURITY CLASSIFICATION OF ABSTRACT	
Unclassified		Unclassified	
20. LIMITATION OF ABSTRACT		21. LIMITATION OF ABSTRACT	
Unlimited distribution			

## FOREWORD

This final Scientific Report details the results of research performed by ST Systems Corporation (STX) under Contract F19628-87-C-0124 with the Atmospheric Sciences Division, Geophysics Laboratory. this contract covered the period from May 16, 1987 to Aug. 15, 1990.

On overview approach has been taken since all work has been or is in the process of being documented in separate reports or papers. Copies of conference papers and journal articles have been included. However, Scientific Reports have not been included in the interest of conservation.

Personnel associated with this contract include:

Teresa M. Bals, MS

Paul R. Desrochers, MS

Ralph J. Donaldson, Jr, MS

Donald Hamann, BS

F. Ian Harris, PhD (Principle Investigator)



Accession For	
NTIS GRA&I	<input checked="" type="checkbox"/>
DTIC TAB	<input type="checkbox"/>
Unannounced	<input type="checkbox"/>
Justification	
By _____	
Distribution/	
Availability Codes	
Dist	Avail and/or Special
A-1	23

## TABLE OF CONTENTS

<b>FOREWORD</b>	iii
<b>1. INTRODUCTION</b>	<b>1</b>
a. Overview of Contract	1
b. Overview of Report	2
<b>2. THE ALGORITHMS</b>	<b>2</b>
a. Hurricane Severity	2
i. Long Range Detection	3
ii. Hurricane Intensity	4
b. Mesoscale Wind Discontinuity	6
i. Overview	6
ii. Gradient Computation	7
iii. Edge Extraction	8
iv. Streak Association	8
v. Results and Conclusions	9
c. Cloud and Precipitation Forecast	9
i. Analysis Techniques	12
(1) Contour extraction	12
(2) Edge Detection	13
(3) Feature Characterization	13
ii. Analysis	14
iii. Summary	14
d. Tornado Probability	16

e.	Hail Size Estimation . . . . .	19
	i. Analysis Techniques . . . . .	21
	(1) Upper-Level Divergence . . . . .	21
	(2) Rotational Kinetic Energy . . . . .	21
	(3) Divergence Profile . . . . .	22
	ii. Discussion . . . . .	22
f.	Velocity Dealiasing . . . . .	23
	i. The Dealiasing Technique . . . . .	24
	ii. Results . . . . .	25
	iii. Summary and Recommendations . . . . .	27
3.	OTHER ACTIVITIES . . . . .	28
4.	SUMMARY . . . . .	28
5.	REFERENCES . . . . .	29
	APPENDIX A. - List of Reports/Publications Produced under Contract .	33
	APPENDIX B: Conference Papers and Journal Articles Published Dur-	
	ing Contract. . . . .	36

## **1. INTRODUCTION**

### **a. Overview of Contract**

Under this contract, STX has conducted research involving the development and evaluation of automated Doppler weather radar based technologies to detect, assess, and predict severe weather. The purpose of this work is to provide forecasts in a responsive and accurate manner to enable timely precautionary measures for the protection of military resources. Results of this work are intended for automated implementation on radar systems such as the NEXt generation weather RADar (NEXRAD) system. Several research areas were addressed:

- \* Downburst Motions
- \* Hurricane Severity
- \* Mesoscale Wind Discontinuity
- \* Cloud and Precipitation Forecast
- \* Tornado Probability
- \* Hail Size Estimation
- \* Velocity Dealiasing

The first six of these are those originally proposed and results of the research in these areas were mostly outstanding. The one exception was



**Downburst Motions.** This algorithm has been treated extensively for some time by MIT/Lincoln Laboratory and the National Center for Atmospheric Research as part of the Terminal Doppler Weather Radar (TDWR) program of the Federal Aviation Administration (FAA). After examining this problem and reviewing recent progress made by these groups, it was concluded by STX that this area was being adequately addressed within the FAA program. In addition, another problem, that of velocity aliasing was presenting a serious impediment to the development of other algorithms and this problem was considered to be of sufficient importance to warrant further attention. Upon consultation with the GL technical monitor, it was agreed that Downburst Motions should not be pursued and that efforts should be directed toward the more pressing problem of velocity dealiasing.

**b. Overview of Report**

In this report, an overview of each task area will be given. For specific details the reader is referred to conference papers, journal articles, or separate technical reports that have been written on each of these areas. These have been listed in Appendix A and copies of all conference papers and journal articles are included in Appendix B.

**2. THE ALGORITHMS**

**a. Hurricane Severity**

The potential for routinely observing synoptic scale storm systems with Doppler radar will soon be realized with the deployment of the NEXRAD radar systems. Some of these large scale storms can have devastating wind conditions resulting in loss of life and property. Atlantic hurricanes, Pacific typhoons, and intense winter oceanic cyclones are notable examples of this

type of storm. The intent of this research effort has been to develop new techniques to allow the monitoring of the intensity of such systems. These systems present a unique problem as compared with the mesoscale systems in that their size and location usually preclude observation of the complete system. This meant that new, innovative monitoring techniques were required. The techniques that have been developed are discussed in detail in the papers listed in Appendix A. Copies of these papers are included in Appendix B.

A serious limitation in the development of such techniques is that there have been only a limited number of data sets that have been collected from such storms from ground-based radar systems. One notable data set was collected by the Air Force Geophysics Laboratory Doppler radar from Hurricane Gloria on September 27, 1985. Analysis of these data under this and a previous contract has resulted in the development of techniques to assess the characteristics of these storms (Donaldson and Harris, 1988, Donaldson and Ruggiero, 1986, Ruggiero and Donaldson, 1987, Donaldson, 1990). Another data source that has been exploited is the simulated data set generated by Wood and Brown (1987). They assimilated observational data and constructed a model flow and precipitation field that evolved and advected. These model data were obtained from Wood and Brown and were then used to generate simulated Doppler radar measurements.

#### i. Long Range Detection

The capability of Doppler radar for long-range detection of the maximum winds around a hurricane was examined through a simulation study by Harris et al. (1989). They used the hurricane model of Wood and Brown (1987) as outlined above. With these model data, simulated radar data were generated where the relative positions of the storm and radar were varied.

In addition, the pulse repetition frequency (PRF) was varied to allow the variation of the maximum unambiguous range and velocity. From these simulations Harris et al. found that long-range observations provide significant information on hurricane core winds, at least out to a range of 350 km, provided care is taken to assure that velocity observations are conducted in the first unambiguous range interval by appropriate reduction in the radar PRF. The ratio of observed core velocities to maximum hurricane winds just above the frictional boundary is 0.83 at a range of 250 km, 0.78 at 300 km, 0.63 at 350 km, but only 0.34 at 400 km distant. The decrease of observed velocity with increasing range is caused almost entirely by obstruction of lower altitudes by the earth's curvature and by the typical decrease of maximum winds with height above the boundary layer.

These results should be encouraging to forecasters who will use the NEXRAD radars which are soon to be installed along coasts prone to tropical cyclone activity. However, it should be noted that, to realize the potential for long-range observations in extensive storms, PRF flexibility is a necessary requirement to prevent the contamination of second-trip echoes by the much greater power of the first-trip echoes. The degree of flexibility that is required may not be available in the NEXRAD systems as deployed. Also, forecasters must have knowledge of the effects of beam size and beam height above ground at long ranges. The beam is centered at much greater altitudes than at close ranges and the beam yields means derived over altitude depths of the order of kilometers at long ranges versus hundreds of meters at close range. Both of these effects tend to bias velocity estimates toward lower values than are actually occurring in nature.

## ii. Hurricane Intensity

It may be desirable to estimate hurricane severity by sampling the

region of the hurricane beyond its core of maximum winds. A technique of this type could lend itself readily to trend analysis because it can be conducted at constant height and resolution. It should also be of particular benefit in monitoring the intensity of approaching hurricanes. Accordingly, a technique, potential-vortex fit, was proposed by Donaldson (1989) for determining the degree of conformity of the horizontal velocity structure in a sampled region outside the hurricane core with the flow field in a potential-vortex regime, wherein both curvature and tangential wind speed vary inversely with distance from a center. The technique uses the method given by Browning and Wexler (1968) for determination of the kinematic properties of a linear wind field, combined with the recent treatment by Donaldson and Harris (1989) of non-linear wind fields in cyclonic flow. Potential-vortex fit is the ratio of calculated shearing deformation of the tangential wind component to twice its curvature estimated by distance from cyclone center. A value of this ratio near unity would be expected in an intense, mature hurricane. Values much less than unity would indicate a decaying circulation.

Potential-vortex fit was tested by Harris et al. (1989) in their simulated hurricane model. It was unity, as expected, because the model was designed to simulate an active and mature hurricane. The concept was also applied to observations of Hurricane Gloria acquired by the GL radar at Sudbury, Massachusetts, on September 27, 1985. The observational mode capable of generating the data needed for calculation of potential-vortex fit commenced at the time that the eye of Gloria was making landfall on the southern coast of Long Island, New York. Observations continued for more than three hours until the remains of Gloria's circulation center were in central Massachusetts and insufficient precipitation around the radar terminated the data acquisition. During the first half of the observations the values of potential-vortex fit averaged 0.32, with a peak of 0.44. This is

indicative of diminishing wind speed toward the circulation center. During the last half the values fell to an average of 0.17, strongly suggestive of a fatal breakdown in hurricane circulation, which was soon confirmed by direct Doppler velocity observations showing no rotation around the eye region. It is interesting to note that potential-vortex fit reached its peak value 40 minutes before the maximum tangential wind measured at the radar, suggesting its possible utility as a forecasting as well as diagnostic aid. It is well to remember, though, that one case study is only a bare beginning, however promising it may seem.

b. Mesoscale Wind Discontinuity

i. Overview

The purpose of this task was to develop a technique that would allow the automated detection of synoptic scale fronts. A technical report by Hamann(1990) contains detailed descriptions of this effort.

It is recognized that the only fronts that can be realistically addressed in this study are cold fronts, since they tend to have strong temperature gradients accompanied by sharp troughs and large velocity gradients. Doppler radar cannot measure the true wind field gradients across a front because it detects only one component of the air velocity, namely that along the radar beam. With the beam scanning in azimuth, this means that the gradients of radial velocity will vary as a function of aspect angle between the beam and the front. This dependability upon aspect angle plus the natural variability of the wind fields along a front makes the objective determination of the location of fronts a difficult task.

Real-time plan view displays of radar radial velocity data often reveal

readily observable structures interpretable as fronts. This structure usually consists of elongated regions of strong gradients with weak regions between over which the eye is able to interpolate to allow the identification of an extended front. In addition, these fronts can also be seen in the radar reflectivity displays in the form of distinct echo lines. Because both the velocity and reflectivity features are discernable by the eye, it followed naturally that this task might be viewed as an imaging problem. For this reason, the broader based area of image analysis has been examined for appropriate techniques that might be applied to this problem.

The adopted analysis technique involves the following procedures:

- \* Computation of gradients, either velocity or reflectivity
- \* Extraction of "edges" based on gradient magnitudes and orientations.
- \* Association of "edges" into streaks (fronts) based on continuity.

The details of these procedures are given in a separate technical report by Hamann (1990). In the following discussion, only an overview will be given of each of the procedures.

## ii. Gradient Computation

In both the reflectivity and velocity fields associated with fronts, one usually sees regions of sharp gradients. For this reason, emphasis was focussed on techniques that emphasized gradient detections. To simplify processing, the data are first converted from spherical to rectangular Carte-

sian coordinates. Data conditioning was then performed to reduce the impact of noise on the analysis. A technique was adopted where a series of templates were passed over a data array. Each of these templates assigned weights to various data points that fell within the template so as to detect the orientation and magnitude of the maximum gradient over the template domain. The results of the application of these templates are two arrays, one of gradient magnitudes and one of gradient orientations.

### iii. Edge Extraction

Edges are extracted from the gradient magnitude and orientation computations derived from the application of the templates described above. This involves the delineation of those regions with the largest gradients. Basically, thresholds are applied to the magnitudes and only those that pass this threshold test are considered to be "edges" on the first pass. Orientation constraints are also applied to reduce the effects of spurious data.

### iv. Streak Association

Results of the above edge analysis are a number of separate regions, of which many are along the line associated with the front. However, the ones along the front may not be connected. In addition, there are usually several spurious regions that have no relevance to the frontal interpretation. It is now necessary to eliminate these spurious regions and to extend and join the pertinent regions into streaks or fronts. This is accomplished by proceeding from the ends of each of the edges and examining the gradients and orientations to determine if the edges can be extended into regions that did not pass the original threshold test. In this way, each of the edges can be extended and combined into streaks that provide a more continuous representation of the front. In addition, area or length thresholds are applied

to the resultant streaks to eliminate any residual clutter and noise.

#### v. Results and Conclusions

Figs. 1 and 2 show the results of application of this technique. In the upper left of each figure is the original field; the lower left presents the gradient magnitudes; the lower right, the gradient orientations; and the upper right the resultant streaks. The case shown is for a particularly good cold front and the technique appears to work extremely well. Further examples are presented by Hamann (1990).

This technique shows a great deal of promise in the extraction of fronts for forecast purposes. It yields a line that is readily amenable to tracking and forecasting. In addition, it appears to have application to a number of related problems that involve the extraction of features from image data. In fact, this technique is being extended to be used as one of the procedures in the Cloud and Precipitation Forecast task to be described next. Further work is required to improve the association of edges into streaks, particularly, for less obvious fronts. Also, results of this type of analysis need to be utilized as input to techniques that track and forecast front locations.

#### c. Cloud and Precipitation Forecast

In the past Bohne et al (1988) and Bohne and Harris (1985) studied several techniques to describe satellite and radar data fields. From these studies and from the wind discontinuity study discussed above it has been determined that there are two techniques that appear to be quite effective in describing precipitation regions adequately for forecasting purposes: edge detection and contour extraction. The edge detection method is one devel-



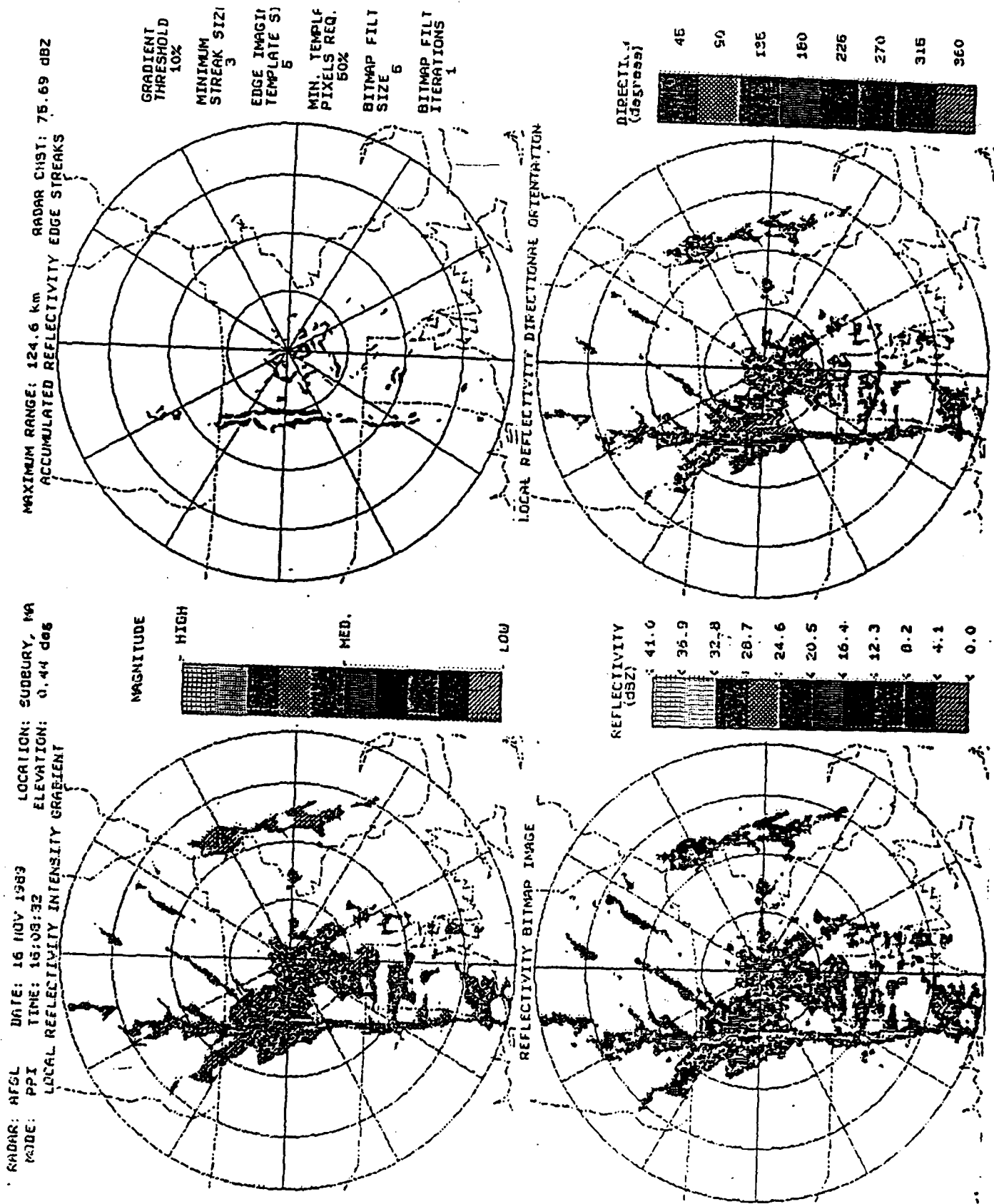
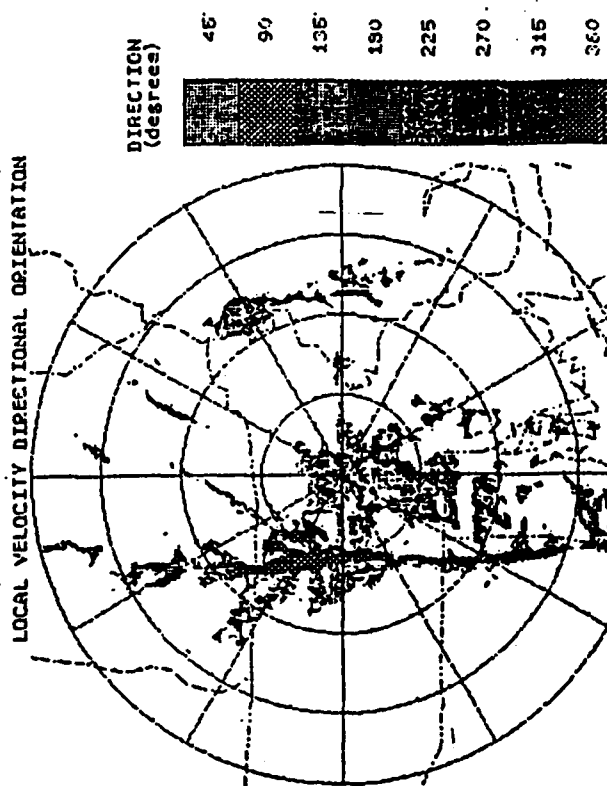
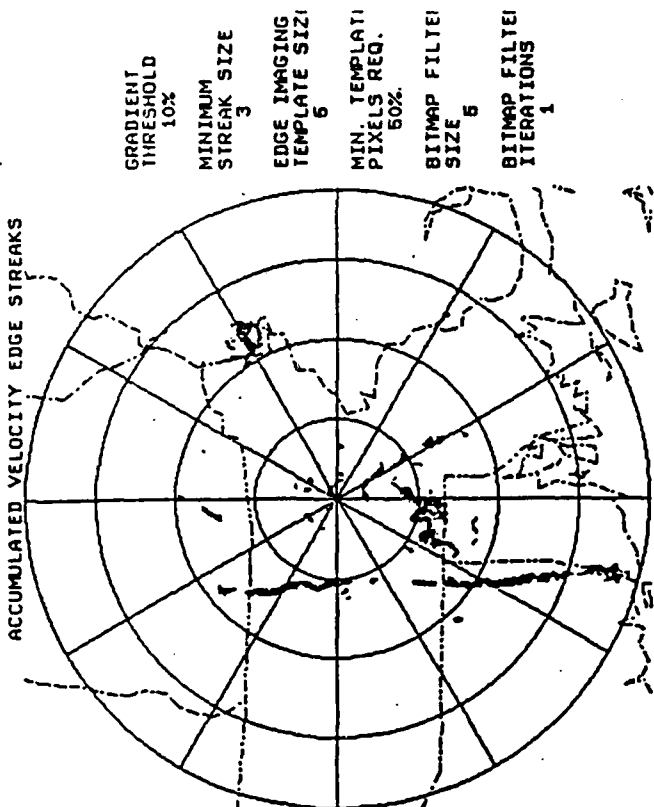


Fig. 1 Edge Detection Analysis for Reflectivity Data

RANGE RINGS: 32.0 km RESOLUTION: 387 X 387  
 MAXIMUM RANGE: 124.6 km NYQUIST: 33.21 m/s  
 ACCUMULATED VELOCITY EDGE STREAKS



**Fig. 2** Edge Detection Analysis for Velocity Data

oped for the detection of wind field discontinuities and is described briefly above and more extensively by Hamann (1990). It detects gradients of velocity and reflectivity and is very well suited to detect the more active portions of precipitation regions regardless of their reflectivity magnitudes. Contour extraction is better at outlining regions of known precipitation intensity, a characteristic to which forecasters can easily relate. Bohne et al (1988) and Bohne and Harris (1985) found that the Freeman chain code representation of contours is accurate, simple to implement, requires little computer storage, and is an ideal candidate for contour extraction and depiction. With these perspectives in mind, it was decided to implement and test these two candidates, individually and eventually, perhaps, combined in a comprehensive analysis package. More extensive discussion of these techniques and the results from this analysis are presented in a separate report by Bals and Hamann (1990).

#### i. Analysis Techniques

##### (1) Contour extraction

To extract contours there are three basic techniques that can be used. One is to precisely locate a contour through an interpolation process. This technique, while being quite accurate, is quite time-consuming and the resultant product, a series of coordinates, is not very amenable to tracking and forecasting. Another technique involves the determination of the best-fit geometric shape, such as an ellipse. This technique is not very precise although it does lend itself to tracking and forecasting. The third technique involves the extraction of a contour in the form of an initial Cartesian coordinate and a series of directional codes (commonly called the Freeman Chain code, FCC, after Freeman, 1961) that direct one around the perimeter of the data. This technique is only slightly less accurate than the interpolat-

ed contour method but is significantly more accurate than the geometric figure fitting routine. The FCC technique is simple to implement and is readily amenable to tracking and forecasting techniques. For this reason, the FCC technique has been chosen as a candidate for evaluation in the development of a tracking and forecasting method.

## (2) Edge Detection

Edge detection focusses attention upon enhanced gradient regions. From the meteorological standpoint this means that for the most part, attention is focussed upon the more active regions of a system, regardless of absolute values of the parameter being analyzed. The edge detection technique, developed by Hamann (1990) and outlined in the Mesoscale Discontinuity Detection analysis above, computes the magnitudes and orientations of the gradients and then extracts edges based on these determinations. This technique can be applied to extended regions as well as lines. A detailed discussion of edge detection appears in a report by Hamann (1990).

## (3) Feature Characterization

Once the contours or edges are extracted, descriptive parameters are needed to uniquely describe each region. From the Freeman chain code techniques can be derived to extract parameters such as area, perimeter, a center of mass, and the orientation of the major axis. The center of mass gives a unique origin for tracking, and ultimately forecasting, the movement of each region. Not only can the movement of the system be derived, but also the intensity of different regions within a system as it grows and decays. Similar parameters can be derived from the edge detection technique. This aspect of the analysis has not been treated in this task.

## ii. Analysis

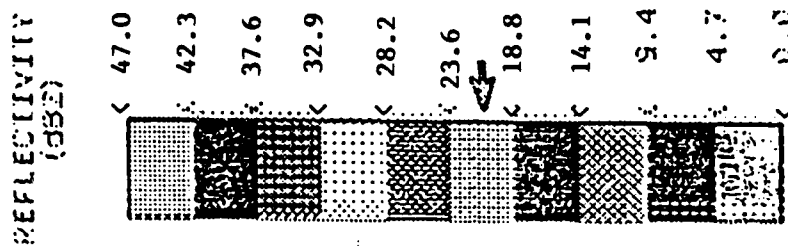
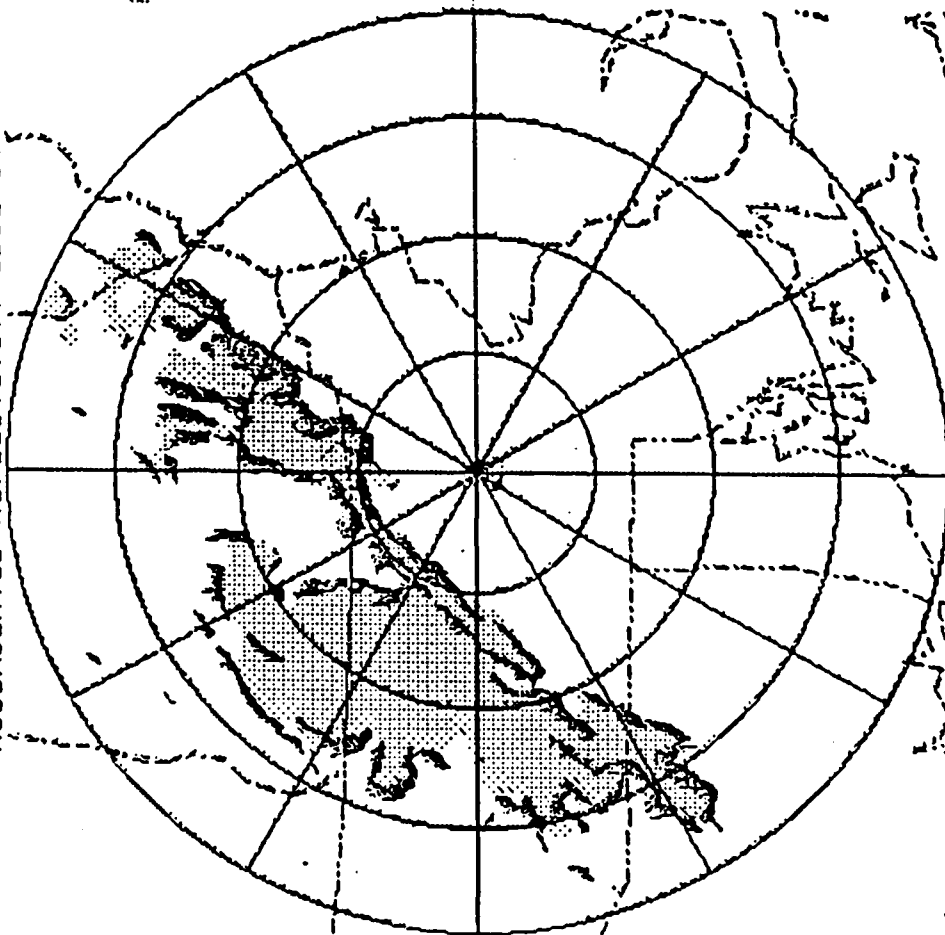
Figs. 3 depicts the precipitation region as detected by the GL Doppler radar at 1734 GMT 26 May 1984 as a cold front passed over New England. The precipitation region has been analyzed to extract the Freeman chain code and to detect significant reflectivity gradients (edges). The shaded region in Fig. 3 depicts shows the relectivity factor area enclosed by the contour for 18.8 dBZ as extracted with the Freeman chain code. Also in this figure are depicted the accumulated edge streaks for the reflectivity field. The edge streaks and the outer limits of the shaded areas define nearly the same areas, indicating that strong reflectivity gradients tend to be along the perimeter of precipitation regions. It should be noted, though, that this observation is highly dependent upon the type of precipitation. If the precipitation is more convective in nature, there will be significant gradients within the min reflectivity area associated with the region of greatest vertical motions. The situation depicted in Fig. 3 is more characteristic of a stratiform case than of an active thunderstorm.

The leading edge of precipitation, the most intense precipitation, and the area covered by the precipitation have all been defined by the edge detection and Freeman chain code techniques. A combination of this information along with products derived from the techniques, such as the center point, the movement of the gradients or the movement of the strongest reflectivities, will result in a forecast based not just on the translation of the center of a precipitation region, but also on the system characteristics as it grows and decays.

## iii. Summary

Two techniques were selected for evaluation as monitoring tools for

RANGE RINGS: 32.0 km      RESOLUTION: 387 X 387  
 MAXIMUM RANGE: 124.6 km    RADAR CNST: 75.69 dBZ  
 ACCUMULATED REFLECTIVITY EDGE STREAKS



GRADIENT  
THRESHOLD  
20%

MINIMUM  
STREAK SIZE  
5

EDGE IMAGING  
TEMPLATE SIZE  
7

MIN. TEMPLATE  
PIXELS REQ.  
50%

BITMAP FILTER  
SIZE 7

BITMAP FILTER  
ITERATIONS  
1

Fig. 3 Contour Analysis for Reflectivity Data

the location of cloud/precipitation. The edge detection technique highlights the significant features within a precipitation system. It detects significant gradients of reflectivity or wind velocity that are more than likely to be associated with significant weather. Contouring, especially with the Freeman chain code technique, successfully provides a compact and accurate method of identifying, extracting, and representing precipitation regions. Descriptive parameters of the regions are easily computed and can be used in tracking and predicting the movement of precipitation regions. Detection of the wind shift line along fronts or along gust fronts can lead to prediction of frontal movement or warn of the approach of severe weather within a region of precipitation. Prediction of not only the movement, but also the nature and evolution of the precipitation region is the objective of future work.

#### d. Tornado Probability

Research accomplished during the previous contract period by Donaldson and Desrochers (1985) and Desrochers et al. (1986) had suggested great promise for excess rotational kinetic energy (ERKE) as a predictor of tornadoes. ERKE is defined as the rotational kinetic energy of a mesocyclone core calculated with a diminished velocity, that is, maximum core velocity reduced by the product of core radius and a selected value of threshold shear.

Consequently, Donaldson and Desrochers (1990a) thoroughly analyzed a small sample of 17 mesocyclonic storms observed in Oklahoma. Eight of the 17 storms produced a total of 23 tornadoes, including 2 of violent (F4) intensity, 11 strong tornadoes (F2 and F3), and 10 weak tornadoes (F0 and F1). No tornadoes were reported with the other nine storms.

In addition to ERKE, calculations were also conducted for several other possible tornado predictors based on mesocyclone core characteristics. These included maximum core velocity, shear across the core, rotational kinetic energy, and several measures of energy multiplied by shear. Values of all candidate predictors were integrated from surface up to heights varying from 4 to 7 km, with and without a 10-minute persistent value, and, where appropriate, with threshold shear values ranging from 0.004 to 0.007  $\text{s}^{-1}$ . Two operational scenarios were envisioned: What is the best predictor of violent (F4) tornadoes, and what is best for identifying storms with non-violent (F0 to F3) tornado from those storms without tornadoes?

The results were evaluated by statistical analysis of the distribution of maximum predictor values, and by a performance analysis taking into account warning lead times for the earliest tornado in a storm as a function of a combined rate owing to false alarms and failures to detect. Candidate predictors were considered to fail if the statistical test indicated that crucial differences in maximum predictor values could have occurred by chance with a probability of more than 1%. Furthermore, predictors with excessive errors and negative lead times were eliminated. This left only ERKE as a suitable predictor of violent tornadoes, and ERKE followed closely by velocity as a predictor of the non-violent tornadoes.

Warning lead times with ERKE as a predictor were more than sufficient for the two violent (F4) tornadoes. The one with less warning provided a lead time of 28 minutes with no false alarms. For strong (F2 and F3) tornadoes, the median time to the first occurrence in a storm was 17 minutes with a false alarm rate of 6%. The warning parameters were not nearly as favorable for weak tornadoes of intensity F0 and F1, with a median lead time of 15 minutes but an unacceptable high false alarm rate of 35%. When the parameters are adjusted so that there is a zero false alarm



rate, the median lead time drops to 7 minutes and the detection failure rate became disappointingly high at 20%. For weak tornadoes, ERKE shows very little skill above the 40% false alarm rate suggested by Burgess and Lemon (1990) for tornado identification by the mere detection of mesocyclones, with no attempt to classify them quantitatively. Although the majority of tornadoes are in the weak category, the vast majority of deaths and serious injuries to humans are caused by strong and violent tornadoes. It is therefore fortunate that accurate warnings with adequate lead times can be achieved for the more intense tornadoes.

These encouraging results were obtained after careful visual inspection of the mesocyclones. However, a real-time automated technique is required for practical forecasting purposes. The improved mesocyclone detection algorithm developed by Desrochers (1990) made possible the testing of tornado prediction by real-time automated calculations of the required mesocyclone parameters. A small sample of 13 mesocyclonic storms in Oklahoma were found suitable for the test.

Results showed that the algorithmic tornado prediction process provided slightly greater median lead times than manual analysis, with ERKE as the best predictor, for strong and violent tornadoes. The ERKE warnings also suffered from fewer false alarms and negative lead times than warnings based on velocity, shear, or the product of rotational kinetic energy and shear. Although this is a minuscule sample, a statistical analysis revealed that the difference in means of ERKE measured in the tornadic versus the non-tornadic storms was significant at a level of confidence well above 99%. If this algorithm were incorporated by NEXRAD, it seems reasonable to expect good performance by NEXRAD radars in automated prediction of strong and violent tornadoes associated with mesocyclones.

The exact mechanism of tornado accompaniment to some of the more energetic mesocyclones, occurring tens of minutes after the mesocyclone is established, is not well understood. The success of ERKE for quantization of those mesocyclones likely to produce strong and violent tornadoes may provide a clue. It seems quite reasonable to expect that the establishment and maintenance of a mesocyclone in a viscous medium requires a minimum expenditure of energy. One manifestation of this energy, readily detectable by Doppler radar, is the rotational kinetic energy of the mesocyclone core. ERKE may be regarded as rotational energy derived from a rotational velocity excess to the requirement for maintenance of the mesocyclone circulation, and is consequently available as a source or a marker of an energy increment destined for tornado production.

In any event, ERKE has certain observational advantages over other candidate predictors. Unlike the thresholding required for mesocyclone identification, ERKE is a continuous, single-valued function. Another advantage of ERKE is its exclusion of very small values of core radius, which often represent artifacts in the Doppler velocity field with no meteorological significance. Still another advantage of ERKE over velocity and especially shear as predictors is the relative insensitivity of ERKE to the variability of antenna resolution errors with range. In a condition of poor resolution, the core radius is overestimated somewhat, while its peak velocity is underestimated. Since ERKE is formulated by the product of radius and velocity, its resolution errors are diminished.

e. Hail Size Estimation

In studies around the world, it has been shown that growth of large hail is related to the availability of liquid water, the magnitude of the vertical motion, and the duration of the hailstone within an active storm environ-

ment. Most diagnostic studies to date have focussed on the liquid water aspect basically because of the greater availability of more reliable estimates of liquid water. Single Doppler radar is not able to reliably estimate the three-dimensional flow within a storm, but it is able to provide velocity-based diagnostics as to the intensity of the updraft and the potential of recirculation of the hail particles in order to maximize their growth potential. Because of the success STX had achieved with the estimation of mesocyclone magnitude in the tornado probability task outlined above, it was decided to assess the value of mesocyclone characteristics in the forecast of hail size.

It is well-known that the more intense thunderstorms exhibit rotation and that the largest hail falls from these storms. Mesocyclones are readily detectable with Doppler radar and techniques have been developed to monitor their characteristics. These monitoring techniques are able to also provide indications of the relative importance of other aspects of the motion fields: upper-level divergence and vertical structure of divergence within the storm. The former of these gives an indication of the magnitude of the vertical velocity within the storm: the stronger the updraft, the greater will be the divergence. The latter indicates the potential for hail to remain within the storm or to be spewed out into the less active environment. In particular, if the divergence is confined to a relatively shallow layer in the upper portions of the storm, the hail is more likely to be dumped into the environment than if the divergence is spread over a deeper layer. Therefore, an ideal environment would be one where there is a strong updraft with a relatively low height for the maximum velocity. This structure would support large liquid water content and large hail, but would also allow the stones to remain within the storm environment for longer growth times.

## i. Analysis Techniques

### (1) Upper-Level Divergence

The mesocyclone algorithm measures, among other things, the maximum velocities towards and away from the radar ( $V_t$  and  $V_r$ , respectively) and the angle relative to the radar beam of a line joining the two maxima. These velocity extrema have contributions from both rotation and divergence and the angle  $\Theta$  between them is related to the relative magnitudes of the two types of motion fields. The divergence contribution to this velocity difference,  $\Delta V_r$ , is given by the following equation:

$$\Delta_r V = (V_t - V_r) \sin(\theta)$$

This expression was first derived by Witt and Nelson (1984) and showed some promise as a hail-size discriminator. In the analysis performed by STX, it was shown that in fact there is a correlation between  $\Delta V_r$  and hail size for hailers. The deviation within this group is quite large (about 32% of the total divergence). In addition, when non-hailers were included in the sample, the variation of  $\Delta V_r$  increases rather dramatically. The resultant False Alarm Ratio (FAR) was 0.58. Through averaging and imposing a persistence criterion the FAR was reduced by 50%. However, the utility of this parameter alone is not practical.

### (2) Rotational Kinetic Energy

Originally, a parameter, Rotational Kinetic Energy (RKE) was developed to categorize the energetics of the rotation in severe storms, given by:

$$RKE = \rho \pi \Delta h \frac{r^2 V^2}{4}$$

Later, Donaldson and Desrochers (1990) introduced the concept of Excess Rotational Kinetic Energy (ERKE) which is simply:

$$ERKE = RKE - RKE_T$$

where  $RKE_T$  is a threshold energy associated with the definition of a mesocyclone.

Evaluation of these two parameters (see Desrochers, 1990) revealed that ERKE showed virtually no skill in determining the hail production capability of any hailstorms. On the other hand, RKE had a stronger relationship (correlation coefficient of 0.98) between hail size and RKE value for hailers than was the case for  $\Delta V_r$ . Use of RKE yielded predictions of hail diameters of 4.5 cm and larger with an average lead time of 21 min. However, it also had a high FAR of 0.45, indicating this too is insufficient to serve as a reliable hailsize indicator.

### (3) Divergence Profile

A simple indicator of the relative importance of divergence and rotation within the storm is the orientation angle  $\Theta$  between the velocity maxima associated with the mesocyclone. When  $\Theta$  is  $45^\circ$  the two motion fields are of approximately equal importance, while if  $\Theta$  is  $0^\circ$  rotation dominates or  $90^\circ$  divergence dominates. The computation of the vertical gradient of  $\Theta$  ( $\Delta_A \theta$ ) therefore gives an indication of the variability of the vertical structure within the storms.  $\Delta_A \theta$  was correlated with hail-size and found to be linearly related as was the case for RKE and  $\Delta_r V$ . For the largest hail ( $> 5$  cm)  $\Delta_A \theta$  provided lead time forecasts of 13 min with a FAR of 0.01. With hail greater than 3.5 cm in diameter, the lead times were about 15 min but the FAR increased to 0.30 and for smaller hail the FAR increased even more,

as would be expected.

A detailed look at the vertical structure of divergence in the various storms revealed the following observations:

- \* The producers of large hail displayed a smooth transition from convergence in the low levels to divergence aloft while those that produced smaller hail displayed a more irregular transition.
- \* All hailers displayed some convergence at low levels (3 km).
- \* All hailers exhibited a significant component of divergence below 10 km height, a feature not seen in non-hailers.

## ii. Discussion

Three kinematic properties of storms were evaluated as discriminators of hailsize: divergence aloft, rotation, and divergence profiles. All three exhibited some degree of success. However, the divergence profile parameter  $\Delta_A\theta$  showed the greatest skill. In fact, it appears that the three-dimensional updraft structure is more important than the actual magnitudes of the updrafts. The vertical variations have more to do with the length of growth time that a hail stone experiences than the magnitude of the updraft. However, more effort needs to be directed towards this topic before a definitive solution is achieved.

## f. Velocity Dealiasing

A serious preprocessing problem for Doppler radar data is caused by

the inherent dynamic range of the velocity measurements. Pulsed Doppler radars are capable of detecting motions unambiguously only within a finite velocity range known as the Nyquist range. Typically for NEXRAD radars and similar 10 cm wavelength radars, this range is of the order of 30 m/s. Actual velocities outside of this range are detected as "folded" velocities, i.e. the real velocities are folded or aliased back into the Nyquist range according to the formula:

$$V_m = V_a - f V_n$$

$$\text{where } f = \text{int}\left(\frac{V_a}{2 V_n}\right)$$

This aliasing not only produces misrepresented velocities, but also results in artificially enhanced velocity gradients. This effect causes severe problems for any algorithm that relies on the accurate representation of the velocity magnitudes and/or gradients. This is a problem that does not appear to be adequately addressed in the NEXRAD system as currently configured. In order to test the algorithms being developed under this contract, STX found that it was necessary to develop a better automated dealiasing technique than was currently available. The result of this work has been an algorithm that has tremendous potential for inclusion as part of a more complete dealiasing algorithm within an operational radar system. This algorithm has been completely documented in a STX technical report "A Technique for Automated Velocity Dealiasing" by Desrochers, currently in press. The reader is referred to this report for a complete discussion since only an overview will be presented here.

#### i. The Dealiasing Technique

Usually, with 10 cm radar systems, the type of velocity aliasing most often encountered is a relatively localized phenomenon. When this occurs and the local shears are not intense, dealiasing can be performed quite easily

with a simple one or maybe a pseudo-two dimensional technique. However, in some of the more interesting storms, particularly those containing mesocyclones, these simple techniques fail, resulting in a breakdown of the automated algorithms such as the mesocyclone and tornado vortex signature (TVS) algorithms. STX has developed an efficient dealiasing technique that effectively deals with such situations. This technique involves the following steps:

- \* Test along each radar beam to determine if aliasing is present.
- \* If aliasing is present, apply a one dimensional (along the beam) dealiasing technique.
- \* Perform a two dimensional test to determine success of dealiasing.
- \* If dealiasing is determined unsuccessful, isolate the area where aliasing is still a problem.
- \* In the isolated area perform dealiasing by minimizing the two dimensional gradients.

This technique has the advantage of adapting its performance complexity as the situation warrants.

## ii. Results

Figure 4 contains an example of the type of region addressed by this technique. The technique was applied to approximately 5000 aliased regions from storms ranging from non-tornadic to violent tornadic. Of these



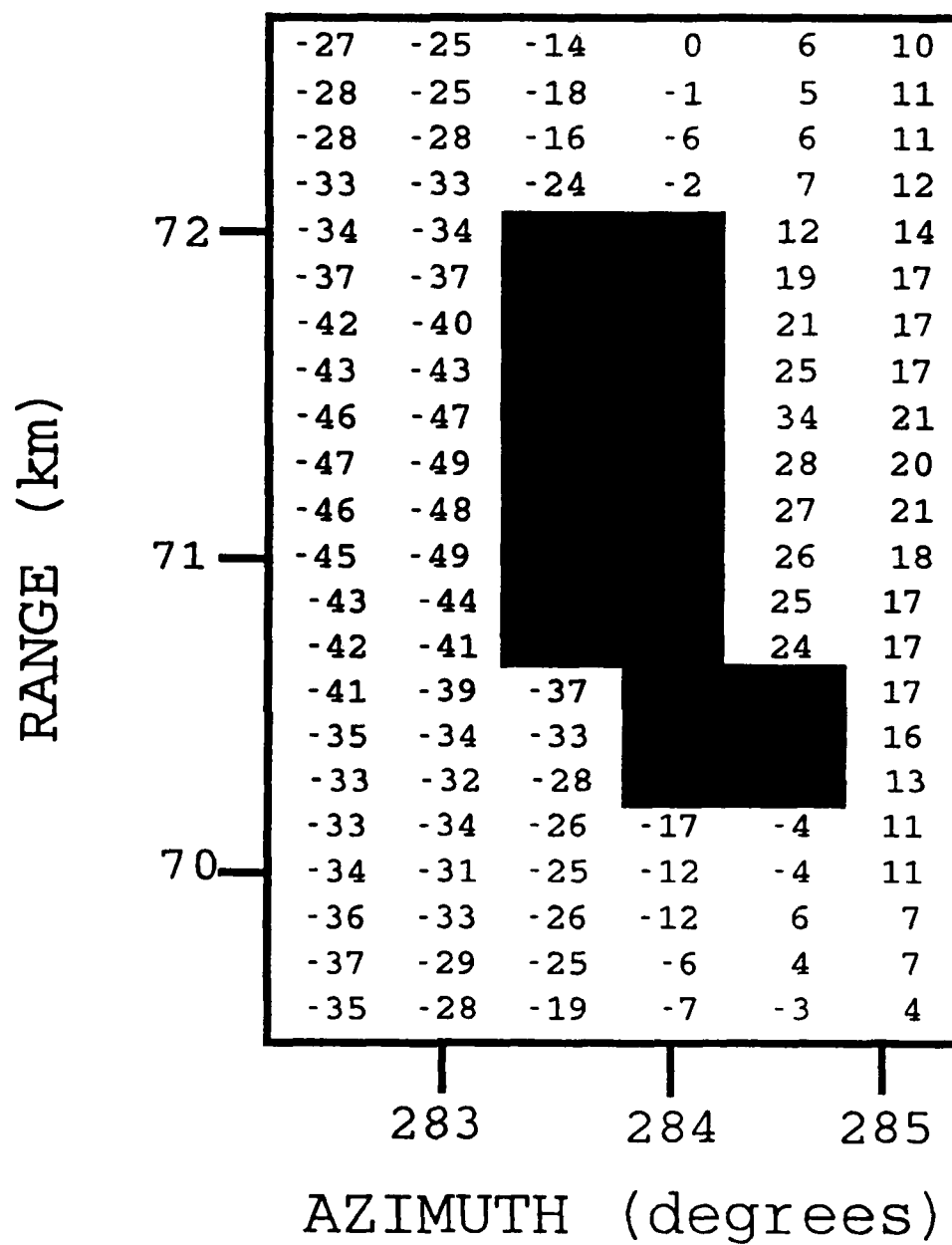


Fig. 4 Dealised velocity field with Nyquist of 34 m/s for original data.

aliased regions, 96% were processed correctly, resulting in 99.96% of all data being processed correctly. Performance was analyzed as functions of velocity Nyquist ranges and the types of phenomena causing the aliasing. It was found that performance was not strongly affected by the Nyquist velocity range, at least over the ranges examined, namely 24 to 34 m/s. It was also found that the algorithm showed little preference for problems due to natural sources over those induced artificially.

Because this algorithm relies upon isolation of problem areas it requires more data to be stored than for simpler one-dimensional techniques. The amount of data required to be retained is adjusted according to the size of the problem area. However, the larger the area the greater the storage requirements and the greater the processing time. To assess the impact of problem area size upon the performance of this algorithm, an analysis of the azimuthal and radial extent of problem areas was performed. In general it was found that the algorithm requires at least 6 radials of data to be 90% effective, with effectiveness increasing to 99% with 10 radials. The other observation from this study is that the problem is primarily a low level phenomenon. 48% of the problems occur below 2 km height and 77% occur below 5 km. Actually, there are two preferred height regions for problem areas: near the ground and near the top of the storm due to the outflow.

### iii. Summary and Recommendations

A very successful and efficient tool has been designed for the automated dealiasing of Doppler radar velocities. This technique should not be considered to be all encompassing since it does not handle large area aliasing problems. Techniques developed elsewhere, such as at the National Severe Storms Laboratory (NSSL), treat the large area problem better. It is

necessary for GL and NSSL personnel to get together in an effort to design an integrated dealiasing package that will work effectively and efficiently on a wide variety of problems.

### **3. OTHER ACTIVITIES**

During the course of this contract STX has played an active role in various activities within the radar meteorology community. Desrochers and Donaldson made substantial contributions to the landmark book **Radar in Meteorology**, the result of the 40th Anniversary and Battan Memorial Conference on Radar Meteorology. In addition, Donaldson, Desrochers, and Harris made presentations at the NEXRAD meeting on algorithms held at the GL Weather Radar Facility. Desrochers was involved in a special meeting called by the NEXRAD/JSPO on velocity dealiasing for NEXRAD. Other meetings with STX involvement include:

- \* 14th Conference on Severe Local Storms
- \* 15th Conference on Severe Local Storms
- \* 16th Conference on Severe Local Storms
- \* 23rd Conference on Radar Meteorology
- \* 24th Conference on Radar Meteorology

At each of these conferences STX personnel made either oral or poster presentations that were all well received.

### **4. SUMMARY**

This report concludes all activity associated with this contract. Several of the activities have shown significant promise and follow on work has been initiated under a new contract. Tremendous success was achieved in the realms of Tornado Probability, Velocity Dealiasing, and Hurricane Intensity. All of these efforts have resulted in algorithms that should be considered for incorporation in the NEXRAD program. Excellent

advances were made in the other three efforts, Hail Size Estimation, Mesoscale Wind Discontinuity detection, and Cloud/Precipitation Forecast. However, more work is necessary before reliable algorithms will be ready for implementation.

## 5. REFERENCES

Bals, T.M., 1990: Techniques to Delineate Precipitation Regions. STX Scientific Report #3. (In Preparation).

Bohne, A.R., F.I. Harris, P.A. Sadoski, D. Egerton, 1988: Short Term Forecasting of Cloud and Precipitation. AFGL-TR-88-0032, 94pp. ADA212619.

Bohne, A.R. and F.I. Harris, 1985: Short Term Forecasting of Cloud and Precipitation. AFGL-TR-85-0343. ADA169744.

Browning, K. A., and R. Wexler, 1968: The determination of kinematic properties of a wind field using Doppler radar. J. Appl. Meteor., 7, 107-113.

Burgess, D. W. and J. R. Lemon, 1990: Severe thunderstorm detection by radar. Chapter 30a, Radar in Meteorology, D. Atlas, ed., American Meteorological Society, Boston, 619-647.

Desrochers, P.R., 1989: A reliable method for real-time velocity unfolding. PrePrints, 24th Conf. on Radar Meteor., Amer. Meteor. Soc., 415-418.

Desrochers, P.R., 1990: Technique for Automated Velocity Dealiasing.

**STX Scientific Technical Report #1, GL-TR-90-0079, 109pp.**

**Desrochers, P.R. and D.E. Forsyth, 1988: "Performance comparison of an improved mesocyclone detection algorithm with the NEXRAD mesocyclone algorithm." 15th Conf. on Severe Local Storms, 201-204**

**Desrochers, P.R., 1990: Automatic Mesocyclone Detection for Tornado Forecasting. STX Scientific Report. (In Preparation).**

**Desrochers, P.R., 1990: Some aspects of the mesocyclone related to hail formation. Preprints, 16th Conf. on Severe Local Storms. (In Press).**

**Desrochers, P. R., R. J. Donaldson, Jr., and D. W. Burgess, 1986: Mesocyclone rotational kinetic energy as a discriminator for tornadic and non-tornadic types. Preprints, 23rd Conf. on Radar Meteorology (Snowmass), 1-4).**

**Donaldson, R. J., Jr., and P. R. Desrochers, 1985: Doppler radar estimates of the rotational kinetic energy of mesocyclones. Preprints, 14th Conf. on Severe Local Storms (Indianapolis), 52-55.**

**Donaldson Jr, R.J. and P.R. Desrochers, 1990: Improvement of tornado warnings by Doppler radar measurement of mesocyclone rotational kinetic energy. Weather and Forecasting, 5, 247-258.**

**Donaldson Jr., R.J. and P.R. Desrochers, 1990: Comparison of algo-**

rithmic and manual performance of tornado predictors derived from Doppler data. Preprints, 16th Conf. on Severe Local Storms. In Press.

Donaldson Jr., R.J. and F.I. Harris, 1989: "Estimation by Doppler radar of curvature, diffluence and shear in cyclonic flow. Jour. of Atmos. and Oceanic Tech., 6, 26-35.

Donaldson Jr., R.J., 1989: Potential - Vortex Fit. Preprints, 24th Conf. on Radar Meteor. pp 186-189.

Freeman, H., 1961: On the encoding of arbitrary geometric configurations. IRE Trns. Electron. Comput., EC-10: 260-269.

Hamann, D.J., 1990: Wind Field Discontinuity Detection with Doppler Radar. STX Scientific Report #2. (In Preparation).

Harris, F.I., D.J. Hamann, and R.J. Donaldson Jr., 1989: Hurricane monitoring with Doppler radar: A simulation. Preprints, 24th Conf. on Radar Meteor., 203-206.

Ruggiero, F.H., and R.J. Donaldson Jr., 1989: Features resembling single Doppler vortex signatures observed in an extratropical cyclone. Preprints, 24th Conf. on Radar Meteor., 240-243.

Witt and Nelson, 1984: The relationship between upper-level divergent outflow magnitude as measured by Doppler radar and hailstorm intensity. Preprints, 22nd Conf. on Radar Meteor., AMS, Boston, MA, 108-111.

**Wood, B. T. and R. A. Brown, 1987: Simulated land-based NEXRAD  
Doppler measurements within hurricanes. Preprints, 17th Conf.  
on Hurricanes and Tropical Meteorology (Miami), 174-177.**

## APPENDIX A. - List of Reports/Publications Produced under Contract

### VELOCITY DEALIASING

Desrochers, P.R., 1989: A reliable method for real-time velocity unfolding. PrePrints, 24th Conf. on Radar Meteor., Amer. Meteor. Soc., 415-418.

Desrochers, P.R., 1990: Technique for Automated Velocity Dealiasing. STX Scientific Technical Report #1, GL-TR\_90-0079, 109pp.

### TORNADO PROBABILITY

Desrochers, P.R. and D.E. Forsyth, 1988: "Performance comparison of an improved mesocyclone detection algorithm with the NEXRAD mesocyclone algorithm." 15th Conf. on Severe Local Storms, 201-204

Desrochers, P.R., 1990: Automatic Mesocyclone Detection for Tornado Forecasting. STX Scientific Report. (In Preparation).

Donaldson Jr., R.J. and P.R. Desrochers, 1990: Improvement of tornado warnings by Doppler radar measurement of mesocyclone rotational kinetic energy. Weather and Forecasting, 5, 247-258.

Donaldson Jr., R.J. and P.R. Desrochers, 1990: Comparison of algorithmic and manual performance of tornado predictors derived from Doppler data. Preprints, 16th Conf. on Severe Local



Storms. In Press.

#### HAIL SIZE ESTIMATION

Desrochers, P.R., 1990: Some aspects of the mesocyclone related to hail formation. Preprints, 16th Conf. on Severe Local Storms. (In Press).

#### HURRICANE SEVERITY

Donaldson Jr., R.J. and F.I. Harris, 1989: "Estimation by Doppler radar of curvature, diffluence and shear in cyclonic flow. Jour. of Atmos. and Oceanic Tech., 6, 26-35.

Donaldson Jr., R.J., 1989: Potential - Vortex Fit. Preprints, 24th Conf. on Radar Meteor.

Harris, F.I., D.J. Hamann, and R.J. Donaldson Jr., 1989: Hurricane monitoring with Doppler radar: A simulation. Preprints, 24th Conf. on Radar Meteor., 203-206.

Ruggiero, F.H., and R.J. Donaldson Jr., 1989: Features resembling single Doppler vortex signatures observed in an extratropical cyclone. Preprints, 24th Conf. on Radar Meteor., 240-243.

#### MESOSCALE WIND DISCONTINUITIES

Hamann, D.J. 1990: Wind Field Discontinuity Detection with Doppler Radar. STX Scientific Report #2. (In Preparation).

## CLOUD AND PRECIPITATION FORECASTING

Bals, T.M. 1990: Techniques to Delineate Precipitation Regions. STX Scientific Report #3. (In Preparation).

## MISCELLANEOUS

Donaldson Jr, R.J., 1987: "Significance of the 40th Anniversary Conference." Address at the Battan Memorial and 40th Anniversary Conference on Radar Meteorology, (AMS), Boston, MA.

Golden, J.H. and panel members (including P.R. Desrochers), 1990: "Severe storm detection: Panel report." Chapter 30b, Radar in Meteorology. D. Atlas, ed., AMS, Boston, MA, 648-656.

Donaldson Jr., R.J., 1989: "Foundations of severe storm detection by radar." Chapter 15, Radar in Meteorology. D. Atlas, Ed., AMS, Boston, MA 115-121.

**APPENDIX B: Conference Papers and Journal Articles Published During  
Contract.**

**B-1: Paper on Velocity Dealiasing**

**Desrochers, P.R., 1989: A reliable method for real-time velocity unfolding. PrePrints, 24th Conf. on Radar Meteor., Amer. Meteor. Soc., 415-418.**

The U.S. Government is authorized to reproduce and sell this report. Permission for further reproduction by others must be obtained from the copyright owner.

# A RELIABLE METHOD FOR REAL-TIME VELOCITY UNFOLDING

Paul R. Desrochers\*  
ST Systems Corporation (STX)  
109 Massachusetts Avenue  
Lexington, MA 02173

## 1.0 INTRODUCTION

There is a basic need for real-time radar data processing systems such as NEXRAD to have a reliable technique for removing ambiguities due to velocity aliasing. Performance of many NEXRAD analysis algorithms is adversely affected when these ambiguities are not resolved. This paper presents a new dealiasing technique that offers both exceptional reliability and real-time operating capability.

## 2.0 THE DEALIASING PROBLEM

Velocity detected by pulsed Doppler radar is constrained to a finite dynamic range. The velocity equal to one-half this dynamic range is commonly referred to as the Nyquist velocity ( $V_n$ ). It is related to the wavelength of the radar  $\lambda$  and the pulse repetition frequency PRF by:

$$V_n = (\lambda * PRF) / 4 \quad (1)$$

Doppler radars can therefore measure velocities unambiguously in the range of  $\pm V_n$ . Any velocities outside of this range are aliased into it according to:

$$V_m = V_t - f * 2V_n \quad (2)$$

where  $V_m$  and  $V_t$  are the measured and true velocity, respectively. The truncated integral Nyquist range is given by:

$$f = \text{int} (V_t / 2V_n) \quad (3)$$

True velocities  $V_t$  of 55 m/s, 5 m/s, and -45 m/s have corresponding  $f$  values of 1, 0, and -1 for a Nyquist velocity of 25 m/s. These velocities are all measured as 5 m/s.

Velocity dealiasing or unfolding is the process of placing measured velocities into the proper Nyquist range. In general, dealiasing involves the selection of  $f$  such that local point-to-point velocity differences ( $\Delta V$ ) are minimized. The simplest approach is to compare  $\Delta V$  in one direction, between only two points. This is done in the most common dealiasing technique, the traditional one-dimensional (1-D) technique, where processing occurs in the radial direction.

\*This work was performed under AFGL contract F19628-87-C-0124.

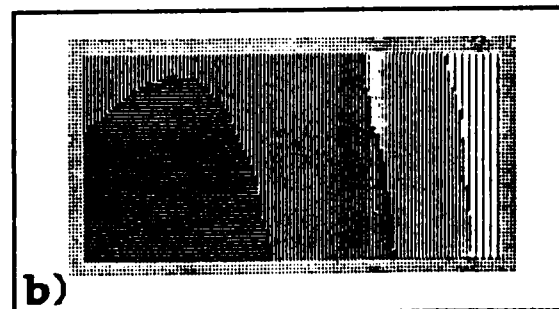
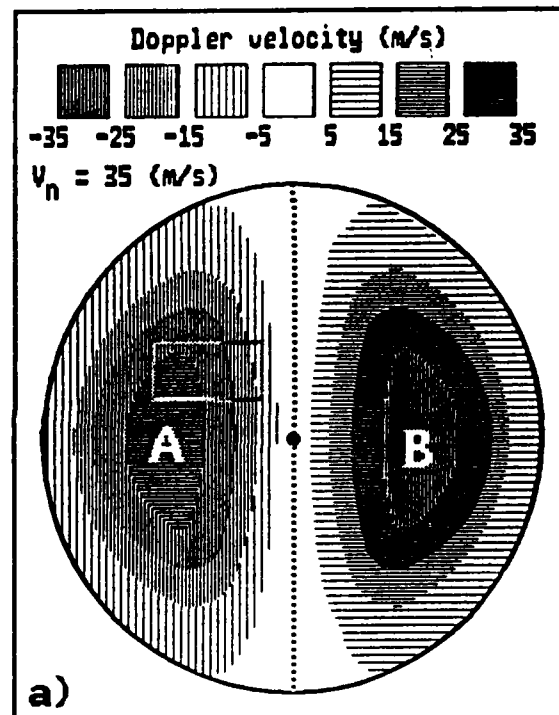


Fig. 1) Idealized windfield of westerly flow. Aliased velocities are implied in areas A and B shown in a). Outlined area in a) corresponds to b). General ambiguity exists in b) because no reference for dealiasing exists.

### 3.0 REGIONS OF AMBIGUITY

The 1-D technique is not always reliable. Firstly, problems are encountered in the initialization process. As noted above, a value is dealiased through comparison with a previous value. However, the first value encountered has no such reference and can therefore be considered ambiguous. If unresolved, this ambiguity will propagate throughout an entire region or data set and it can be considered general in nature. A second problem arises due to the presence of large natural gradients (LNGs), where  $\Delta V$  exceeds  $V_n$ . These real gradients are usually of limited extent and often make it impossible for the 1-D techniques to correctly dealias measured velocities.

#### 3.1 General ambiguity

When the velocity field is well sampled such that one can invoke continuity across the entire field, dealiasing is rarely a problem. For example, in Fig. 1a there is a velocity field obtained from a relatively uniform west to east flow field. From the zero line oriented north-south through the radar one can progress outwards and assess the aliased or dealiased state of each data point. In this case it is quite apparent that the sharp  $\Delta V$ s around the regions denoted by A and B are due to aliasing and can consequently be correctly dealiased. All ambiguities can be assessed.

On the other hand, when only a fraction of the field is observed (e.g. Fig. 1b), there is often no true reference point or line like the zero line in Fig. 1a. In Fig. 1b from the  $\Delta V$ s it is obvious that there are aliased velocities. However, because of the lack of a good reference velocity, one can only dealias the velocities in relation to one another, leaving an overall ambiguity to the absolute velocities of the entire field. This leaves an overall general ambiguity.

Methods exist to reduce general ambiguity. Most common of these is a Velocity Azimuth Display (VAD) approach where wind field characteristics obtained from current or previous scans are used as a reference. The VAD approach is useful for initialization purposes only when steady state conditions exist, the wind fields are free of perturbations, and precipitation is widespread.

Merritt (1984) developed a technique that overcomes VAD constraints. The uncorrected velocity field is divided into regions of like sign to differentiate aliased and non-aliased quantities. A reference for dealiasing is attained by assuming the largest area of like sign is not aliased. Dealiasing can then proceed from this area. Since sign changes across the zero line wind field orientation can be obtained. This can further aid in the dealiasing process. Additional work on this technique was done by Bergen and Albers (1987). They have achieved magnificent results for reducing general ambiguity.

#### 3.2 Relational ambiguity

In situations where  $\Delta V$  is small, no larger than  $V_n$ , it is always clear how neighboring velocity values relate to one another even when there is general ambiguity. In these cases  $\Delta V$  is a known quantity. However, where LNGs exist the interrelationship between points is not clear and

$\Delta V$  is ambiguous. Ambiguity about point-to-point velocity differences will therefore be referred to as relational ambiguity. An example of this is seen in the Binger, OK mesocyclone shown in Fig. 2. The shaded region delineates the field of relational ambiguity within the overall field of general ambiguity.

Identification of relational ambiguities requires perusal in at least two-dimensions. The simplest approach is to use two radials such that a "corrected" radial guides the dealiasing of the adjacent "subject" radial. Relational ambiguities are identified by thresholds that operate on point-to-point velocity differences. Such a technique was developed by Eilts and Smith (1988). It operates by minimizing radial velocity differences over subtended segments in the corrected and subject radials. Success is achieved when thresholds limiting  $\Delta V$  are correctly matched with the phenomena being dealiased.

Two-radial techniques are not always reliable. This is because their analysis is biased by the direction from which dealiasing proceeds. These techniques work well for flagging relational ambiguity but are unable to precisely locate LNGs. Therefore, they are prone to localized failure, and this is often compounded by error propagation in range and azimuth.

Directional bias must be eliminated if relational ambiguities are to be reliably dealiased. Therefore, data values on all four sides of a relational ambiguity must equally control dealiasing. It is necessary then that the surrounding values be first corrected in relation to one another. Since  $\Delta V$  is no larger than  $V_n$  dealiasing can be accomplished reliably with the 1-D technique. Also, since dealiasing is a localized process only perimeter values surrounding a relational ambiguity need to be

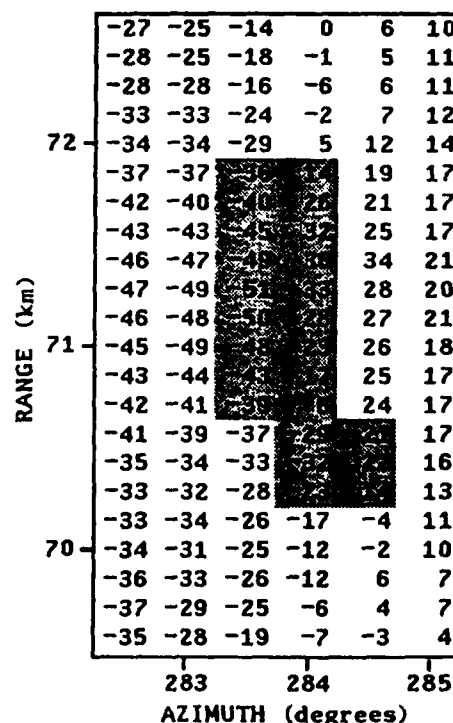


Fig. 2) An example of relational ambiguity. Doppler data from the Binger, OK mesocyclone (22 May 1981) at 1910 CST and 4 km height. The Nyquist velocity is 34 (m/s). Zero Doppler velocity is indicated by the dashed line.

correct in order to establish a reference for dealiasing. This is the basis for a new dealiasing technique where relative ambiguities are isolated and then corrected using adjacent members as references.

#### 4.0 THE ALGORITHM

The technique is designed for real-time operation. This is accomplished by two complementing analysis techniques, one to process general ambiguities and the other for relational ambiguities. A simple and fast routine called SEARCH corrects data for general ambiguity and monitors for relational ambiguities. Two routines are then used to process a relational ambiguity. Relational ambiguities are isolated in DEMARCATION and then dealiasing in CORRECTION. These routines are computationally intensive but are extremely reliable. Additional routines exist for housekeeping and data continuity.

**SEARCH:** In this routine radial data are processed in a sequential manner, gate-by-gate, away from the radar. Dealiasing is accomplished with the 1-D technique. This is sufficient to handle most data but requires monitoring since failure is possible in LNG situations.

Detection of LNGs oriented radially or azimuthally, or both, is possible by monitoring azimuthal  $\Delta V$ . LNGs oriented radially cause the 1-D technique to fail since velocity values beyond a LNG become incorrectly unfolded by one Nyquist interval. This artifact is detected as an artificially large azimuthal  $\Delta V$ .

Large azimuthal  $\Delta V$ s are correctly unfolded by the 1-D technique. However, with the simple technique used to detect LNGs orientation can not be distinguished. Therefore, both radially and azimuthally oriented LNGs are flagged for further scrutiny by DEMARCATION and CORRECTION.

**DEMARCATION:** All relational ambiguities flagged by SEARCH are isolated within DEMARCATION. Isolation is accomplished through identification of the periphery of small natural  $\Delta V$  that exists around the zone of relational ambiguity. Such a periphery is seen just outside the shaded area in Fig. 2. Since the natural  $\Delta V$ s around the periphery are less than  $V_n$ , they can be unfolded reliably using the simple 1-D technique.

Only three radials are required to isolate a relational ambiguity confined to one radial. More radials are required if a LNG extends over multiple radials. The radial length of a relational ambiguity is also determined in the isolation process and typically varies from about 10 to 100 gates.

**CORRECTION:** The small  $\Delta V$  periphery identified in DEMARCATION provides the perspective necessary for a reliable, objective analysis of a relational ambiguity. Unfolding is accomplished by an iterative, consensus approach that is controlled by previously unfolded peripheral values. Six steps comprise this process.

A) Dealiasing begins in one of the four corners of the demarcated area. The corner value is dealiasing with neighboring, peripheral values. The data field is then processed in a stepwise manner until the opposite corner of the analysis area is encountered. Dealiasing is accomplished by a two-dimensional (2-D) technique where  $\Delta V$  is minimized spatially. Dealiasing of each

subsequent value is biased not only by the corrected peripheral values but also by adjacent, newly-dealiasing values. The correctness of values within the analysis array is therefore considered tenuous in this stage.

B) Step A is repeated but with the start location in the opposite corner of the field.

C) The two arrays of tenuous data from steps A and B are compared. Where there is agreement the data value is assumed to be correctly dealiasing and is flagged as such. Otherwise, the data value is left open for further assessment.

D) With the output of step C as the starting field, steps A through C are repeated until no more agreements are obtained.

E) If uncorrected values remain in the analysis array, steps A through D are repeated but with the two remaining corners of the analysis array being used to initialize the process.

F) If any uncorrected values remain after E is completed they are unfolded such that the azimuthal  $\Delta V$  is minimized.

Although the correction process may appear intensely iterative, this is not the case. Most situations can be corrected with between 2 and 6 iterations of steps A through D. Step E is generally not necessary.

#### 5.0 IMPLEMENTATION CONSIDERATIONS

##### 5.1 Filtering

For any dealiasing technique to be effective, it is necessary that spurious data first be eliminated because they put large demands on processing. Three filtering techniques were designed to accomplish this.

The first filter eliminates data based upon signal strength. Data are accepted for further processing if their signal return is above some arbitrary threshold above noise. Exceptions to the acceptance criteria are made for data below threshold that are relatively free of noise. This condition is inferred when  $\Delta V$  is no greater than  $V_n/4$  within a test segment length of eight gates. These thresholds are arbitrary but work well.

The second technique is a size filter. Small features, less than eight contiguous gates in length are eliminated. These features are of little meteorological importance and their elimination improves the performance of the technique used to initialize isolated features (section 5.3).

The final preprocessing step eliminates point-spikes. This is accomplished by computing the radial velocity differences on either side of each data point. When both differences exceed the arbitrary threshold of  $V_n/2$  a point spike is declared and the value is flagged.

##### 5.2 Algorithm Initialization

Since the SEARCH routine uses a corrected reference radial to control unfolding in the adjacent subject radial, a method is needed to initialize the first radial of the program. A simple procedure works well as long as a few precautions are taken.

No reference is available to help unfold the first radial. It is therefore necessary that

steps are taken to minimize failure. Two potential problems exist. An aliased velocity might be used to initialize the radial and/or a LAG may exist along the radial. Neither of these problems can be detected with the 1-D technique used to unfold the radial.

The first problem can usually be avoided by initialization at low elevations. Any radial, regardless of elevation angle, can be used if initialization is done near the radar but away from data contaminated by ground clutter. The second problem is more difficult to avoid. LAGs, however, can be inferred by the magnitude of the gate-to-gate  $\Delta V$  revealed during unfolding. Note that this velocity difference is not necessarily real but may be induced by the 1-D technique. Radials with gate-to-gate  $\Delta V$  in excess of the arbitrary threshold  $V_n/2$  are assumed to contain LAGs and are not used to initialize the algorithm. This technique was found to be not particularly sensitive to the threshold selected.

### 5.3 Isolated Features

The problem of initializing isolated features is addressed by techniques that correct general ambiguity. This algorithm addresses only relational ambiguity. It is not the intent or purpose of this work to present a new solution to resolving general ambiguity. The problem has been addressed here, however, because of difficulties produced in the unfolding process; an unresolvable conflict occurs when correctly and incorrectly initialized radials meet. A simple technique was designed where isolated features are initialized with nearby, corrected features. The purpose is not so much to assure correct initialization, but to maintain continuity.

An isolated feature can be initialized by features along the subject radial or in the adjacent, corrected radial located either ahead or behind the isolated feature. A feature is a candidate to initialize another only if the two features are within a propagation distance (D) defined as:

$$D = V_n \cdot \lambda / |V_b - V_e|$$

where  $V_b$  and  $V_e$  are the begin and end velocities of the feature,  $\lambda$  is the length of the feature, and  $V_n$  is the Nyquist velocity. If more than one feature is a candidate the nearest is selected. If no values satisfy the condition, the isolated feature is assumed to be correct as is.

### 6.0 CASE STUDIES AND RESULTS

Some of the most difficult unfolding situations are those associated with severe thunderstorms. Data from four days of thunderstorm activity were selected for the study. These storms cover the gamut of thunderstorm intensity from non-tornadic to severe tornadic (F4) (Table 1). Also represented in the sample are the typical Nyquist ranges used when sampling these storms by S-band radar: 24, 28, and 34 m/s. All the storms were observed by the National Severe Storms Laboratory S-band radar in Norman, Oklahoma. For three cases the data were processed with the AFGL pulse-pair processor used during the Joint Doppler Operational Program (JDOP). For the fourth, the NSSL processor was used.

A total of over 5000 cases of relational ambiguity were identified by the algorithm. These cases are roughly separated among natural and spurious data. Only about 1 percent of the

Table 1. Case studies.

Storm	Date	tornadoes produced			analysis times (CST)
		W	S	V	
Ada	5/23/78	0	0	0	1740 - 2015
Binger	5/22/81	3	1	1	1515 - 2010
Del City	5/20/77	0	2	0	1610 - 1930
Piedmont	4/30/78	1	3	1	1545 - 1920

W = weak tornadoes (F0 - F1)

S = strong tornadoes (F2 - F3)

V = violent tornadoes (F4 - F5)

data contain relational ambiguities, but these data contain extremely important meteorological information. The algorithm correctly processed these 96 percent of the time. This corresponds to 95 percent accuracy for spurious data and 97 percent accuracy for natural data.

Failures of the algorithm in natural data occurred, for the most part, at the edge of a boundary where the signal strength fell below threshold. In these cases the perimeter surrounding a relational ambiguity is incompletely defined and directional bias is a problem. To counteract this problem, the data were threshold at low signal levels. As a result, mesocyclones, which often are near echo boundaries, appear to have been treated correctly in nearly all cases.

Additional failures in natural data are associated with the inability to isolate a relational ambiguity. This can occur at either the beginning or end of a radial where the data are truncated. This is a design limitation of the algorithm.

Failures in spurious data resulted primarily when implementation thresholds in DEMARCATION were exceeded. Nominal thresholds of 120 contiguous gates in range and ten azimuths define the maximum operating resolution of DEMARCATION. The range threshold can be exceeded by jamming signals, as from military aircraft. Conversely, the azimuthal threshold can be exceeded by interference bands.

### 7.0 CONCLUSIONS

A new two-dimensional velocity dealiasing technique is presented. This was tested on severe thunderstorms and was found to correctly process 96 percent of those problem areas remaining after the application of a 1-D technique. This degree of reliability can have a tremendous impact on phenomena detection algorithms, such as those in NEXRAD, that depend heavily on data integrity. The algorithm operates in real-time on a 1 MIP processor and appears to represent a suitable approach for NEXRAD operations since computational demands are optimized without compromising reliability.

### 8.0 REFERENCES

- Bergen, W.R. and S.C Albers, 1988: Two- and three-dimensional de-aliasing of Doppler radar velocities. J. Atmos. Oceanic Technol. Vol. 5, p. 305-319.
- Eilts, M.D and S.D Smith, 1988: Efficient de-aliasing of Doppler velocities. Submitted for publication.
- Merritt, M.W., 1984: Automatic velocity de-aliasing for real-time application. Preprints, 22nd Conf. on Radar Meteor., AMS, Boston, MA, 528-533.



**B-2: Papers on Tornado Probability**

**Desrochers, P.R. and D.E. Forsyth, 1988: "Performance comparison of an improved mesocyclone detection algorithm with the NEXRAD mesocyclone algorithm." 15th Conf. on Severe Local Storms, 201-204**

**Donaldson Jr., R.J. and P.R. Desrochers, 1990: Improvement of tornado warnings by Doppler radar measurement of mesocyclone rotational kinetic energy. Weather and Forecasting, 5, 247-258.**

**Donaldson Jr., R.J. and P.R. Desrochers, 1990: Comparison of algorithmic and manual performance of tornado predictors derived from Doppler data. Preprints, 16th Conf. on Severe Local Storms. In Press.**

S3.3

## PERFORMANCE COMPARISON OF AN IMPROVED MESOCYCLONE DETECTION ALGORITHM WITH THE NEXRAD MESOCYCLONE ALGORITHM

Paul R. Desrochers\*

ST Systems Corporation (STX)  
109 Massachusetts Avenue  
Lexington, MA 02173

Doug E. Forsyth

National Severe Storms Laboratory  
1313 Halley Circle  
Norman, OK 73069

### 1.0 INTRODUCTION

Mesocyclones are rotating regions associated with intense updrafts in a severe thunderstorm. They usually contain two flow regimes: an inner core where the velocity is proportional to the radius (a Rankine combined vortex), and an outer region where the velocity decreases with the inverse of the radius (a potential vortex). Rotational velocities are then greatest along the periphery of the inner core.

The core region tends to be sufficiently large and strong to be readily detected by a single Doppler radar. Since Doppler radar senses motion only along its beam, it senses the mesocyclone circulation only on two sides where motion is directed either toward or away from the radar. The result is a characteristic signature that consists of a maximum-minimum radial velocity couplet in close proximity to each other.

While severe weather events, especially intense tornadoes, usually have associated intense and persistent rotation, not all rotation events within thunderstorms are associated with severe weather. Rules for discriminating mesocyclones from transient rotation events were established by the Joint Doppler Operational Project (JDOP) (Burgess, et al., 1979) following extensive data analysis. Hennington and Burgess (1981) then took these rules and developed an algorithm for automatic mesocyclone detection. With a high degree of success their algorithm distinguished cyclonically rotating mesocyclones from other shear feature types and was selected for use by the Next Generation Weather Radar (NEXRAD). This version of the algorithm will be referred to here as the NEXRAD algorithm. Wieler and Donaldson (1983) enhanced this algorithm to enable the additional detection of Tornadoic Vortex Signatures (TVSs) and anticyclonic features. In this paper we present a further enhancement that results in improved discrimination capabilities for features and more accurate estimation of mesocyclone core related parameters. The structure and performance of this better algorithm, herein referred to as the STX algorithm, is compared to the NEXRAD algorithm.

### 2.0 AUTOMATED MESOCYCLONE DETECTION

#### 2.1 GENERIC ALGORITHM STRUCTURE

Current mesocyclone detection algorithms rely on the same basic infrastructure in order to detect mesocyclones. There are four primary construction steps:

- 1) Azimuthally oriented shear is identified in the Doppler velocity field. Across a mesocyclone

core the velocity gradient is constant in sign and is readily identified. At each range gate interval a search is made in the azimuthal direction for segments where the velocity gradient has the same sign. These segments, called Pattern Vectors (PVs), are described by range, beginning and ending azimuths, and velocities.

- 2) PVs from a single elevation scan are combined into two-dimensional (2-D) features.

- 3) 2-D features from multiple elevations are combined into three-dimensional (3-D) features.

- 4) 3-D features are tested for mesocyclone qualification.

Important differences between the algorithms occur in the methodology used in these construction steps. In the discussions that follow, the focus will be on the methodologies of the algorithms and how the methodologies affect the performance of the algorithms. Threshold magnitudes are generally not presented in order to emphasize technique.

#### 2.2 NEXRAD ALGORITHM CONSTRUCTION

Both algorithms are designed to operate in a real-time environment. To minimize processing overhead the methods were developed to minimize the total number of PVs retained by the algorithm while still retaining all mesocyclone associated PVs. For the NEXRAD algorithm, mesocyclone associated PVs are identified with thresholds on momentum and shear.

Once PVs are assembled, 2-D features are constructed by matching PVs that are close in range and azimuth. In order to eliminate noise, feature retention is limited to those containing a threshold number of PVs.

Pattern vectors contain valuable information about the mesocyclone core region that can be used to distinguish mesocyclones from other types of shear features. Parameters, such as core dimensions, rotational velocity, and shear, are estimated in the NEXRAD algorithm by the averages of PVs with modification by a momentum factor that emphasizes the largest and most sheared PVs. These parameters are then used to determine if a 2-D feature has the characteristics of a mesocyclone, namely that the feature is somewhat circular and has mesocyclonic shear. Because mesocyclone sampling is degraded with range, symmetry criteria are relaxed beyond a prescribed range from the radar. Requirements for shear do not change, however.

In the construction of three-dimensional features, 2-D features from different elevations are grouped together into a 3-D feature upon satisfying separation criteria. These criteria are unique to each 2-D feature and are a function of feature diameter. Once assembled, 3-D

\*This work was performed under AFGL contracts F19628-82-C-0023 and F19628-87-C-0124.

features are tested for qualification as mesocyclones. This requires only that two or more of the 2-D features within a 3-D feature have mesocyclone characteristics.

### 2.3 STX ALGORITHM CONSTRUCTION

Some problems (to be outlined below) have arisen with the NEXRAD algorithm and with the Wieler and Donaldson algorithm. These appear to be based not in the basic algorithm structure but rather in some of the methodology used in the mesocyclone construction steps. The STX algorithm was designed to eliminate these problems so that its analysis of mesocyclones would more closely replicate that of a human being. Since the NEXRAD and STX algorithms contain the same generic structure it is instructive then to outline some difficulties with the NEXRAD algorithm along with the improvements in the STX algorithm that ameliorate these difficulties.

Use of a momentum criterion by the NEXRAD algorithm implies a variable lower limit on the size of PVs that can be detected. Momentum thresholding will often prevent TVS detection unless they are very large and intense. In situations when a mesocyclone 'wraps up' into a TVS some PVs of the mesocyclone may go undetected by the NEXRAD algorithm resulting in an incompletely sampled circulation. The STX algorithm uses a simpler approach to pattern vector retention based on shear and velocity difference across a PV. These parameters are suitable for mesocyclone detection as are the NEXRAD parameters, but because they are sensitive to feature energy and not dependent on feature size they permit TVS detection as well. STX thresholds are not fixed but vary according to the relative sizes of the beam and vortex. This is especially important for TVS detection throughout the first-trip range interval.

In the construction procedure for 2-D features the NEXRAD algorithm combines together PVs that are adjacent in range if their centers are within a prescribed azimuthal separation. This leads to a problem for some PVs with small azimuthal diameters. Some 2-D feature elements, adjacent in range, are allowed to be disjunct by the NEXRAD algorithm if the sum of their azimuthal diameters is less than four degrees. Since this is not an observed property of mesocyclone cores, feature elements of the STX algorithm are required to be contiguous.

During the development stages of the STX algorithm it was discovered that the number of potential 2-D features often exceeded the design capacity of the algorithm. Rather than increase the 2-D feature capacity it was decided to eliminate unwanted features with detection criteria based upon circularity and shear of 2-D features. While the NEXRAD algorithm design does not specify an upper limit for the number of 2-D features, the version used in this investigation, obtained from the National Severe Storms Laboratory (NSSL), had a limit of 40. This was found sufficient for the cases examined in this study.

The NEXRAD algorithm is not accurate for estimating mesocyclone core parameters. That is because it assumes that the core is well represented by the continuum of PVs when in fact true rotational velocity is measured only at the points where motion is directed toward or away from the radar. Therefore the use of momentum weighted means of shear and diameter computed over the entire mesocyclone as used by the NEXRAD algorithm will not produce meaningful results. Feature parameters of the STX algorithm are based

upon the location and magnitude of the incoming and outgoing velocity maxima of the core. This method permits an estimation for mesocyclone core orientation so that rotational velocity can be adjusted for divergence. Mesocyclone features are also adjusted according to the theoretical profiles of how a radar views a Rankine combined vortex (Brown and Lemon, 1976).

It is common for unrelated shear regions or velocity couplets to exist in the vicinity of a mesocyclone. When they do it is important that they not be mistaken as mesocyclone components. In order to better assure reliable mesocyclone construction the STX algorithm identifies all 2-D feature candidates of the same elevation scan that qualify for inclusion into a 3-D feature. From these a selection is made based upon distance and shear. The NEXRAD algorithm does not go through such a selective process. A 3-D feature is matched with any 2-D feature that satisfies the overlap criteria, regardless if better combinations exist.

When the number of 3-D features exceeds the design capacity of the STX algorithm, those features that appear least likely to be mesocyclones are discarded. Feature elimination is based upon the degree of circularity and three-dimensional structure. In this scheme elongated shear areas are the first features discarded. Feature capacity is not specified in the NEXRAD algorithm.

STX mesocyclone classification criteria mirror those from JDOP: mesocyclone shear must exist over a prescribed thickness and over a time period of at least that of one half the feature rotation period. The STX algorithm requires the additional constraints that a 3-D feature be somewhat circular and that it has a vertical divergence distribution that does not deviate from the standard model of mesocyclones (Burgess, et al., 1979). These additional criteria were, in part, derived from a detailed, manual analysis of over twenty mesocyclones. NEXRAD criteria are much more lenient than the JDOP rules in that they do not specify a minimum thickness for mesocyclonic shear, mesocyclonic shear to be contiguous in the vertical, and persistence. The lack of a persistence requirement, in particular, may well result in a high percentage of false alarms in the NEXRAD algorithm.

As a consequence of the STX algorithm's persistence requirement for mesocyclone identification it became necessary to develop tracking capabilities, because persistence is not always satisfied within a single volume scan period. All 3-D features are tracked regardless of classification to enable the entire history of a mesocyclone to be monitored.

### 3.0 ANALYSIS

#### 3.1 DATA SOURCE

From March 15 to June 15, 1987 the DOPLIGHT '87 (Doppler Lightning Program) was conducted at NSSL. One objective of the program was to closely simulate the NEXRAD data collection format in order to test performance of a number of algorithms destined for use in NEXRAD. Azimuthal resolution was mandated at 1 degree, and vertical scanning increments were 1 degree for the first 5 elevations with subsequent larger increments at higher elevations. The total number of elevation scans generally varied between six and nine, and while this resulted in a degraded vertical resolution over that obtainable with the NEXRAD systems, it was

necessary to obtain reasonable volume scan update times of 6 to 10 minutes.

The 1987 tornado season in Oklahoma was rather uneventful with only 12 tornado days occurring during DOPLIGHT '87. Most of the tornadoes were weak, but a couple with F-2 intensity occurred in western Oklahoma. Large hail (1 inch or larger) was a more frequent weather event, occurring 21 days of the program. Most of these events did not have mesocyclones associated with them and any mesocyclones that did exist were generally neither intense nor persistent.

Table 1. Storm analysis.

date	time (CST)	location az.,rng. (deg),(km)	analysis / levels with (structure only) / mesocyclonic shear		
			manual	STX	NEXRAD
5/19	1619	356, 63	C/3	C/2	miss
5/19	1629	356, 67	M/4	M/2	miss
5/19	1639	353, 72	C/2	C/1	U/1
lag time (min) —>				0	n.a.
5/19	1619	159,110	C/3	C/2	U/1
5/19	1629	159,106	M/4	M/2	U/1
5/19	1639	158,100	M/5	M/4	U/1
lag time (min) —>				0	n.a.
5/26	1858	323,118	M/4	C/2	miss
5/26	1904	323,117	M/3	C/0	miss
5/26	1911	329,116	C/2	M/2	U/0
5/26	1918	335,117	M/4	C/1	U/1
5/26	1925	340,122	M/4	M/2	U/1
5/26	1932	339,124	M/4	M/3	S/1
5/26	1938	344,126	C/3	C/1	M/1
5/26	1945	345,128	M/4	M/2	U/1
5/26	1952	347,128	M/4	C/0	U/1
5/26	1958	350,131	C/2	S/2	U/1
5/26	2006	354,134	M/3	C/2	C/2
lag time (min) —>				14	28
5/26	1952	355,152	n.a.	M/3**	U/0**
5/26	1958	359,152	n.a.	C/0**	M/1**
5/26	2006	2,156	n.a.	C/1**	U/1**
lag time (min) —>				n.a.	n.a.
6/15	2030	195, 55	M/7	C/4	U/1
6/15	2040	198, 54	M/7	M/5	M/1
6/15	2050	201, 56	M/6	C/4	miss
lag time (min) —>				10	10
6/15	2040	163, 64	M/5	C/3	miss
6/15	2050	169, 61	M/2	M/2	miss
lag time (min) —>				10	n.a.

\*\* byproduct of an aliased velocity field

LEGEND:

U - single elevation feature  
S - multiple elevation nonsymmetric feature  
C - multiple elevation symmetric feature  
M - mesocyclone

The season was useful for the purposes of this investigation. There is little doubt that either the NEXRAD or STX algorithms could identify intense, well defined mesocyclone circulations such as those that produced the F-4 rated 1978 Piedmont, OK and 1981 Binger, OK tornadoes. A more respectable challenge to algorithm performance is how well it detects borderline mesocyclone circulations. Although weak mesocyclones are unlikely to produce significant tornadoes, their detection is important because they are still associated with large hail and strong winds. From the archives of DOPLIGHT '87, five test cases were selected. A number of these cases were classified as mesocyclones by meteorologists at NSSL, while others were thought to be marginal for mesocyclone classification. This mix of feature types provides a good test bed for algorithm performance.

### 3.2 ANALYSIS METHOD

Both algorithms were run on the test data. Whenever a feature was identified as a mesocyclone by either the NEXRAD or STX algorithm the data was subjected to an independent analysis to establish a ground truth by which the algorithms could be compared. This analysis consisted of two parts:

- 1) Manual analysis of the data through use of B-scans.
- 2) Application of JDOP rules for for verification of mesocyclones.

Features suspected or verified as mesocyclones through this method were tracked manually for their duration or until the data was exhausted in order to establish their history.

In order to facilitate performance evaluation of the algorithms, it is necessary to standardize the classifications made by each. Since the NEXRAD algorithm categorizes a feature as a mesocyclone based entirely upon its vertical structure this method will be referred to as a structure classification. Mesocyclone identification by JDOP rules and the STX algorithm, which require structure and persistence, shall be referred to as a persistence classification. The ability of each algorithm to detect mesocyclones according to these two classifications was determined. Since persistence often requires tracking features between consecutive volume scans, and since no reliable method exists for tracking NEXRAD features, this was accomplished manually in order to simulate the persistence method in the NEXRAD algorithm.

### 3.3 RESULTS

A total of five mesocyclones existed within the first-trip range interval during the dates and study times examined. None of these were tornadic but two developed within storms that produced large hail. However, an F-1 tornado formed on May 19 about 80 km northeast of the radar, for which no associated shear feature was detected by either algorithm or by manual analysis.

One pertinent feature existed in the second-trip range interval during the study. This was a short-lived mesocyclone resolvable by manual analysis that formed in the Texas panhandle on May 24. Unfortunately, software problems at the writing of this paper prevented analysis of second trip data by the automated algorithms.

Table 1 presents the histories of the five first-trip mesocyclones. Feature locations shown were obtained from the STX algorithm and compare on average to within 1.6 km of the locations derived from manual analysis of the data. Features were classified using structure only and not persistence. 'Levels with mesocyclonic shear' refers to those 2-D features correctly identified by the algorithms as having mesocyclonic shear. 'Lag time' indicates the delay for mesocyclone classification by the algorithms compared to manual analysis when feature persistence is included.

Table 2A contains each algorithm's performance in detecting the 2-D features of a mesocyclone that have mesocyclonic shear. Performance criteria were adapted from the forecasting performance evaluation method of Donaldson, et al. (1975). To qualify as a hit, PVs of the mesocyclone core must be detected by the algorithms and shear must be indicated to be of mesocyclonic magnitude. Failure to satisfy these requirements qualifies as a miss. Levels indicated as having mesocyclonic shear that were found otherwise through manual analysis are labeled as false alarms. Although the sample is too small for absolute percentages to be meaningful, the relative performance of the algorithms can be appreciated. Neither algorithm completely duplicated the manual analysis, but the STX algorithm did outperform the NEXRAD algorithm. The probability of detection by the STX algorithm was higher and its false alarm rate was lower, in comparison with the NEXRAD algorithm. While the STX algorithm detected 83 percent of the 2-D features associated with mesocyclones, problems with estimating the locations of the extrema in the rotational

velocity appear to be a source for misses. On the other hand, the NEXRAD algorithm detected only 20 percent of the features associated with mesocyclones and therefore its misses appear to be due to this failure.

The success rate for identifying mesocyclones, based on their structure alone, is shown in Table 2B. No false alarms were produced by either algorithm, but the STX algorithm identified two mesocyclones that the NEXRAD algorithm missed. It is interesting to note that every mesocyclone identification by the NEXRAD algorithm was rather coincidental because none of its 3-D features ever contained more than one 2-D feature actually associated with the mesocyclone core. Large 2-D features that did not share vertical continuity were often combined together into the same 3-D feature by the NEXRAD algorithm.

Mesocyclone detection was found not to increase when feature persistence was included for the cases examined.

It is worthy of note that one other feature (on May 26) not included in this study resulted in both algorithms identifying a mesocyclone 150 km north of the radar. However, manual investigation of the data indicated no mesocyclone. In fact, no shear feature of any kind could be seen. This false alarm can not be directly attributed to the algorithms but rather to a corrupted velocity field. Aliased velocities associated with a mesocyclone located 20 km to the south were not unfolded correctly by the method employed for this study, and velocity data at subsequent ranges were corrupted. The resulting velocity field was perceived as a mesocyclone by both algorithms. The unfolding technique used is common and simple, attempting to unfold aliased velocity data by minimizing the radial velocity gradient. This technique is known for speed but not reliability. Better unfolding methods will have to be developed for NEXRAD if this problem is going to be avoided in the future. Because the false alarm was caused by faulty data and not the algorithms, the results of this were not included in previously discussed algorithm performance.

#### 4.0 CONCLUSIONS

A comparison was conducted between the NEXRAD and STX mesocyclone detection algorithms. The algorithms were tested on five weak mesocyclones. The STX algorithm detected all of the mesocyclones of the study, while two of the mesocyclones were missed by the NEXRAD algorithm. Neither algorithm produced false alarms when velocity data were correctly unfolded, but their performance was poor in the presence of velocity artifacts.

#### 5.0 REFERENCES

- Brown, R. A. and L. R. Lemon, 1976: Preprints, 17th Conf. on Radar Meteorol., 104-109.
- Burgess, D. W., 1976: Preprints, 17th Conf. on Radar Meteorol., 97-103.
- Burgess, D. W. and JDOP Staff, 1979: NOAA Tech. Memo., ERL NSSL - 86, 84 pp.
- Donaldson, R. J., Jr., R. M. Dyer, and M. J. Kraus, 1975: Preprints, 9th Conf. on Severe Local Storms, 321-326.
- Hennington, L. D. and D. W. Burgess, 1981: Preprints, 20th Conf. on Radar Meteorol., 704-706.
- Wieler, J. G. and R. J. Donaldson, Jr. 1983: Preprints, 13th Conf. on Severe Local Storms, 58-61.

Table 2. Algorithm performance.

A) event: single elevation feature containing mesocyclonic shear

	STX	NEXRAD
POD	57%	21%
FAR	8%	29%
CSI	55%	19%

B) event: mesocyclones (by structure only)

	STX	NEXRAD
POD	100%	60%
FAR	0%	0%
CSI	100%	60%

#### LEGEND:

- X = detect event which occurs
- Y = miss event which occurs
- Z = false alarm

$$\text{Probability Of Detection (POD)} = X/(X+Y)$$

$$\text{False Alarm Rate (FAR)} = Z/(Z+X)$$

$$\text{Critical Success Index (CSI)} = X/(X+Y+Z)$$

The U.S. Government is authorized to reproduce and sell this report.  
Permission for further reproduction by others must be obtained from  
the copyright owner.

## Improvement of Tornado Warnings by Doppler Radar Measurement of Mesocyclone Rotational Kinetic Energy

RALPH J. DONALDSON, JR. AND PAUL R. DESROCHERS

*ST Systems Corporation, Lexington, Massachusetts*

(Manuscript received 1 September 1989, in final form 15 November 1989)

### ABSTRACT

A significant improvement in the reliability and timeliness of tornado warnings can be achieved through quantitative measurement by Doppler radar of selected mesocyclone features. The mesocyclone, a midsize circulation found in some of the most severe thunderstorms, is a frequent precursor of tornadoes, especially those of strong or violent intensity. Mesocyclones can be readily detected by Doppler radar, and their distinguishing characteristics measured.

A small sample of 17 Oklahoma storms containing mesocyclones was investigated in an effort to find optimum tornado predictors. The mesocyclone characteristic that provided the basis for the longest and most accurate warnings for violent (F4 and F5) as well as strong (F2 and F3) tornadoes is excess rotational kinetic energy (ERKE), defined as the rotational kinetic energy of the mesocyclone core calculated after subtraction from mesocyclone rotational velocity of the product of core radius and a selected value of threshold mesocyclonic shear. Rotational velocity also offered a basis for excellent warnings of the strong tornadoes. Little or no skill was achieved for identification of weak (F0 and F1) tornadoes. However, the distinctive warnings possible for strong and violent tornadoes in this small sample, using ERKE, offer reasonable promise of similar results when next generation weather radar (NEXRAD) becomes operational.

### 1. Introduction

Accurate tornado warnings, combined with an alert and receptive public, can prevent personal injury and save lives. The reliability of tornado warnings should improve significantly during the next few years as next generation weather radars (NEXRAD) are installed throughout the United States and forecasters learn to use them effectively. The capability of Doppler radar to measure advancing and receding air motion provides a valuable source of information on storm processes frequently associated with developing tornadoes. This enables a greater probability of detection of tornadic storms and increased lead time before tornado touch-down. The use of Doppler radar should also reduce false alarms, which compromise the credibility of accurate warnings and might increase tornado casualties among skeptics insufficiently motivated to heed a valid warning.

The research reported herein represents an early stage in the development of a quantitative technique for the timely identification of tornadic storms. The results, using an Oklahoma dataset, appear to be very promising as an aid in warning of strong and violent tornadoes. Accordingly, this study is offered as background information to interested forecasters of severe

storms and tornadoes, who will eventually have the advantage of the augmented observing capability and automated products of the NEXRAD Doppler radars. We are motivated by our trust that operational forecasters will benefit from familiarization with ongoing developments of techniques that may lead to improved tornado warnings. The techniques discussed in our article may also contribute to the development and testing of algorithms useful for warning of strong and violent tornadoes in a variety of climatic regimes throughout the United States.

After a brief review of mesocyclone detection and its significance for tornado identification in section 2, the concept of excess rotational kinetic energy (ERKE) of a mesocyclone core is introduced in section 3. Some earlier results are presented, showing application of this concept for identification of subsequent tornadoes. ERKE is rotational kinetic energy of a mesocyclone core, calculated with a velocity diminished by a term proportional to core radius. The reasoning leading to adoption of ERKE as a tornado predictor, and the advantages it offers, are discussed in some detail in section 3. Current research, employing integration by height of ERKE, is discussed in section 4. Procedures for selection of optimum ERKE parameters are explained in this section, and resultant lead times and identification errors are given for three intensity classes of tornadoes. Finally, these ERKE results are compared with those achieved by several other mesocyclone features.

---

Corresponding author address: Ralph J. Donaldson, ST Systems Corporation, 109 Massachusetts Avenue, Lexington, MA 02173.

## 2. Historical background of mesocyclone detection

The key to reliable and timely identification by radar of strong and violent tornadoes is the mesocyclone. Brooks (1949) discovered evidence for a midscale circulation surrounding tornadoes, inferred through his study of a closely spaced network of surface pressure and wind trends. He named the feature a tornado cyclone, now known as a mesocyclone. A mesoscale analysis by Fujita (1958) of an Illinois tornado and its environment, using radar observations as well as all available surface data, confirmed Brooks' hypothesis.

Lhermitte (1964), in a theoretical treatment, anticipated the characteristic signature of a mesocyclone core viewed by a single Doppler radar. After observing Lhermitte's predicted velocity pattern in a severely damaging storm, Donaldson (1970) proposed criteria of shear, persistence, and vertical extent for validation of the single-Doppler signature of a mesoscale vortex or mesocyclone. This signature (Fig. 1) consists of a couplet of maximum (receding) and minimum (approaching) Doppler velocities at about the same range, and with the maximum velocities to the right of the minimum, as viewed from the radar. The distance across the couplet indicates the diameter of the high-vorticity core of the mesocyclone, and half the speed difference across the couplet is the maximum rotational velocity of the core.

Burgess (1976) conducted a search for mesocyclones by Doppler radar in Oklahoma. In a 5-yr period, he identified 37 mesocyclones, and found that 23 of these were accompanied by tornadoes. Furthermore, he

found that tornado-producing mesocyclones preceded tornadoes by half an hour, on average. Some form of severe weather accompanied all but two of these mesocyclones. This crucial study by Burgess laid the foundation for improved tornado warnings, and led to the Joint Doppler Operational Project (JDOP), an experiment designed for testing the reliability of Doppler radar in an operational scenario for detection of tornadoes and other severe storm hazards.

The results reported by the JDOP Staff (1979) are most impressive. The detection rate for tornadoes was 69%, with a false-alarm rate of only 25%. Most important for tornado warnings, the average lead time before tornado touchdown was 21 min. This is a significant improvement over the average 2-min. lead time achieved by the Oklahoma City Weather Service forecasters during the JDOP operations for tornado warnings prepared without benefit of Doppler radar. The Oklahoma City forecasters achieved a stunning tornado detection rate of 64%, nearly equal to the rate for JDOP and about three times the national rate for the same period reported by Pearson and David (1979), but their false alarm rate of 63%, though considerably below the concurrent national average of 93%, was significantly higher than that of JDOP. The superior JDOP warning performance validated the incorporation of Doppler capability in the NEXRAD radars.

The statistical relationship between mesocyclones and tornadoes suggests the possibility for mesocyclone classification that might provide a basis for further improvement of tornado prediction. Burgess (1976), however, found that average values of rotational ve-

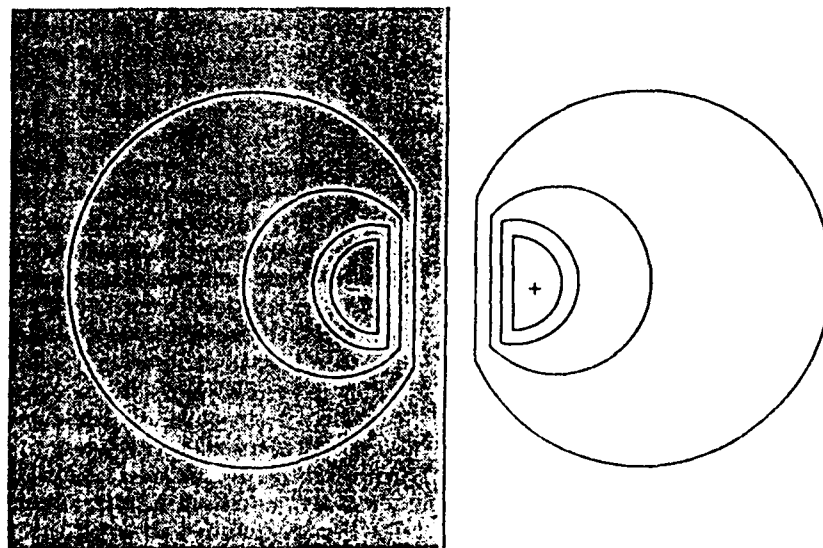


FIG. 1. Single-Doppler radar signature in plan view of a mesocyclone with pure rotation (no divergence) and no translational component, depicted by contours of Doppler velocity measured by a radar located at the bottom of the page. Positive velocities (white area) indicate motion receding from the radar; negative velocities (shaded area) indicate motion toward the radar. (Adapted from Donaldson 1970.)

locity, horizontal diameter, and vertical extent in his early sample of 37 Oklahoma mesocyclones were nearly equal to the corresponding average values of the tornadic subset. This was also the case in a recent survey article by Burgess and Lemon (1990), where they provided data on 45 "well-observed" mesocyclone signatures.

For both of his surveys, however, Burgess found encouraging characteristics that may lead to better forecasting of the large and violent maxitornadoes: Their precedent mesocyclones are distinctive in several respects from the general population of mesocyclones. These special mesocyclones tend toward somewhat smaller diameters and have larger rotational velocities, resulting in considerably greater shear (velocity divided by radius) across their cores. For example, in the Burgess and Lemon (1990) survey, all of the maxitornadic mesocyclones displayed shear of  $\geq 0.01 \text{ s}^{-1}$ , but more than half of the total number of mesocyclones in their sample failed to reach this high value of shear.

### 3. Development of the concept of excess rotational kinetic energy

Donaldson and Desrochers (1985) initiated an investigation of the rotational kinetic energy (RKE) of mesocyclone cores, in an effort to seek further improvements in tornado predictability. They assumed that the core region of a mesocyclone may be approximated fairly well by a cylinder of radius  $r$  and height  $\Delta h$ , in solid rotation around a vertical axis, with a maximum rotational velocity  $v$ . The rotational kinetic energy is given by  $I\omega^2/2$ , where  $I$  is the moment of inertia about the rotational axis, and  $\omega$  is the angular velocity, equal to  $v/r$ . The moment of inertia of a cylinder of mass  $m$  and radius  $r$ , rotating about its central axis, is  $I = mr^2/2$ . The mass of the cylinder is  $\rho\Delta h\pi r^2$ , where  $\rho$  is density. Finally,

$$\text{RKE} = I\omega^2/2 = \rho\Delta h\pi r^2 v^2/4. \quad (1)$$

Values of  $r$  and  $v$  are obtained through a search of the Doppler velocity field, at each elevation angle, for a couplet of velocity extrema at roughly the same range. These extrema are generally of opposite sign, unless the mesocyclone is moving toward or away from the radar at a translational speed greater than the rotational velocity. The radius  $r$  is half the distance between the velocity extrema, and the rotational velocity at the core perimeter is half the algebraic difference between the velocity extrema, multiplied by a factor  $\cos\phi$ . The angle  $\phi$ , measured between a line joining the velocity extrema and a constant-range line, indicates the presence of divergent (or convergent) components across the core (cf. Wood et al. 1986), and in these instances pure rotational velocity is isolated by the factor  $\cos\phi$ . Values of  $\rho$  (air density) as a function of height were taken from the 30°N July table in the U.S. Standard Atmosphere Supplement (1966). Energy calculations were performed in joules/meter by setting  $\Delta h = 1 \text{ m}$ .

A quantitative technique is required to distinguish those couplets indicating that rotation is likely from those wherein rotation could be in doubt. The traditional criterion for rotation used with single-Doppler radar is the mesocyclonic shear threshold  $S_m = v/r = 0.005 \text{ s}^{-1}$  suggested by Donaldson (1970) and confirmed by Burgess (1976) as suitable for identification of Oklahoma mesocyclones. Acceptance of this shear threshold—or any subsequent revision of it—as a condition of rotation necessarily discards shear regions that almost, but not quite, reach the threshold. Although the product of  $r^2$  and  $v^2$  might be very large in these submarginal shear regions, its failure to reach the standards set up for rotation would require its *rotational* kinetic energy to be considered as zero. On the other hand, a shear region with the same velocity increment but occurring over a slightly smaller distance might barely achieve the requisite mesocyclonic shear threshold and have its very large RKE considered legitimate. Slight errors in measurement of  $r$  and/or  $v$ , or a small adjustment of the threshold, could result in undesirably large variability in the resultant product.

Consequently, Donaldson and Desrochers (1985) removed these threshold-induced ambiguities by introducing the concept of *excess* rotational kinetic energy. In their formulation, the rotational kinetic energy is calculated with a diminished velocity, given by subtraction of the velocity ( $rS_m$ ) required to achieve mesocyclonic shear ( $S_m$ ) for the measured radius ( $r$ ) from observed rotational velocity ( $v$ ). The resultant diminished velocity ( $v - rS_m$ ) can be regarded as excess to the minimum required for the maintenance of mesocyclonic shear. This formulation provides a smooth transition from zero to finite rotational energy values as the shear threshold is crossed. Accordingly,

$$\text{ERKE} = \rho\Delta h\pi r^2(v - rS_m)^2/4, \quad (2)$$

with  $S_m$  provisionally equal to  $0.005 \text{ s}^{-1}$ . Negative values of  $(v - rS_m)$  are considered as zero ERKE. If indicated by further research, ERKE is readily adaptable to a revised value of threshold-mesocyclonic shear.

The ERKE formulation of (2) can be envisioned by depiction on a diagram (Fig. 2) with mesocyclonic core velocity and radius as axes. The straight line on this diagram is threshold mesocyclonic shear, with a selected value of  $0.005 \text{ s}^{-1}$ . The region to the left of this line is the domain of the traditional mesocyclone. The contours represent various values of ERKE divided by the ERKE of an average mesocyclone in its strongest stage of development, found by Burgess et al. (1982) to have a core radius of 2.75 km and rotational velocity of 23.3 m/s. This corresponds to an ERKE/m of 540 MJ/m, which is renamed 1 CMM (climatological mature mesocyclone).

The ERKE curves are hyperbolas, asymptotic to the  $r = 0$  axis on the left and the threshold mesocyclonic shear line on the right. Increasing values of ERKE require higher values of both velocity and shear. It seems



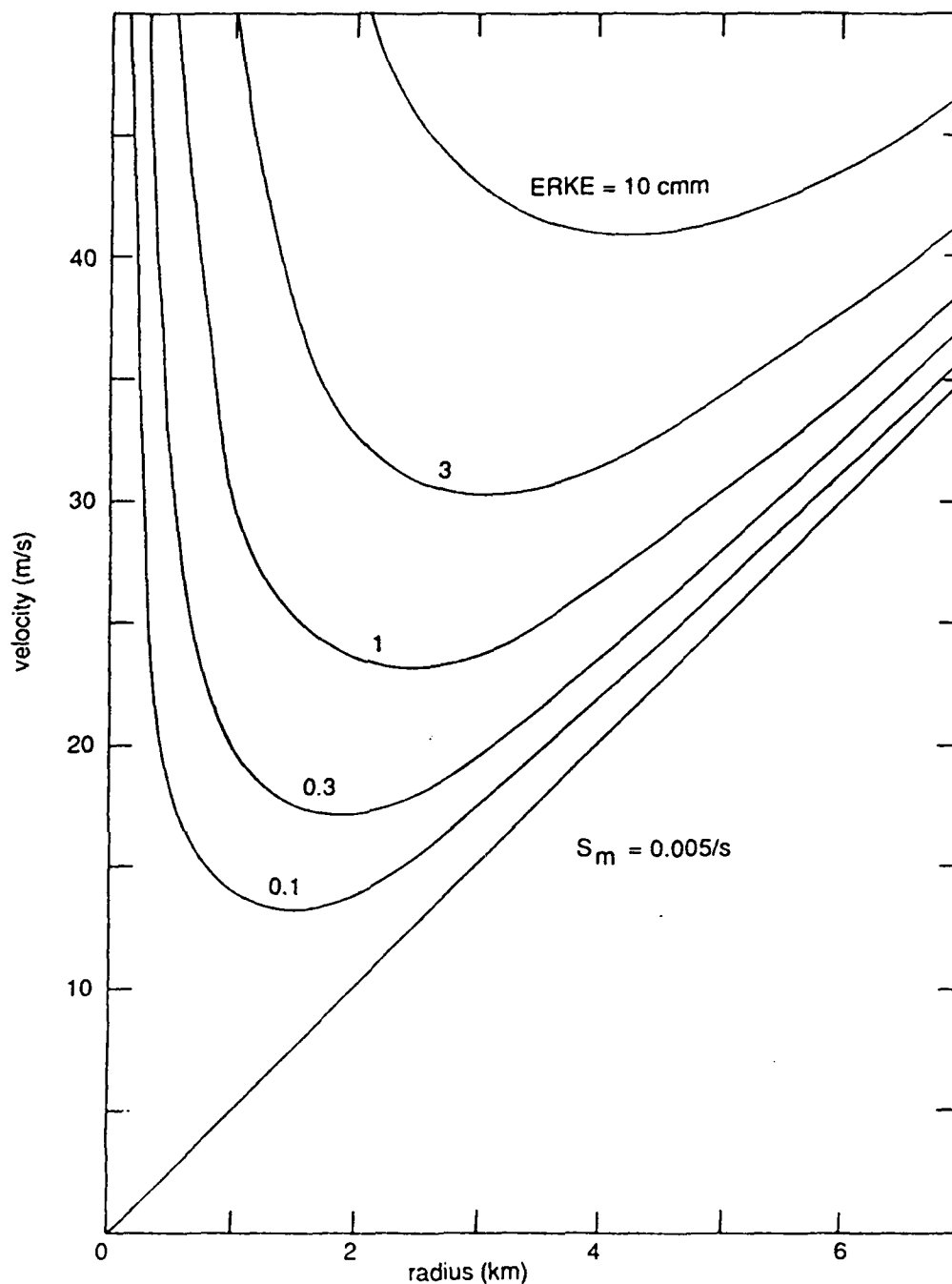


FIG. 2. Contours of constant ERKE values plotted as a function of mesocyclone rotational velocity and core radius. Values are expressed as a fraction or multiple of 1 CMM, the ERKE equivalent of a climatological mature mesocyclone. The straight line is  $S_m$ , threshold mesocyclonic shear, shown here with a value of  $0.005 \text{ s}^{-1}$ .

advantageous to accomplish this quantization of mesocyclones with a single function that has no discontinuities, rather than a combination of two or more functions. Another advantage of ERKE is the exclusion of very small values of radius, which often represent

artifacts in the Doppler velocity field with no meteorological significance. Still another advantage of ERKE is its relative insensitivity to antenna resolution errors because it depends on the product of radius and velocity. Brown and Lemon (1976), in their theoretical

study of the effects of varying resolution on measurement of a Rankine combined vortex that simulates a mesocyclone, showed that, in a condition of poor resolution, the core radius is overestimated somewhat, while the rotational velocity is underestimated.

Desrochers et al. (1986) presented some promising results on the application of the ERKE concept to mesocyclone classification. They examined ten mesocyclonic storms observed throughout their lifetimes by the National Severe Storms Laboratory (NSSL) Doppler radar facility at Norman, Oklahoma. The observations were recorded as a succession of volumetric scans, each scan consisting of a series of plan-view slices through the storm at successive antenna elevation angles. Most of the volumetric scans covered the entire height extent of the mesocyclonic circulations, though a few terminated at altitudes as low as 7 km. Five of these storms produced tornadoes, and two of the tornadic storms produced violent maxitornadoes, rated F4 on the intensity scale established by Fujita (1971, 1981). This sample frequency of tornado occurrence is consistent with the general Oklahoma experience for mesocyclones. However, the proportion of storms releasing violent (F4 or F5) tornadoes—two of the ten—is undoubtedly much higher than nature provides (Kelly et al. 1978).

Corrections were made in vortex size and rotational velocity for antenna beam resolution, following the

guidance offered by Brown and Lemon (1976). This correction is intended to free the ERKE measurements from a dependence on range. Comparison among storms was further facilitated by dividing all values of ERKE/m by 540 MJ/m, in order to express them in terms of CMM.

The mesocyclone life cycle within each of the ten storms was studied by locating the maximum value of ERKE/m and its weighted height during each volume scan. Some examples are illustrated in Fig. 3 portraying significant differences among the three storm types. The Ada storm (Fig. 3a) did not release a tornado, though it did produce large hail. The high values of ERKE/m,  $\leq 2$  CMM near the beginning and  $\geq 1$  CMM on two succeeding observations, occurred with weighted height above 5 km. In contrast, the two tornadic storms (Figs. 3b and 3c) reached high values of ERKE/m when their weighted height had descended below 5 km. ERKE/m values in the lower troposphere prior to and during tornado occurrence persistently exceeded 1 CMM, a pattern not apparent in the nontornadic mesocyclones. The Binger storm (Fig. 3c) persistently attained ERKE/m values well above 2 CMM before and during its violent F4 tornado.

The intensity of each tornado in all five of the tornadic storms did not correspond with the ERKE/m magnitude detected just prior to tornado occurrence. Rather, the maximum ERKE/m value observed during

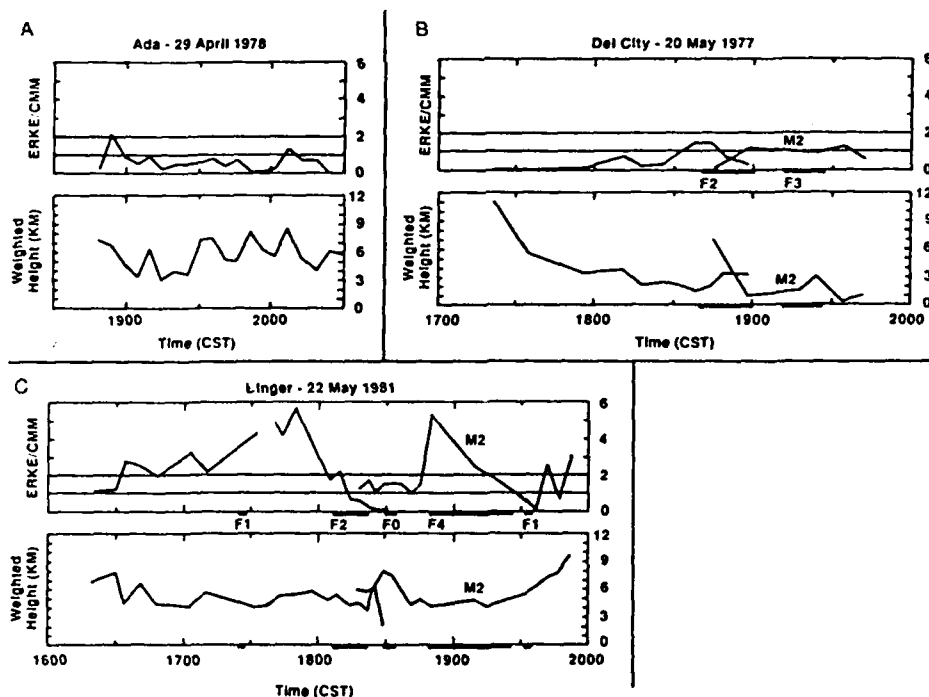


FIG. 3. Lifetime of three Oklahoma storms in terms of ERKE magnitude (upper part of each figure) and weighted-mean height of ERKE (lower part). Tornado intensity is indicated by F-number and duration by the thick solid lines at the bottom of each figure. The second mesocyclone is labeled "M2" in the two tornadic storms, Figs. 3b and 3c. (After Desrochers et al. 1986.)

the lifetime of a tornadic storm seemed to correspond with and *anticipate* the most intense tornado produced by the storm. Therefore, Desrochers et al. (1986) suggested a simple rule to distinguish tornadic from non-tornadic mesocyclones: One or more tornadoes are predicted if the mesocyclone attains an ERKE/m value of at least 1 CMM at a height below 5 km, and persists in this condition for at least 5 min. Nine of the ten storms were correctly forecast by this rule. The tornado predictive rule was slightly modified for violent tornadoes, by requiring ERKE/m of 2 CMM to persist for at least 5 min at a height below 5 km. Both of the storms with violent maxitornadoes were correctly forecast in this way, with no false alarms.

The warning lead times were calculated with the addition of 5 min to the beginning of each volumetric scan to allow for its completion. Results were not encouraging for the *first* tornado in each storm, because three of these tornadoes had negative lead times of -3 to -8 minutes. For the most intense nonviolent tornado in each storm, however, the lead times were all positive, ranging from 13 to 63 minutes. For the two violent (F4) tornadoes, which are rare but disproportionately dangerous to human life and well-being, the lead times using 2 CMM as a threshold were 20 and 72 min, providing adequate opportunity for people in the threatened area to seek shelter or move to a safer location.

#### 4. Integration of ERKE with height

The early results of Desrochers et al. (1986) for prediction of tornado occurrence were achieved through two-dimensional (2-D) calculations of ERKE, specific to a particular altitude, and dependent on a high value of ERKE/m appearing below a threshold altitude of 5 km. We now feel that more reliable results can be achieved by integrating the observations of ERKE/m from ground level up to some standard height above ground. There are two advantages in using an average value of ERKE throughout a column. First, there is less dependence on a single observation that might be affected by a measurement error or scanning strategy, as well as a requirement for some degree of consistency in the mesocyclone energy structure. Also, the results are much less sensitive to height thresholding. In the earlier work a descent of high energy from 5.0 to 4.9 km could trigger a warning, and such a high degree of sensitivity to measurement error or to an isolated anomaly in the energy profile seems undesirable.

The calculations of ERKE within a specified column are performed by integrating along a curve connecting all values of ERKE/m at the various heights given by antenna elevation angle and range. At the earth's surface, the value of ERKE/m is considered to be zero in the calculation of integrated ERKE.

The optimum height limits for the most productive tornado warnings by integrated ERKE will be deter-

mined only after installation and shakedown of the NEXRAD system enables the acquisition of a large sample of mesocyclonic data. This is also true for the optimum value of threshold shear ( $S_m$ ) for generation of ERKE in (2). It is likely, also, that these optimum height limits and shear thresholds will vary regionally, and perhaps seasonally and diurnally as well.

#### a. Selection of optimum predictors

Meanwhile, the small sample of storms presented here can provide an overview of candidate tornado predictors and indicate productive directions for analysis of the large sample of data expected to be available in the next few years. Our sample now comprises 17 Oklahoma storms, including the 10 reported by Desrochers et al. (1986) and 7 additional ones. All of the storms were observed within ranges of 160 km by one or the other of two NSSL Doppler radars. These radars operate at a wavelength in the 10-cm band and have half-power antenna beamwidths slightly less than  $1^\circ$ , so they are comparable in design to the NEXRAD radars.

The storms were observed during 5 years in April, May, and June. All of the storms occurred during the late afternoon and early evening hours, with all mesocyclones active within the 1600 to 2100 CST period. Eight of the 17 storms produced a total of 23 tornadoes, including 2 of violent (F4) intensity, 11 strong (F2 and F3) tornadoes, and 10 weak (F0 and F1) tornadoes. No tornadoes were reported with the other nine storms. The occurrence and intensity of the tornadoes were determined by storm chase teams and poststorm surveys organized by NSSL.

These 17 mesocyclonic storms were subjected to intense scrutiny. Calculations of ERKE at each volumetric scan for all storms were integrated over height intervals from ground level to 4, 5, 6, and 7 km above ground, using values of 0.004, 0.005, 0.006, and 0.007  $s^{-1}$  for threshold mesocyclonic shear  $S_m$  in (2). (Integrating heights below 4 km were not considered, in order to avoid reduction in data at great ranges.) All values were expressed in terms of CMM, the climatologically mean mature mesocyclone given by Burgess et al. (1982), by integrating the Burgess statistics for each of the 16 combinations of height and shear to arrive at the corresponding CMM values.

A persistence function was also considered, as Desrochers et al. (1986) had done with their 2-D technique. A casual inspection had revealed a tendency for the more active tornadic storms to exhibit high values of ERKE during several or more consecutive observations. Consequently, for all of the ERKE candidate predictors we produced a corresponding set of 10-min persistence values by selecting the minimum instantaneous value occurring during the 10-min period preceding each volume scan, interpolating where necessary. Comparative evaluation revealed that the persis-

tent predictors were superior for some cases, but for others the instantaneous values were better.

The resultant set of ERKE candidate predictors was evaluated by statistical analysis, by the number of correctly forecasted storms in our sample, and by the lead times achieved for the strong (F2 and F3) and violent (F4) tornadoes. The statistical analysis, discussed in more detail in the Appendix, developed  $t$ -statistics, i.e., ratios of mean difference to standard deviation of two distributions. These ratios, expressed as  $t_v$  and  $t_{nv}$ , provided an assessment of the significance of the mean difference in maximum ERKE values between storms producing violent tornadoes and our total sample, and between the nonviolent tornadic storms and those without tornadoes, respectively. The  $t_v$  and  $t_{nv}$  values were used for selection of the optimum predictors. Also, values of  $t_v$  and  $t_{nv}$  above 3 suggest a less than 1% probability that the observed differences are a chance occurrence.

The statistical analysis revealed optimum values of  $S_m$  (threshold-mesocyclonic shear) and  $h$  (maximum height for integrating ERKE). Results are depicted in Fig. 4, where the two ratios  $t_v$  and  $t_{nv}$  are plotted as a function of  $S_m$  for  $h = 4$  km (left side), and as a function of  $h$  for  $S_m = 0.006 \text{ s}^{-1}$  (right side). The violent tornadoes have greater  $t$  values for 10-min persistence, so  $t_v$  is plotted in Fig. 4 for this condition. It is immediately apparent that higher values of  $S_m$  are better for both predictors, tornadoes in general as well as the violent ones, up to a peak at  $S_m = 0.006 \text{ s}^{-1}$  or slightly greater.

The effect of  $h$ , the height of the top of the column in which ERKE is integrated, is depicted in the right half of Fig. 4. The greatest separation between the tornadic and nontornadic storms is achieved in our sample

with the lowest value of  $h = 4$  km. This is true not only for our adopted value of  $S_m = 0.006 \text{ s}^{-1}$ , but for the other values of threshold shear as well. It is not at all clear why this is so, and whether this condition is peculiar only to our sample, or will prove to be general.

On the other hand, it is not surprising to find that utilizing the greatest height for integrating ERKE (7 km) provides the most opportune separation of violently tornadic storms from all the others. The early mesocyclone statistics of Burgess (1976) show that the average vertical extent of maxitornado mesocyclones is 9.5 km, exceeding the average of all the other mesocyclones by 2 km. The top limit of  $h = 7$  km was chosen for our sample because in a few of our storms, including one of the two storms with a violent tornado, the data did not go above 7 km because of limited elevation angles in the radar scanning program. However, in the other violent tornadic storm there were three persistent episodes when ERKE with  $S_m = 0.008 \text{ s}^{-1}$  would have appeared at heights of  $\geq 8$  km, and all three episodes occurred before touchdown of the violent tornado. None of the other storms displayed such excess energy at such a great height. In view of this fact, as well as the results of Burgess' pioneer statistical study of mesocyclones, we believe that the optimum top height for integrating ERKE for the important purpose of warning against violent tornadoes may exceed our provisional value of  $h = 7$  km by 1 or 2 km when a much greater volume of data is analyzed during the NEXRAD era.

#### b. Lead times and identification errors for ERKE

Tornado warning lead times depend not only on the magnitude of predictor differences between tornadic

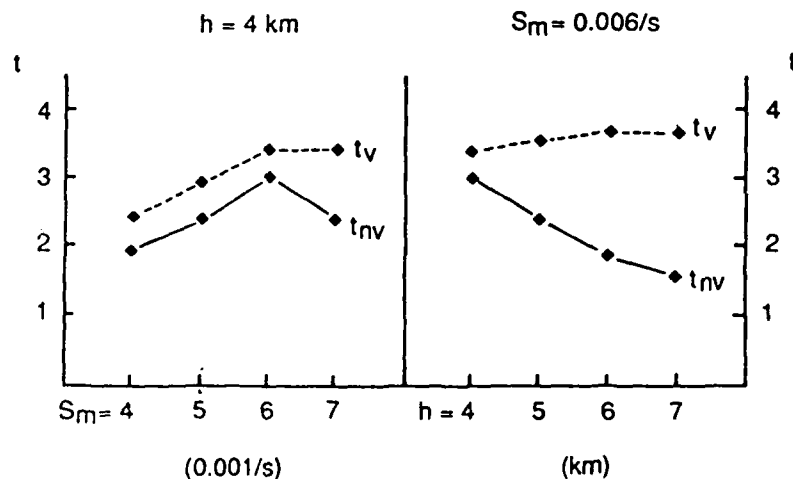


FIG. 4. Selection of optimum ERKE parameters for tornado warning, using ratios  $t_v$  and  $t_{nv}$  discussed in the Appendix. Solid lines are instantaneous values of  $t_{nv}$ ; dashed lines are 10-min persistence values of  $t_v$ . Left side of figure shows variation of  $t_v$  and  $t_{nv}$  as a function of threshold mesocyclonic shear ( $S_m$ ) for integrating height  $h = 4$  km. Right side shows variation of  $t_v$  and  $t_{nv}$  as a function of  $h$  for  $S_m = 0.006 \text{ s}^{-1}$ .

and nontornadic mesocyclones, but also on the stage in mesocyclone life cycle when a tornado predictor rises to prominence, and ultimately on the tornado warning threshold level chosen by the forecaster community. At one very safe extreme, one could decide that the smallest value of an ERKE predictor could trigger a tornado warning, in which case all tornadoes associated with a mesocyclone would receive the maximum lead time, but at the cost of a maximum number of false alarms. On the other hand, if false alarms were regarded as totally undesirable, the tornado warning threshold could be set at such a high level that some tornadoes might escape detection, and the others would have minimal warning times.

For our evaluation of tornado predictors, we have bypassed the perils of subjective decisions about the optimum conditions for a tornado warning. Instead, we have adopted objective thresholds, determined for violent tornadoes by the midway point between the mean of the maximum predictor value for violent tornadoes and the corresponding mean for nonviolent tornadoes. Similarly, the objective threshold for nonviolent tornadoes is the midway point between the mean of the maximum predictor value for nonviolent tornadoes and the corresponding mean for mesocyclones without tornadoes. Lead times are determined by interpolation between observation completion times to find the first minute that shows the predictor value exceeding the threshold value.

We have also calculated lead times from an adjusted threshold, defined as the lowest threshold value that would avoid an increase in the number of false alarms existent with the objective threshold. Practical lead times could probably be set somewhere between the limits determined by objective and adjusted thresholds.

The results achieved with ERKE as a tornado predictor are directly proportional to the intensity of the resultant tornado. For example, the two violent (F4) tornadoes were perfectly predicted with no false alarms, using a 10-min persistent value of ERKE calculated with  $S_m = 0.006 \text{ s}^{-1}$  and  $h = 7 \text{ km}$ . Both the objective and the adjusted lead times were more than adequate: 124 minutes (objective) and 134 minutes (adjusted) for the Binger storm of 22 May 1981 (discussed by Hennington et al. 1982, and Lemon et al. 1982), and 11 minutes (objective) and 28 minutes (adjusted) for the Piedmont storm of 30 April 1978 (discussed first by JDOP Staff 1979).

We can claim satisfying results, but not perfect success, for prediction of the nonviolent (F0 to F3) tornadic storms. As indicated earlier in Fig. 4, the optimum predictor for this class of storm is instantaneous (nonpersistent) ERKE calculated with  $S_m = 0.006 \text{ s}^{-1}$  and  $h = 4 \text{ km}$ . With an objective warning threshold, there were no false alarms, but one of the eight tornadic storms, a producer of two tornadoes, failed to reach threshold value at any time. In four other storms the first of several tornadoes touched down *before* the

warning threshold was reached. In other words, negative lead times prevailed for these early tornadoes. However, both of the undetected tornadoes, and all but one of the tornadoes detected after touchdown, were in the so-called weak category of F0 or F1.

Accordingly, the warning performance of ERKE for the 11 strong (F2 and F3) tornadoes in our sample is very good to excellent, leaving none of the tornadoes undetected. There was one false alarm triggered in a tornadic storm that produced only weak tornadoes. One of the strong tornadoes had a negative-lead time of  $-1 \text{ min}$ , but the mean lead time for all of the strong tornadoes was 27 min with an objective threshold and 29 min with an adjusted threshold. However, the warning performance of ERKE for the ten weak (F0 and F1) tornadoes must be considered only fair to poor, with two of them escaping detection entirely with the objective threshold, three others with negative lead times, and another with only a 2-min positive lead time. At the lower adjusted threshold, two weak tornadoes remained undetected and two others had negative lead times.

The comparative performance of ERKE for timely identification of the three intensity classes of tornadoes is illustrated in Fig. 5. The violent classification is represented by the Piedmont tornado (solid line), the less intense of the two F4 tornadoes in the sample, and therefore regarded as a conservative estimate of performance for violent tornadoes. Performance for strong (weak) tornadoes is given by the dashed (dotted) line.

The ordinate of Fig. 5 is the lead time achieved before tornado touchdown throughout the range of ERKE threshold values. Lead time is greatest for the smallest threshold values and decreases as the threshold is increased. For the strong and weak tornadoes, the measure of performance used is the *median* lead time before the *first* strong (or weak) tornado in a storm. The median, rather than mean lead time is used to minimize the skewing to greater values by the extraordinarily long lead times calculated for all of the tornadoes in the Binger storm. Also, when two or more tornadoes of a given class occur in the same storm, the lead time to the first tornado is regarded as more crucial for effective warnings.

The abscissa of Fig. 5 shows the combined error rate owing to false alarms and failures to detect. The false-alarm rate, for a given tornado-intensity class and threshold value, is equal to the number of storms incorrectly identified as a producer of one or more tornadoes of the same or greater intensity, divided by the total number of storms sampled. The rate of failures of detection, for a given intensity class and threshold value, is the number of tornadoes in that class not detected, divided by the total number of tornadoes in the class. The two kinds of errors are easily distinguished on this diagram, because, as lead time decreases, false alarms also decrease but failures of detection eventually increase. Accordingly, the portions of curves slanted

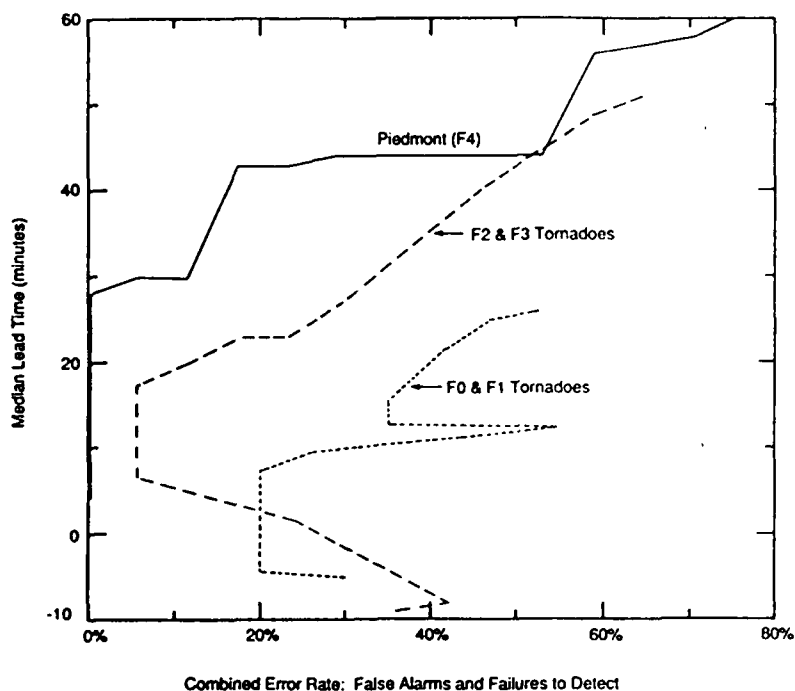


FIG. 5. Performance of ERKE as an aid in warning of three intensity classes of tornadoes: violent (solid line), strong (dashed line), and weak (dotted line). The ordinate gives median lead time for an intensity class, considering only the earliest tornado of that intensity in a storm. The abscissa shows combined errors expressed as the sum of false-alarm rate and failed detection rate.

upward and to the right indicate changes in false alarms, and where the curves slant downward and to the right, failures of detection are increasing. The vertical portions of the curves indicate a minimum in false alarms before failures of detection increase the error rate.

The type of curves depicted in Fig. 5 would be a useful forecasting tool when a sufficiently large sample of mesocyclone data becomes available to establish confidence in their reliability. For example, if a 20-min median lead time is regarded as essential, these preliminary data show the error rate to be zero, 12%, and 40% for violent, strong, and weak tornadoes, respectively, with all errors caused by false alarms. The corresponding error rates for a 10-min median lead time are zero, 6%, and 32%, with 20% of the 32% error rate for weak tornadoes caused by failure of detection. If a 10% combined error rate is acceptable, the corresponding median lead times would be 30 min for violent tornadoes, and 19 min for strong tornadoes; weak tornadoes would not be detected under such strict conditions.

The recent survey article by Burgess and Lemon (1990) suggests a 40% false-alarm rate for identification of tornadoes by mere detection of mesocyclones, with no attempt to classify them quantitatively. Figure 5 clearly shows that the ERKE technique demonstrates little or no skill in achieving an error rate below 40%

for predicting weak tornadoes. However, the ERKE technique does provide the basis for both accurate and timely warnings of the far more dangerous strong and violent tornadoes.

### c. Comparison of tornado predictors

A number of mesocyclonic features were examined to determine their accuracy for tornado prediction relative to ERKE. These included velocity ( $v$ ), shear ( $v/r$ ), rotational kinetic energy (RKE) as given by (1), and several measures of energy multiplied by shear. Each of these candidate predictors was averaged over height intervals of 0–4 and 0–7 km, and compiled with both instantaneous values and 10-min persistent values pertinent to each volume scan. For each predictor, the most warning-effective combination of averaged height and persistence or lack of persistence was selected for comparison with the other predictors.

Multiplication of rotational kinetic energy as given in (1) by shear ( $v/r$ ), and integration with height, yields a candidate predictor that we call RP because it has the dimensions of power, or energy per unit time:

$$RP = \bar{\rho} h \pi r v^3 / 4. \quad (3)$$

It is likely that RP has no physical relationship to temporal changes in rotational kinetic energy, but is merely

TABLE 1. Comparison of predictors for violent (F4) tornadoes.

Predictor	$t_v$	Storm errors	Lead time	
			Binger	Piedmont
ERKE (P) ( $S_m = 6$ , $h = 7$ )	3.70	0	124 (134)	11 objective (28) (adjusted)
Velocity ( $h = 7$ )	3.42	0	144 (144)	-7 (-5)
Shear ( $h = 7$ )	3.89	0	-18 (144)	-6 (-4)
ERP ( $S_m = 6$ , $h = 7$ )	3.61	0	-6 (-4)	-8 (-6)
Time-integrated (RP, $h = 7$ )	2.44	1 M 1 FA	51 (56)	M (M)
RP (P) ( $h = 4$ )	2.62	1 M	-15 (-15)	M (M)
RKE ( $h = 7$ )	Negative	2 M 5 FA	M (M)	M (M)

a way to express a product that emphasizes velocity at the expense of radius. Its dimension does, however, suggest the possibility of integrating the product of RP and time throughout the life cycle of a mesocyclone to produce another candidate predictor, time-integrated RP, that grows with time. Finally, we can multiply ERKE in (2) by excess shear above mesocyclonic threshold,  $(v - rS_m)/r$ , integrating with height to calculate excess RP, or ERP:

$$\text{ERP} = \bar{\rho} h \pi r (v - rS_m)^3 / 4. \quad (4)$$

The results of a comparison of all predictors are listed in Tables 1 and 2. The symbol (P) following a listed predictor indicates that 10-min persistence gave the best results for that predictor; no symbol indicates that the instantaneous values were best. Threshold mesocyclonic shears  $S_m$  are given in units of  $0.001 \text{ s}^{-1}$ , and

integrating heights  $h$  in kilometers. The ratios  $t_v$  and  $t_{mv}$  are discussed in the Appendix. Under the heading "Storm Errors," FA indicates a false alarm and M a missed detection, or failure to detect. The objective and adjusted thresholds for determination of lead times (listed in minutes) were discussed earlier, and lead times derived from the adjusted thresholds are listed in parentheses. In Table 2, mean-lead times for strong tornadoes were penalized for missed tornadoes by assigning a negative-lead time for each such failure to detect a strong tornado equal to tornado time of touchdown minus a time just beyond the final volume scan recorded for the parent storm. In both tables, our estimates of best predictors are listed in descending order.

Both tables indicate that ERKE and velocity are the only reasonable contenders for selection as a tornado predictor, with a slight edge to ERKE for nonviolent tornadoes and a decisive preference for ERKE as a predictor of violent tornadoes because of the negative lead times velocity gave for the Piedmont F4 tornado. The poor performance of shear and ERP for providing warnings of violent tornadoes—despite their very high values of  $t_v$ —is caused by the appearance of maximum values of these predictors in a tornadic vortex signature (Brown et al. 1978), when the tornado is already on the ground and it is too late for a warning. This is partially the situation for velocity as well.

It is interesting to compare the totally useless performance of RKE with the outstanding predictive value of ERKE. This condition is, at least partially, a resultant of smaller mesocyclone radii in the most intense storms. The mean radius of all observations in the two violently tornadic storms is 2 km, but in the storms with strong tornadoes it is 3 km, and in those without tornadoes or only weak tornadoes it is 3.3 km. The large radii contribute directly to higher RKE, but also reduce the role of velocity in its contribution to ERKE. It is fortunate, indeed, that ERKE reflects a mesocyc-

TABLE 2. Comparison of predictors for non-violent tornadoes

Predictor	$t_{mv}$	Storm errors	Performance for 11 strong (F2 and F3) tornadoes		
			Number of tornadoes missed	Number of negative lead times	Mean lead time
ERKE ( $S_m = 6$ , $h = 4$ )	3.02	1 M	0	1	27 objective (29) (adjusted)
Velocity (P) ( $h = 7$ )	3.35	3 FA	0	1	27 (28)
RP ( $h = 4$ )	3.20	2 FA	0	5	20 (23)
ERP ( $S_m = 6$ , $h = 7$ )	1.50	3 M 1 FA	2	1	12 (19)
Time-Integrated (RP, $h = 4$ )	2.36	1 M 1 FA	0	6	-3 (4)
Shear (P) ( $h = 4$ )	1.47	3 M	2	4	-10 (6)
RKE ( $h = 4$ )	1.81	4 M 2 FA	8	2	40 (24)

clone characteristic that anticipates the tornado process so reliably in these early results.

### 5. Concluding remarks

Significant improvements in tornado-warning capability have been demonstrated by Doppler-radar measurement of particular mesocyclone features in 17 mesocyclonic storms observed in Oklahoma. ERKE predicted both of the two violent F4 tornadoes in our sample, with adequate lead times and no false alarms. Nearly perfect detection, also with adequate lead times, was provided for the strong F2 and F3 tornadoes by ERKE and by rotational velocity. Little or no skill was achieved for identification of the so-called weak (F0 and F1) tornadoes.

Although our sample of storms is very small, the successful predictors (ERKE and velocity) seem to be statistically significant at or above a 99% level of confidence, and offer reasonable promise that these predictors will be useful as an aid for warning of strong and violent tornadoes in the large number of storms that will be available for study after installation of the NEXRAD radar network. These early results offer a promising basis for the eventual development of an automated technique for tornado warning. However, the detailed treatment of the predictors may very likely differ, especially regionally, from the particular forms found to be most productive for this small sample of Oklahoma storms.

**Acknowledgments.** We are pleased to express our gratitude to Don Burgess and Doug Forsyth of the National Severe Storms Laboratory—fellow workers in developing Doppler radar techniques for detection of tornadoes and severe storms—for providing radar data on several Oklahoma mesocyclones. We are very appreciative of the efforts of our local friends Donna Velardi, for her patience and skill in preparation of our manuscript, and Ian Harris, for his helpful encouragement and suggestions. We are also grateful for valuable suggestions offered by Don Burgess, by an anonymous reviewer, and by Louis Uccellini, co-editor of this journal. This work was supported under AFGL Contract F19628-87-C-0124.

### APPENDIX

#### Assessment of the Significance of Mean Differences of Predictor Values

The significance of mean differences in tornado predictor values was tested by calculating the small-sample variances,  $\sigma^2$ , larger than the normal population variance by a factor  $N/(N-1)$ , where  $N$  is the sample size. We use the symbol  $\sigma^2$  for small-sample variance,  $m$  for mean, and subscripts  $T$ ,  $v$ ,  $nv$ , and  $0$  to designate attributes of all 17 mesocyclones, the two with violent (F4) tornadoes, the six with nonviolent (F0 to F3) tornadoes, and the nine without tornadoes, respectively.

The statistic  $t_{nv}$ , based on the Student's  $t$  distribution, for assessing the significance of the difference in means of a predictor value for mesocyclones with nonviolent tornadoes ( $m_{nv}$ ) and mesocyclones without tornadoes ( $m_0$ ) is given by a standard formula:

$$t_{nv} = (m_{nv} - m_0)(\sigma_{nv}^2/N_{nv} + \sigma_0^2/N_0)^{-1/2}. \quad (A1)$$

This gives credible results if we had been certain that the two distributions are representative of the same population. There is no way of knowing to what extent or in which direction our very small sample is biased. Therefore, very conservatively, we use equal values of variance, which we call  $\hat{\sigma}^2$ , given by the larger of the variances  $\sigma_{nv}^2$  and  $\sigma_0^2$  in (A1). Then, since  $N_{nv} = 6$  and  $N_0 = 9$ , we can simplify (A1) to

$$t_{nv} = 1.9(m_{nv} - m_0)/\hat{\sigma}. \quad (A2)$$

We find, in the Student's table of  $t$  values, under  $N_{nv} + N_0 - 2 = 13$  degrees of freedom, that  $t = 3.01$  indicates a probability of 0.01 that our sample-mean difference occurred by chance. Accordingly, we welcome  $t_{nv}$  values in excess of 3 as significant at the 99% level of confidence.

In order to test the significance of mean differences in predictor values for the two mesocyclones with violent tornadoes ( $m_v$ ) and all others, we considered that a sample size of 2 is much too small for meaningful treatment by (A1). Instead, we chose a formula that tests the significance of a deviation of a subset mean from the total mean that incorporates the subset. Using subscript  $v$  for our subset and  $T$  for the total distribution, this formula is expressed as

$$t_v = (m_v - m_T)\sigma_T^{-1}N_v^{1/2}(1 - N_v/N_T)^{-1/2}. \quad (A3)$$

With  $N_v = 2$  and  $N_T = 17$ , (A3) simplifies to

$$t_v = 1.5(m_v - m_T)/\sigma_T. \quad (A4)$$

For  $N_T - 2 = 15$  degrees of freedom, the probability of 0.01 for a chance difference of  $m_v$  from  $m_T$  occurs with  $t_v = 2.95$ .

### REFERENCES

- Brooks, E. M. 1949. The tornado cyclone. *Weatherwise* 2: 32-33.
- Brown, R. A., and L. R. Lemon. 1976. Single Doppler radar vortex recognition: Part 2, Tornadic vortex signatures. Preprints, 17th Conference on Radar Meteorology, Seattle, pp. 104-109. Boston: American Meteorological Society.
- , —, and D. W. Burgess. 1978. Tornado detection by pulsed Doppler radar. *Mon. Wea. Rev.* 106: 29-38.
- Burgess, D. W. 1976. Single Doppler radar vortex recognition: Part 1, Mesocyclone signatures. Preprints, 17th Conference on Radar Meteorology, Seattle, pp. 97-103. Boston: American Meteorological Society.
- , and L. R. Lemon. 1990. Severe thunderstorm detection by radar. *Radar in Meteorology*, ed. D. Atlas, American Meteorological Society.
- , V. T. Wood and R. A. Brown. 1982. Mesocyclone evolution statistics. Preprints, 12th Conference on Severe Local Storms, San Antonio, pp. 422-424. Boston: American Meteorological Society.



- Desrochers, P. R., R. J. Donaldson, Jr. and D. W. Burgess. 1986. Mesocyclone rotational kinetic energy as a discriminator for tornadic and non-tornadic types. Preprints, *23rd Conference on Radar Meteorology*, Snowmass. pp. 1-4. Boston: American Meteorological Society.
- Donaldson, R. J., Jr. 1970. Vortex signature recognition by a Doppler radar. *J. Appl. Meteor.* 9: 661-670.
- , and P. R. Desrochers. 1985. Doppler radar estimates of the rotational kinetic energy of mesocyclones. Preprints, *14th Conference on Severe Local Storms*, Indianapolis. pp. 52-55. Boston: American Meteorological Society.
- Fujita, T. 1958. Mesoanalysis of the Illinois tornadoes of 9 April 1953. *J. Meteor.* 15: 288-296.
- . 1971. Proposed characterization of tornadoes and hurricanes by area and intensity. SMRP Research Paper, Number 19, Univ. Chicago, 42 pp.
- . 1981. Tornadoes and downbursts in the context of generalized planetary scales. *J. Atmos. Sci.* 38: 1511-1534.
- Hennington, L. D., D. S. Zrnic and D. W. Burgess. 1982. Doppler spectra of a maxi-tornado. Preprints, *12th Conference on Severe Local Storms*, San Antonio. pp. 433-436. Boston: American Meteorological Society.
- JDOP Staff. 1979. Final Report on the Joint Doppler Operational Project (JDOP) 1976-1978. NOAA Tech. Memo. ERL NSSL-86. National Oceanic and Atmospheric Administration, U.S. Department of Commerce, Washington, DC. [NTIS PB80-107188/AS].
- Kelly, D. L., J. T. Schaefer, R. P. McNulty and C. A. Doswell III. 1978. An augmented tornado climatology. *Mon. Wea. Rev.* 106: 1172-1183.
- Lemon, L. R., D. W. Burgess and L. D. Hennington. 1982. A tornado extending to extreme heights as revealed by Doppler radar. Preprints, *12th Conference on Severe Local Storms*, San Antonio. pp. 430-432. Boston: American Meteorological Society.
- Lhermitte, R. M. 1964. Doppler radars as severe storm sensors. *Bull. Amer. Meteor. Soc.* 45: 587-596.
- Pearson, A. D., and C. L. David. 1979. Tornado and severe thunderstorm warning verification. Preprints, *11th Conference on Severe Local Storms*, Kansas City. pp. 567-568. Boston: American Meteorological Society.
- U.S. Standard Atmosphere Supplement. 1966. U.S. Government Printing Office, D.C.
- Wood, V. T., E. A. Brandes and R. A. Brown. 1986. Computation of vorticity and vertical velocity from single Doppler radar measurements in severe thunderstorms. Preprints, *23rd Conference on Radar Meteorology*, Snowmass. pp. JP115-JP118. Boston: American Meteorological Society.

COMPARISON OF ALGORITHMIC AND MANUAL PERFORMANCE OF TORNADO  
PREDICTORS DERIVED FROM DOPPLER DATA

Ralph J. Donaldson, Jr. and  
ST Systems Corporation  
Lexington, MA

Paul R. Desrochers  
Geophysics Laboratory  
Hanscom AFB, MA

1. INTRODUCTION

Doppler radar, with its capability to measure advancing and receding air motion, provides a valuable source of information on processes within convective storms. Mesocyclones, a characteristic feature of many severe thunderstorms, are readily detected by Doppler radar, and their detection is an important aid in tornado prediction. The early investigations of Oklahoma thunderstorms by Burgess (1976) indicated that roughly half of the storms containing mesocyclones produce tornadoes. This occurrence ratio was confirmed later during the Joint Doppler Operational Project (JDOP Staff, 1979), where the tornadic storms provided a mean lead time of about 20 minutes from confirmation of a mesocyclone by Doppler radar to tornado touchdown.

Donaldson and Desrochers (1985) sought further improvement in tornado prediction by Doppler radar through their proposal of the concept of excess rotational kinetic energy (ERKE) of mesocyclone cores. ERKE is rotational kinetic energy calculated after subtraction of the product of core radius and a selected value of shear from mesocyclone rotational velocity. The resultant diminished velocity can be regarded as excess to the minimum requirement for maintenance of the mesocyclone. Desrochers et al. (1986) used ERKE to correctly identify tornado occurrence in 9 of 10 mesocyclonic storms. Recently Donaldson and Desrochers (1990) examined 17 Oklahoma storms containing mesocyclones; 8 of these produced tornadoes, 9 did not. They investigated ERKE and several other candidate predictors of tornadoes, and found that ERKE performed best, correctly identifying 16 of the 17 storms, with a median lead time of 18 minutes to the first strong tornado in a storm, and 28 minutes or more for the two violent tornadoes.

These results were obtained by manual inspection of the mesocyclone features. However, a real-time automated technique is required for practical forecasting purposes. Accordingly, Desrochers (1990) has developed an improved mesocyclone detection algorithm. This algorithm provides the information on mesocyclone parameters to a tornado probability algorithm. It is the purpose of this paper to evaluate the automated technique and compare its results to the older manual inspection method.

2. THE MESOCYCLONE ALGORITHM

Doppler radar can detect only the component of motion directed along its beam. Maximum velocities of rotational features, like mesocyclones, are therefore sensed at only two points by a single Doppler radar, and the shear associated with rotation is oriented in the azimuthal direction. Mesocyclone algorithms essentially detect and interpret azimuthal shear.

Vectors of azimuthal shear are detected by the algorithm, assimilated into two-dimensional features, and then associated with features from other elevations. The resulting three-dimensional feature is evaluated for classification as a mesocyclone. Rules for mesocyclone classification were proposed by Donaldson (1970) and verified by Burgess (1976) and the JDOP Staff (1979). Their important characteristics are:

- \* Azimuthal shear of at least 0.005/s between the peak relative incoming and outgoing velocities.
- \* The mesocyclone shear pattern, known as a velocity couplet, extends vertically at least 3 km.
- \* The feature persists for a time equal to at least half its rotation period.

In addition to the JDOP rules, the algorithm has a simple shape criterion for identifying couplets.

An important feature of the current algorithm is the ability to accurately determine mesocyclone parameters such as size and rotational velocity. Estimates of velocity, for example, are derived from an average of selected values that is weighted toward the largest values. A weighting function given by

$$V = V_{\text{thresh}} - |V_a - V_{\text{max}}| \quad (1)$$

is applied uniquely to each velocity that is contained in the average.  $V_{\text{max}}$  is the maximum observed incoming or outgoing velocity for a feature.  $V_{\text{thresh}}$  is a velocity threshold that varies between 5 and 25 m/s. Qualifying velocities ( $V_a$ ) for inclusion in the average are those values that are within  $V_{\text{thresh}}$  of  $V_{\text{max}}$ .  $V_{\text{thresh}}$  is selected such that at least 10 values

are included for averaging. This minimizes the impact of erroneous values that may occur, for example, during de-aliasing. The peak velocity ( $V$ ) is then given by

$$V = \sum (W \cdot V_q) / \sum (W) \quad (2)$$

This process is performed separately for the incoming and outgoing velocities. Weighting in this manner essentially provides a numerical approach to contouring. Azimuth and range are obtained in a similar manner, based also on the peak velocities. For a more detailed discussion of the algorithm the reader is referred to Desrochers (1990).

### 3. TORNADO PREDICTORS

Four mesocyclone features (velocity, shear, ERKE, and RP) were selected as candidate tornado predictors. Velocity ( $V$ ) is the maximum rotational speed of the mesocyclone core, and shear is defined as velocity divided by core radius,  $r$ . The formulation for ERKE, which we introduced in 1985, is

$$ERKE = \rho \Delta h \pi r^2 (V - r S_c)^2 / 4, \quad (3)$$

where  $\rho$  is air density,  $\Delta h$  is an increment of mesocyclone height, and  $S_c$  is a selected threshold value of mesocyclonic shear. The predictor RP is the product of shear ( $V/r$ ) and rotational kinetic energy, defined as

$$RP = \rho \Delta h \pi r V^3 / 4. \quad (4)$$

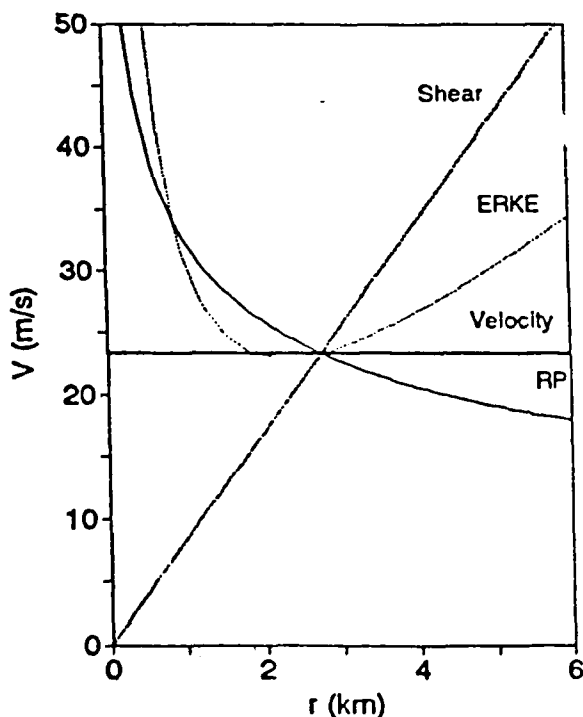


Figure 1. Candidate tornado predictors portrayed on the plane of mesocyclone core radius and velocity, using mean values of the mature mesocyclone of Burgess et al. (1982).

These four candidate predictors are portrayed on Fig. 1, using values of velocity (23.3 m/s) and radius (2.75 km) found by Burgess et al. (1982) for a typical mesocyclone core in its strongest stage of development. The direction of greater predictor value for each curve is towards the top of the page. These curves define the value of 1 CHM (climatological mature mesocyclone), and all values of ERKE and RP observed in a storm are expressed as a fraction or a multiple of 1 CHM.

There were 13 storms, 6 of them tornadic, suitable for analysis by algorithm. All storms were observed in Oklahoma during 1977, 1978, and 1981 by one or the other of the two NSSL 10-cm Doppler radars. At each observational time, the new and improved mesocyclone algorithm calculated the four predictors and found average values of each one from ground level up to heights  $h = 4, 5, 6,$  and  $7$  km above ground. In addition, for the ERKE formulation, two values were selected for  $S_c$ :  $0.005/s$  and  $0.006/s$ . Thus a total of 20 time series of candidate predictors was produced for each of the 13 storms.

Previous experience by Desrochers et al. (1986) had demonstrated the usefulness of persistence of the predictor values as assurance against acceptance of large spurious errors that almost always affect just one observational time. Accordingly, persistent values of each of the 20 sets of predictors were calculated for periods of 5 and 10 minutes, by selecting the minimum instantaneous value occurring during the 5-minute or 10-minute period preceding each observation, interpolating where necessary. This exercise left us with 40 time series for 13 storms. Obviously some winnowing was the next order of business.

### 4. SELECTION OF OPTIMUM PREDICTOR PARAMETERS

The optimum mix of parameters, comprising averaging height, duration of required persistence, and threshold mesocyclonic shear for ERKE, was determined by t-statistics, which provided a measure of the significance of mean differences of the distributions. Two sets of parameters were selected for each predictor. One set was calculated as most significant for discriminating strong and violent tornadic storms (designated intensity F2+ on the scale established by Fujita, 1981) from storms of lesser intensity. In this data set there were no tornadic storms containing only weak tornadoes of intensity F0 and F1, so all storms of lesser intensity than F2 in our group were non-tornadic. The other set of parameters for each predictor was chosen to best isolate the two storms with violent F4 tornadoes from all the other storms.

For each of the 40 sets of parameters, the statistical procedure required calculation of means  $\bar{m}$  and small-sample standard deviations  $\sigma$  for maximum predictor values of the six tornadic storms, the seven non-tornadic storms, and all 13 storms, designating these by subscripts F2+, 0, and T (total), respectively. Also calculated was  $\bar{m}_{F2+}$ , the mean of the maximum predictor values for the two storms with violent tornadoes.

The statistic  $t_{F2+}$ , based on the student's t distribution, to determine the best parameter set for predicting all F2+ tornadoes, is given by a standard formula:

Table 1: Optimum Parameter Mix and t-Statistic for Prediction of F2+ and F4 Tornadoes

Predictor	ERKE	Velocity	Shear	RP
Parameters for F2+ tornadoes	S = 0.005/s h = 5 km 5-min persistence	h = 5 km 5-min persistence	h = 7 km 10-min persistence	h = 6 km 10-min persistence
$t_{r2+}$	4.00	3.39	2.59	2.56
Parameters for F4 tornadoes	S = 0.006/s h = 4 km 5-min persistence	h = 5 km 10-min persistence	h = 6 km 5-min persistence	h = 5 km 5-min persistence
$t_{r4}$	2.90	2.87	3.28	2.30

$$t_{r2+} = (m_{r2+} - m_0)(\sigma_{r2+}^2/N_{r2+} + \sigma_0^2/N_0)^{-0.5}, \quad (5)$$

where N is the number of storms in each distribution. With  $N_{r2+} + N_0 - 2 = 11$  degrees of freedom, values of  $t_{r2+} \geq 3.11$  indicate a probability of <0.01 that the sample mean difference is a chance occurrence.

The significance  $t_{r4}$  of mean differences in maximum predictor values for the two storms with violent tornadoes ( $m_{r4}$ ) and the others was evaluated by a formula that tests the significance of a deviation of a subset mean from the total mean that incorporates the subset:

$$t_{r4} = (m_{r4} - m_T)\sigma_T^{-1} N_T^{0.5} (1 - N_{r4}/N_T)^{-0.5}, \quad (6)$$

which simplifies to  $t_{r4} = 1.54(m_{r4} - m_T)/\sigma_T$  for  $N_{r4} = 2$  and  $N_T = 13$ .

The results of these statistical analyses are given in Table 1. The table suggests that ERKE is a stellar performer for identifying F2+ tornadoes, and shear looks like the best bet for picking out storms with F4 tornadoes. This process has reduced our number of predictor sets from 40 to 8. Further reductions should be possible by examining the detailed tornado forecasting results of these statistical survivors.

## 5. TORNADO PREDICTOR PERFORMANCE

Statistical analysis has narrowed the field of candidate predictors, but the acid test is performance in providing acceptable lead times for tornado warnings with the minimum number of false alarms and failures to detect tornadoes. The performance of the leading predictors for our data set is illustrated clearly on Fig. 2 for F2+ tornadoes, and on Fig. 3 for F4 tornadoes. These figures show how performance varies as a function of the increase of predictor values during the development of a mesocyclonic storm.

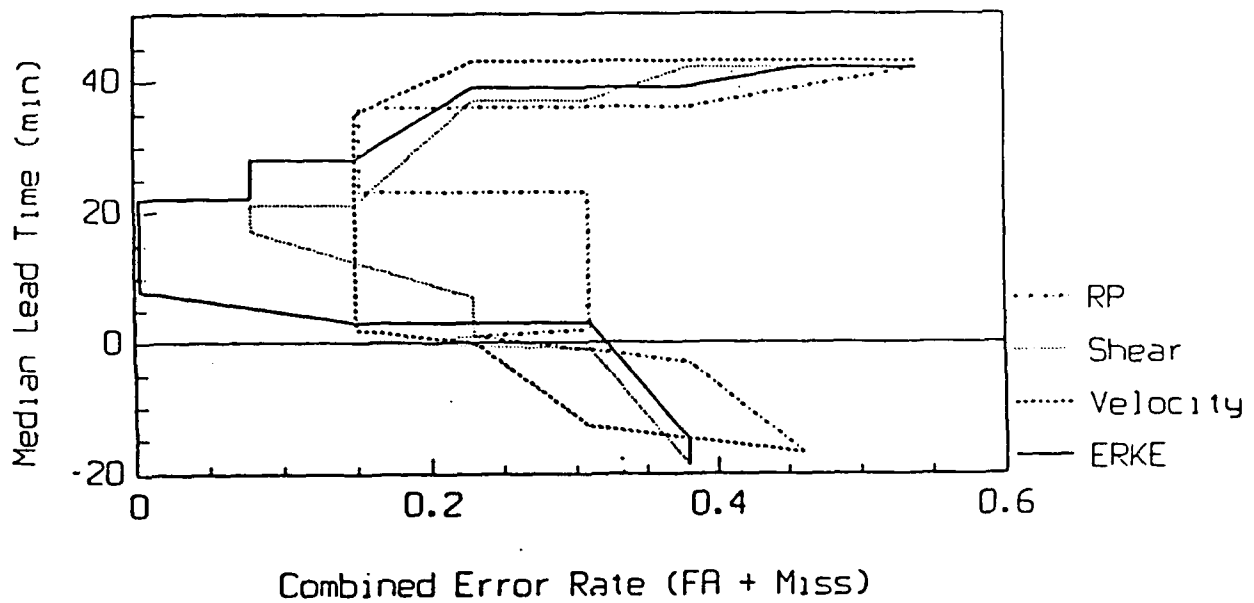
The ordinate of each figure is the lead time from completion of the measurement of a predictor value to the time of touchdown of the first tornado of a given intensity in a storm. On Fig. 2 the performance curves show the median

lead time for the 6 tornadic storms, rather than mean which is biased on the high side by extraordinarily long lead times in one storm. On Fig. 3 the lead time is the lesser time achieved by the two storms with violent F4 tornadoes, and thus is a conservative estimate of what can be achieved. The linear ascending scale of lead times on each diagram is related implicitly to descending, non-linear progressions of predictor values for the four predictors in each tornado intensity category that survived the statistical analysis. Thus maximum lead times are associated with minimum predictor values, and vice versa.

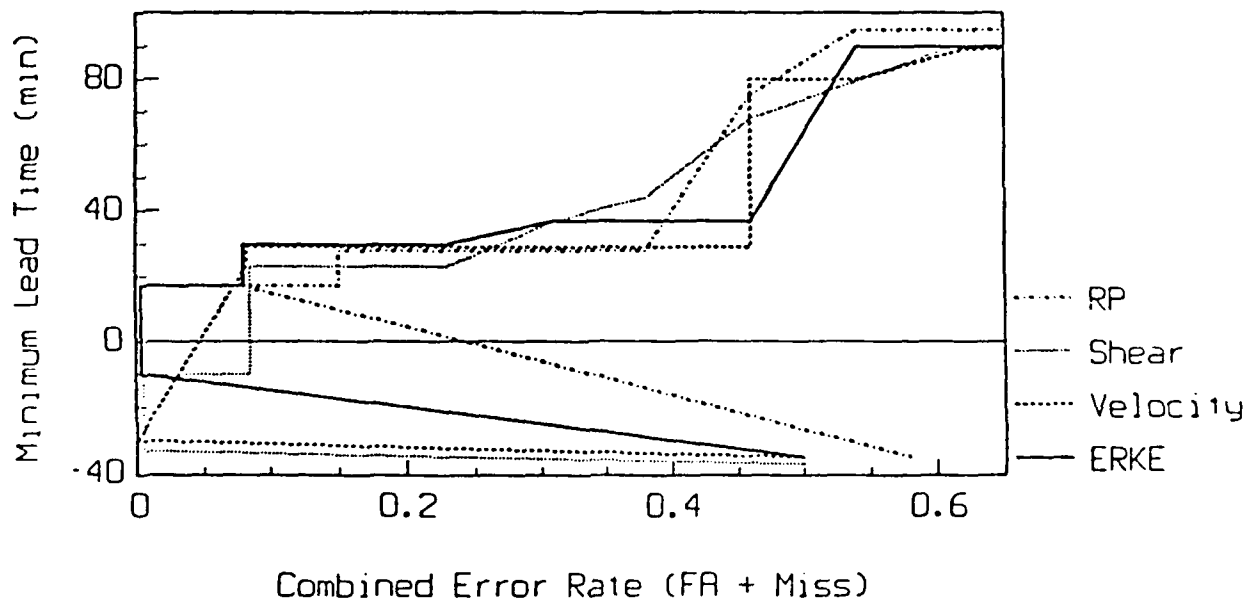
The abscissa on each diagram is a combined error rate owing to false alarms and failures to detect. The false-alarm rate, for a given class of tornado intensity and lead time, equals the number of storms incorrectly identified as an eventual producer of one or more tornadoes of the same or greater intensity, divided by the total number of storms, 13 in this sample. The rate of failures of detection is the number of tornadoes not detected in a given intensity class and at a particular lead time, divided by the total number of tornadoes in the class. There were 13 F2+ tornadoes, including 2 F4 tornadoes, in the 6 tornadic storms. The two kinds of errors are easily distinguished on these diagrams, because false alarms decrease with decreasing lead times, as predictor values increase, but failures of detection eventually increase as lead times decrease.

All of the curves in Figs. 2 and 3 demonstrate appreciable forecasting skill above and beyond the early findings of Burgess (1976) and JDOP (1979) that approximately half of detected mesocyclones will produce a tornado. However, ERKE is clearly the best predictor for both intensity classes of tornadoes in the critical region where false alarm rates are less than 20% and no failures of detection are tolerated. Shear showed great promise in the statistical analysis for identifying F4 tornadoes, but it tends to peak late in a storm's lifetime and therefore had negative lead times for zero false alarms.

### F2+ TORNADO PREDICTION



### F4 TORNADO PREDICTION



Figures 2 & 3. Tornado prediction performance of the four candidate algorithmic predictors for strong and violent tornadoes of intensity F2 or greater (Figure 2, above) and for only the violent F4 tornadoes (Figure 3, below). Please refer to accompanying text for a full explanation of results.

Negative lead times are indicated clearly on Fig. 3, because the minimum lead time for the F4 tornadoes was selected for portrayal there, in the interest of eschewing oversell. However, negative lead times are not at all obvious on Fig. 2, so they will be reported now: Each of the four predictors suffered one negative lead time out of 13 F2+ tornadoes as the number of false alarms decreased from 6 to 5. With the increase of predictor values, false alarms decrease but negative lead times increase. Two negative lead times first appeared when shear reached three false alarms, and when velocity and RP reached two false alarms. The best performer was ERKE, which had two negative lead times with just one false alarm. Counting negative lead times as an error, the minimum number of errors achieved by ERKE in predicting F2+ tornadoes was two, in contrast to a minimum of four errors by the other three predictors.

#### 6. COMPARISON OF ALGORITHMIC AND MANUAL ANALYSIS

The 13 storms were examined manually to determine mesocyclone core features that could be used for calculation of height-averaged and persistent values of the four predictors: ERKE, velocity, shear, and RP. Only the eight winning combinations of parameter values found previously for the algorithmic analysis and listed in Table 1 were calculated. A tornado prediction performance analysis was conducted for these so-called manual predictors and compared with the corresponding findings of the algorithmic predictors as reported in Section 5.

The distributions of the values of the manual predictors followed the same trend as the corresponding algorithmically-generated distributions, but with higher values. The algorithm averaging process described earlier produced lower mesocyclone velocities but somewhat larger core radii than those read manually. Accordingly, differences were greater for shear ( $V/r$ ) than for velocity, and were least for ERKE, which involves the product of velocity and radius.

The median lead times for the two analysis modes are compared alongside one another in Table 2, with the algorithm lead times enclosed in parentheses. These are listed for both F2+ and F4 tornado predictors at the operationally significant false alarms of 3, 2, 1, and 0 out of 13 storms. It is easy to see that the algorithmically-generated ERKE predictor is superior for both tornado intensity classes, especially at the level of zero or one false alarm.

Some of the differences in lead time are enormous between the manual and algorithmic techniques for mesocyclone analysis. For example, note the astounding difference for prediction of F4 tornadoes by ERKE at the level of zero false alarms. We cannot explain this, but we suspect that our very small sample size could allow some surprises. Nevertheless, we feel confident that the mesocyclone algorithm as developed by Desrochers (1990) provides reliable data leading to superior tornado prediction performance.

#### 7. CONCLUDING REMARKS

A small sample of 13 mesocyclonic storms in Oklahoma furnished data for an investigation of the possibility of generating reliable tornado warnings by automated Doppler radar techniques. The results showed that a new algorithm for mesocyclone detection developed by Desrochers (1990) provided greater lead times than manual analysis for prediction of strong and violent tornadoes of intensity F2 and greater. The predictor that provided the longest warnings with fewest false alarms and negative lead times is excess rotational kinetic energy (ERKE). Although this sample is minuscule, a statistical analysis indicated that the difference in means of ERKE measured in the tornadic and non-tornadic storms was significant at a level of confidence well in excess of 99%. It is therefore reasonable to expect good performance by NEXRAD radars in predicting strong and violent tornadoes associated with mesocyclones.

Table 2: Median Lead Times in Minutes for Manual and (Algorithmic) Tornado Predictors

Predictor of F2+ Tornadoes:	False Alarm Ratio			
	3/13	2/13	1/13	0
ERKE	28 (39)	28 (28)	28 (28)	16 (22)
Velocity	28 (42)	21 (35)	10 (1)	3 (-42)
Shear	25 (36)	16 (21)	16 (21)	-13 (0)
RP	25 (36)	25 (36)	21 (1)	9 (-57)
Predictor of F4 Tornadoes:				
ERKE	58 (66)	22 (66)	-7 (62)	-27 (55)
Velocity	73 (42)	73 (42)	25 (42)	-17 (-6)
Shear	18 (38)	18 (38)	13 (38)	-17 (-5)
RP	68 (88)	58 (88)	-7 (41)	-7 (-22)

## 8. ACKNOWLEDGMENTS

We are happy to acknowledge the valuable contributions of our colleagues: Ian Harris for his helpful critique and for producing the diagrams, and Donna Velardi for her expertise in preparing and assembling our manuscript. We are also thankful to Don Burgess and Doug Forsyth of NSSL for providing data on several Oklahoma mesocyclones. Most of this work was supported under GL Contract F19628-87-C-0124.

## 9. REFERENCES

- Burgess, D. V., 1976: Single Doppler radar vortex recognition: Part I, Mesocyclone signatures. Preprints, 17th Conf. on Radar Meteorology (Seattle), AMS, Boston, 97-103.
- Burgess, D. V., V. T. Wood, and R. A. Brown, 1982: Mesocyclone evolution statistics. Preprints, 12th Conf. on Severe Local Storms (San Antonio), AMS, Boston, 422-424.
- Desrochers, P. R., 1990: Automatic Mesocyclone Detection and Tornado Forecasting. ST Systems Corp. Technical Report published under contract with Geophysics Laboratory (in press).
- Desrochers, P. R., R. J. Donaldson, Jr., and D. V. Burgess, 1986: Mesocyclone rotational kinetic energy as a discriminator for tornadic and non-tornadic types. Preprints, 23rd Conf. on Radar Meteorology (Snowmass), AMS, Boston, 1-4.
- Donaldson, R. J., Jr., 1970: Vortex signature recognition by a Doppler radar. J. Appl. Meteor., 9, 661-670.
- Donaldson, R. J., Jr. and P. R. Desrochers, 1985: Doppler radar estimates of the rotational kinetic energy of mesocyclones. Preprints, 14th Conf. on Severe Local Storms (Indianapolis), AMS, Boston, 52-55.
- Donaldson, R. J., Jr. and P. R. Desrochers, 1990: Improvement of tornado warnings by Doppler radar measurement of mesocyclone rotational kinetic energy. Weather and Forecasting, 5, xxx-xxx.
- Fujita, T., 1981: Tornadoes and downbursts in the context of generalized planetary scales. J. Atmos. Sci., 38, 1511-1534.
- JDOP Staff, 1979: Final Report on the Joint Doppler Operational Project (JDOP) 1976-1978. NOAA Tech. Memo. ERL NSSL-86, 84 pp.

**B-3: Paper on Hail Size Estimation**

**Desrochers, P.R., 1990: Some aspects of the mesocyclone related to hail formation. Preprints, 16th Conf. on Severe Local Storms. (In Press).**



## SOME ASPECTS OF THE MESOCYCLONE RELATED TO HAIL FORMATION

Paul R. Desrochers

Geophysics Laboratory  
Hanscom AFB, MA

### 1. INTRODUCTION

The updraft is an important element in convective storms controlling the production of large hail. Updraft speed (Browning, 1963), areal extent (Nelson, 1983, Ziegler et al., 1983), and horizontal airflow relative to the updraft (Browning and Foote, 1976) are seen to be important characteristics contributing to the growth of large hail. Therefore, it would appear that if hail events are to be predicted, an accurate description of the updraft region within a storm is necessary.

The purpose of this paper is to identify aspects of the updraft that are useful for predicting hail events. Because this work is oriented for real-time operations we examine techniques applicable to analysis by single-Doppler radar. Specifically, we examine characteristics of the mesocyclone, a manifestation of the updraft that is readily detected by single-Doppler radar.

It is apparent that accurate prediction of hail events will require consideration of many aspects of storm structure including microphysics and kinematics. However, it is believed that kinematics play a dominant role in the growth of large hail (Knight and Knight, 1973) and kinematic evaluation techniques, such as those to be presented here, will add to the capability of existing techniques that evaluate hail likelihood through interpreting a storm's reflectivity structure (e.g., Lemon, 1978).

### 2. MESOCYCLONE CHARACTERISTICS

The mesocyclone offers a unique view of the updraft from which a host of characteristics can be derived. In this paper we examine three aspects of the mesocyclone/updraft that are considered to be physically related to hail growth: upper-level outflow, divergence structure, and rotation.

#### 2.1 Upper-Level Outflow

A promising technique for the prediction and sizing of large hail using a single Doppler radar was developed by Vitt and Nelson (1984). They examine two aspects of the mesocyclone outflow that are related to updraft speed. These are the velocity difference ( $\Delta V$ ) of the divergent flow at 10 km and the divergence at 10 km multiplied by its areal extent, a term they call High Radial Shear Area (HRSa). Among the 6 storms of their study they find a nearly perfect correlation

between outflow strength and maximum hail size.

The storms of their study were sampled by multiple Doppler radars. Mesocyclone outflows are often asymmetric, and multiple perspectives are needed for accurate outflow estimates. Accordingly, Vitt and Nelson report that the correlation of hail size with outflow strength decreases somewhat for single-Doppler determinations. They point out, however, that even with outflow asymmetries it is still possible to distinguish 2-4 cm hailers from 7-10 cm ones with a single Doppler radar. We test their findings further on a larger and more diversified data set.

#### 2.2 Divergence Structure

The dominant mechanism for hail growth is considered to be the accretion of supercooled cloud droplets (e.g., Rogers, 1979). A desirable trajectory for growth is one that keeps hail embryos and hailstones in the updraft for a long period of time. Hail embryos that ascend in the center of a strong updraft will likely be lost to the anvil.

Standard mesocyclone structure consists of rotation and convergence at lower tropospheric levels, changing to pure rotation in mid-levels, changing again to divergence and rotation aloft, and perhaps capped by pure divergence (Burgess et al., 1982). This general structure contains elements favorable to hail growth. For example, convergence at low levels can serve to gradually introduce hail embryos to greater updraft speeds. Rotation at middle tropospheric levels may serve to maintain growing hailstones within the updraft where they can enjoy maximum growth.

In an updraft, continuity requires adherence to this standard mesocyclone structure; but one can speculate that the heights where convergence/divergence becomes significant may vary from storm to storm. We will examine the divergence structure and evaluate the impact on hail growth.

#### 2.3 Rotation

Another aspect of the mesocyclone we could consider is rotation. Trajectory studies indicate that significant overall hail growth from mm to cm sizes occurs in the middle troposphere (e.g., Foote et al., 1982; Miller et al., 1988). Since mesocyclones typically display rotation at middle levels (Burgess et al., 1982) it would be interesting to see if rotation differs among hailers and non-hailers.

Table 1. Data Set of Mesocyclones

Oklahoma mesocyclone	date	maximum hail size
Ada	4/29/78	10.0 cm
Ardmore	5/13/83	7.0
Binger	5/22/81	6.5
Clinton	5/22/81	5.0
Fort Cobb	5/20/77	5.0
Enid	5/26/87	4.5
Kingfisher	5/13/83	3.5
Healdton	6/13/87	2.5
Sterling	5/20/77	2.5
Cordell	5/22/81	0
Del City	5/20/77	0
Foster	5/19/77	0
Konawa	4/29/78	0
Maysville	6/15/87	0
Pauls Valley	6/15/87	0
Sylvian	4/29/78	0
Vanoss	4/29/78	0

### 3. TEST CASES

This work is supported by a data base that contains a broad range of hail sizes. The data set contains 17 Oklahoma mesocyclones (Table 1) collected with NSSL's Norman or Cimarron S-band Doppler radars. These data were analyzed manually using only single-Doppler data. The storms were selected on the basis of perceived hail reporting quality and radar observations to a height of at least 10 km. Maximum hail sizes range upwards to 10 cm. One useful aspect of the data set is the group of 8 storms that have no reported hail. They will help to define the mesocyclone characteristics unique to hailers.

The accuracy of hail size reports is an important consideration in studies like this one. The U.S. Department of Commerce publication Storm Data is a general source for hail reports, especially large hail. Another source is NSSL. These two sources do not always agree. Hail reports are sometimes incomplete and the accuracy of sizes is sometimes questionable. For example, in a ground survey NSSL found the maximum hail size in the Ada storm to be 10 cm (JDOP Staff, 1979), but Storm Data reports a maximum size of 2.5 inches (6 cm). When reports disagree we use the NSSL sizes.

All but one of the hail events, Clinton, are listed in Storm Data, and many of the events such as Ada, Binger, Fort Cobb, and Sterling are substantiated in literature or in the NSSL storm summaries provided by chase teams. A hail report of 5 cm stones for Clinton is found in the NSSL archives, but no time is listed for the hail event. Hail of baseball size is reported in Storm Data for the Ardmore storm and is interpreted to be 7-cm hail.

The greatest uncertainty in the data is with the storms that have no reports of hail. Hail events can go undetected in the sparsely populated areas that prevail in Oklahoma. However, Del City and Cordell, at least, were fairly well observed and had no reported hail.

NSSL's Volunteer Observer Network (VON), comprised of selected and trained observers, is considered to produce reliable reports of even small hail (Nelson and Young, 1979). Unfortunately, none of the supposed non-hailers occurred over the region west of NSSL covered by VON. The NOAA observer network, which covers the rest of Oklahoma, is not as dense as VON. It is

therefore quite possible that some storms without hail reports did produce hail.

The data used in this study cover the mesocyclone lifetimes in all but a few cases. In Foster and Ardmore our data begins after the mesocyclones have formed. Data collection in Foster began at the time of its first tornado. In Ardmore, our data begins after two hail events have occurred. Therefore, the earliest event we can predict is the third.

### 4. ANALYSIS TECHNIQUES AND RESULTS

In this section we examine the three mesocyclone characteristics described in Section 2. We follow the lead of Witt and Nelson (1984) in first examining upper level outflow. Then we will present formulations for rotation and divergence structure.

#### 4.1 Upper-Level Outflow

The component of  $\Delta V$  associated with divergence in a mesocyclone ( $\Delta V$ ) varies as a function of the velocity couplet orientation angle ( $\theta$ ) orthogonal to the radar beam as shown in Fig. 1.

$$\Delta V = (V_r - V_t) \sin(\theta) \quad (1)$$

where  $V_t$  and  $V_r$  represent relative flow away from and toward the radar, respectively. The standard convention is that flow away from the radar is positive. In situations of pure divergence  $\theta = 90^\circ$ . In solid body rotation  $\theta = 0^\circ$ .

Maximum values of  $\Delta V$  at 10 km for each storm, as examined by Witt and Nelson (1984), are shown in Fig. 2a. Among the hailers there appears to be a linear relationship between  $\Delta V$  and maximum hailstone size. The slope of  $\Delta V$

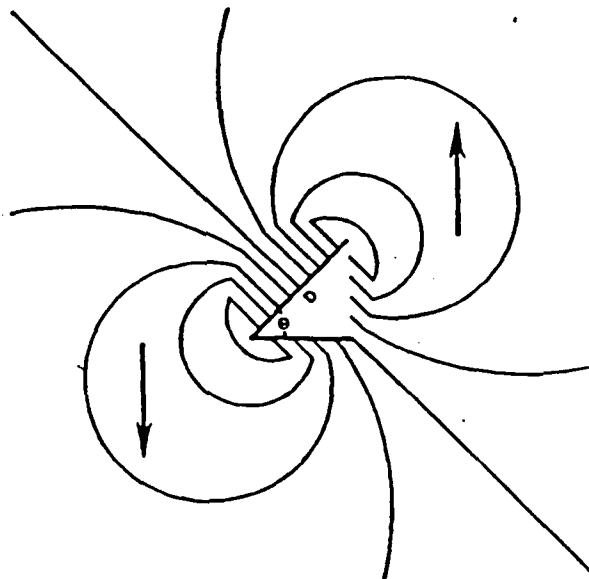


Figure 1) Single-Doppler velocity contours for an idealized mesocyclone displaying a combination of rotation and divergence. Mesocyclone core diameter ( $D$ ), measured between the endpoints of maximum velocity, and orientation angle ( $\theta$ ) are indicated. Arrows represent flow relative to the radar which is located in the direction towards the bottom of the page.

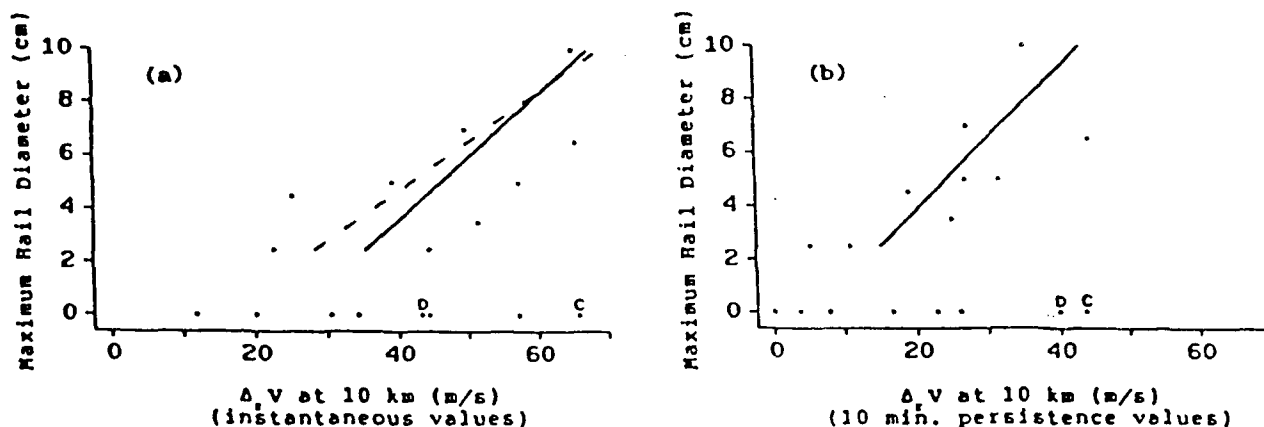


Figure 2). Plot of maximum hailstone diameter vs. maximum  $\Delta V$  at 10 km AGL for each storm listed in Table 1. D and C indicate the Del City and Cordell storms for which we are most confident that no large hail fell. a) instantaneous values of  $\Delta V$ . b) 10 min. persistence values of  $\Delta V$ .

obtained from a least squares fit of the hailers is shown by the solid line, which corresponds quite well with that of the Vitt and Nelson study shown by the dashed line.

There is a somewhat large deviation for each hail size category that averages 32% of the total  $\Delta V$  range of the hailers. As explained by Vitt and Nelson, some of this deviation can be attributed to asymmetries in the outflow.

A significant departure from  $\Delta V$  sizing is observed with the non-hailers. The Del City and Cordell storms, which we are most confident did not produce large hail, are indicated in the figure by C and D, respectively. These storms have outflow comparable even to the largest hailstone producers. This suggests that a strong outflow (indicative of a strong updraft) may be a necessary but not sufficient condition for hail formation.

Peaks in  $\Delta V$  tend to follow hail events by an average of 20 min. for the 5-cm and greater diameter hail. However, magnitudes of  $\Delta V$  prior to hailfall will determine its warning capability. Our evaluation approach is to adjust thresholds such that no severe hail events are missed. This is done at the expense of false alarms. We therefore use the False Alarm Rate to evaluate performance. The FAR is given by  $FAR = FA/(H+FA)$ , where FA (false alarms) are non-events that are improperly identified, and H (hits) are the number of successful discriminations for a sample. FAR varies between 0 and 1, with the former being the desired score.  $\Delta V$  produced a FAR of 0.58 when the threshold is adjusted to 34 m/s to achieve positive lead times for the 5-cm and greater hail events. An average lead time of 18 min. is achieved.

Somewhat improved results are attained when  $\Delta V$  is averaged with time. Values were calculated for persistence periods of 5, 10, 15, and 20 min. The method for determining persistence values is a conservative one; it is the minimum value occurring over a prescribed time period. For  $\Delta V$  the 10 min. persistence period is found to be most effective (Fig 2b). The 5-cm and greater storms are forecast with an average lead time of 16 min. with only two false alarms (FAR = 0.29). Averaging over time reduces the deviation in  $\Delta V$  for each hail size category for the hailers, but does not reduce the relative spread for the non-hailers.

As in Vitt and Nelson, we find  $\Delta V$  and the

High Radial Shear Area (HRSA) to be comparable hail indicators (not shown). Among the hailers, outflow strength is effective for distinguishing various sizes of large hail. However, the present findings also indicate that there is no significant difference in the outflow magnitude among hailers and non-hailers. Outflow magnitude appears not to be useful by itself.

#### 4.2 Rotational Kinetic Energy

A good quantifier of rotation is rotational kinetic energy (RKE). Donaldson and Desrochers (1990) developed a variation of RKE that is tailored for the magnitude of shear associated with mesocyclones. They call this parameter Excess Rotational Kinetic Energy (ERKE) and define it to be

$$ERKE = \rho \pi \Delta h r^2 (V - r S_m)^2 / 4 \quad (2)$$

where  $\rho$  is the air density,  $\Delta h$  an integration thickness,  $r$  the mesocyclone core radius,  $V$  the maximum tangential velocity, and  $S_m$  an arbitrary shear threshold (e.g., 0.005/s originally suggested by Donaldson (1970) for mesocyclone identification). When  $S_m$  is set equal to zero, ERKE becomes RKE.

Since hail growth trajectories have a vertical component we examine three-dimensional (3-D) ERKE, setting  $\Delta h$  to some thickness. ERKE is determined between elevations of 3 and 10 km for  $\Delta h$  of 4, 5, 6, and 7 km at all possible height combinations.  $S_m$  is varied between 0.005/s and 0/s to test the dependence of hail discrimination on rotational shear. The importance of persistence is also examined with instantaneous, 5, 10, 15, and 20 min. values determined.

For comparative purposes, 3-D ERKE is normalized with the ERKE of a typical mature mesocyclone. Climatological values of mesocyclone radius and tangential velocity at selected elevations and during the different stages of mesocyclone evolution are given in Burgess et al. (1982). The ERKE associated with a climatological mature mesocyclone is assigned the unit 1 CHM. Separate CHM values are calculated for each corresponding  $\Delta h$  and  $S_m$ .

The values at  $S_m$  of 0.005/s and 0/s are shown in Fig. 3. We first examine ERKE at the larger  $S_m$  (Fig. 3a). Shown are the maximum 10 min.

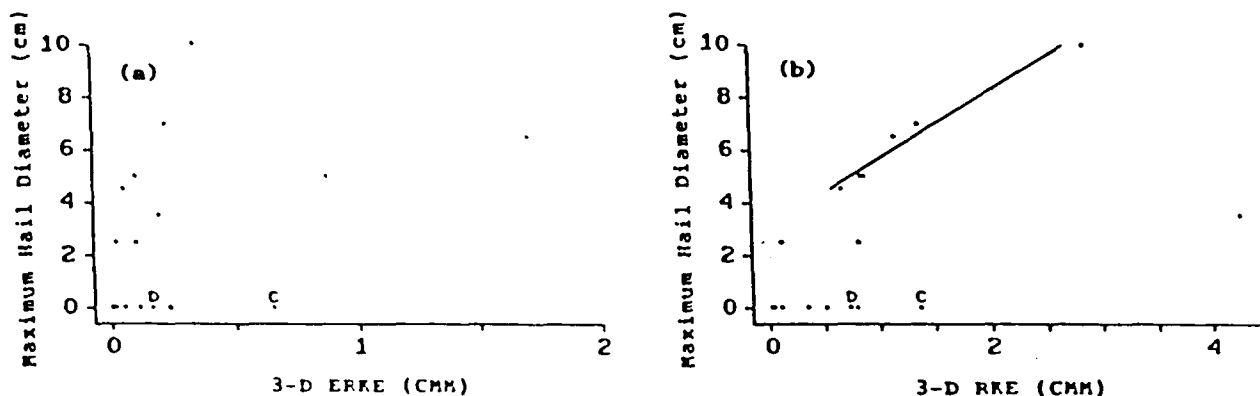


Figure 3). Same as in Fig. 2 but for three-dimensional ERKE. a) maximum 10 min. persistence values of 3-D ERKE from 5-10 km AGL at  $S_p=0.005/s$ . b) maximum 10 min. persistence values of 3-D RKE from 5-10 km AGL.

persistence values of ERKE integrated from 5 to 10 km. Although there is a general increase of ERKE from the smallest hail to the largest, the variation in ERKE magnitude for hailstones greater than 4 cm in diameter is considerable. This appears to make ERKE unsuitable as a size indicator. Donaldson and Desrochers (1990) find 3-D ERKE at the same shear threshold at low- to mid-tropospheric levels to be effective for identifying tornado potential. In contrast to what is found for tornado formation, the present results suggest that rotational shear is not important for hail growth.

Compared to ERKE, RKE displays a good deal of skill for hail sizing. Fig. 3b shows the maximum 10 min. persistence values of RKE integrated from 5 to 10 km, our best performer. For hail diameters of 4.5 cm or greater there is an excellent linear relationship between maximum hail size and RKE magnitude (correlation coefficient = 0.98). The deviation per hail size category is only 6% of the total RKE range of the hailers.

In four of the six storms producing 4.5-cm or larger diameter hail, RKE peaked prior to hailfall, suggesting that RKE is potentially useful for hail prediction. RKE, at a threshold of 0.4 CMM, predicts the 4.5-cm and greater hail events with an average lead time of 21 min. RKE, however, is subject to false alarms (FAR = 0.45).

Miller et al. (1988) examined hail trajectories of a supercell storm derived from multiple Doppler analysis. They found the mesocyclone to be important for the production of very large hail. Our results agree with their general findings. The strong correlation of RKE with hail size does indeed suggest a sizing mechanism. However, this relationship exists only for very large hail. As we also found with upper-level outflow (Section 4.1) the non-hailers must be identified before the sizing potential offered by RKE can be realized.

One caveat of these results is that they pertain only to the dominant mesocyclone cores. The data base for this study was compiled manually, concentrating, for the most part, on the primary mesocyclone cores. Many of the mesocyclones had multiple cores and so the total RKE of the updraft(s) is not accounted for here. The strong correlation of RKE with hail size for the 4.5-cm and greater hail does suggest, however, that a storm's largest hail is strongly

associated with the primary updraft.

Although for most of the hailers, the total updraft RKE is not included in our statistics, one interesting exception that deserves comment is the Kingfisher mesocyclone. This mesocyclone evolved through multiple primary cores during its lifetime as is common (Burgess et al., 1982), but between evolutions it often had only one large identifiable core. In fact, the exceptionally large RKE of this mesocyclone (> 4 CMM from 5-10 km shown in Fig. 3b) is due to a very large core that varied between 10 and 14 km in diameter during the 20 min. prior to hailfall. The storm produced a 42 km long swath of golf ball sized hailstones. The abnormally large value of RKE of the Kingfisher storm suggests that it may be worthwhile to consider the total updraft RKE in hail production evaluations.

### 4.3 Divergence Profile

A simple evaluator of the mesocyclone structure is the orientation angle ( $\theta$ ) seen in Fig. 1. The orientation angle gives an indication of the relative strengths of rotation and divergence. When  $\theta = 45^\circ$ , for example, the components of velocity associated with rotation and divergence are equal. The change in the orientation angle with height ( $\Delta\theta$ ) provides a simple kinematic picture of the updraft, a divergence profile, that we can use to assess variations among storms. We arbitrarily assign the natural tendency towards increasing relative divergence with height as a positive orientation change.

$\Delta\theta$  is calculated over the same values of thickness and for the same persistence times as ERKE (Section 4.2). Fig. 4 presents the distribution for the 3-10 km layer at 15 min. persistence, the best performer.

$\Delta\theta$  is seen to increase linearly with increasing maximum hailstone size. As with the other predictors examined, the distribution of  $\Delta\theta$  has a tail associated with the non-hailers. But in contrast to the other predictors,  $\Delta\theta$  isolates the storms producing the largest hail. A maximum  $\Delta\theta$  of  $40^\circ$  is found for the non-hailers while  $\Delta\theta$  of storms producing 5-cm or greater hailstones averages more than  $60^\circ$ .

In 3 of the 9 hailstorms  $\Delta\theta$  peaked during hailfall, but large values prior to the event provide lead times and discrimination for size.

A threshold of  $45^\circ$  distinguishes the 5-cm or greater hail events. Lead times for these average 13 min. with no errors (FAR = 0)

Our 3.5-cm and greater events are also forecast by  $\Delta\theta$ . These are defined by a  $\Delta\theta$  of about  $35^\circ$ . An average lead time of 15 min. is achieved for these, although three false alarms are produced (FAR = 0.30). The linear relationship of  $\Delta\theta$  appears to apply also to the 2.5-cm events. For these, however, the magnitude of  $\Delta\theta$  prior to the event are very small and positive lead times are achieved at the expense of numerous false alarms.

It is appropriate to ask what aspect of the updraft is revealed by  $\Delta\theta$  to provide the successful discrimination we see for the producers of very large hail. There is one obvious possible answer: the vertical divergence structure that is revealed by  $\Delta\theta$ . To illustrate this we will examine the orientation angle ( $\theta$ ) at 10 km. This is similar to the outflow ( $\Delta V$ ) at 10 km presented in Section 4.1, except that  $\theta$  gives an indication of the relative strengths of divergence and rotation without regard to magnitude. In Fig. 5 we present maximum values of  $\theta$  at 10 km for a 5 min. persistence time, the sample time that produces the least false alarms.

As with the  $\Delta V$  distribution, for  $\theta$  we see that there is a linear relationship with hail size. Among the hailers, we find that those producing the largest hail have the largest  $\theta$  and therefore the largest component of divergence relative to rotation. However, as also seen with  $\Delta V$ ,  $\theta$  at 10 km does not distinguish the hailers from the non-hailers.

These results suggest that both the magnitude of the outflow, and the relative outflow magnitude with respect to rotation, represent a potential in hail size that may or may not be realized. It is apparently the divergence structure, as indicated here by  $\Delta\theta$ , that is a strong factor in determining which storms will produce large hail.

There are a number of contrasts in the divergence profiles among the storms that produced very large hail (3.5-cm and greater diameter) and the ones that were less productive. The very large hailers display a continuous transition from convergence at low levels to divergence aloft. In many of the lesser storms the transition to divergence is irregular.

All of the hailers display a component of convergence at low levels (3 km), but for the most part this is small, less than 10 degrees

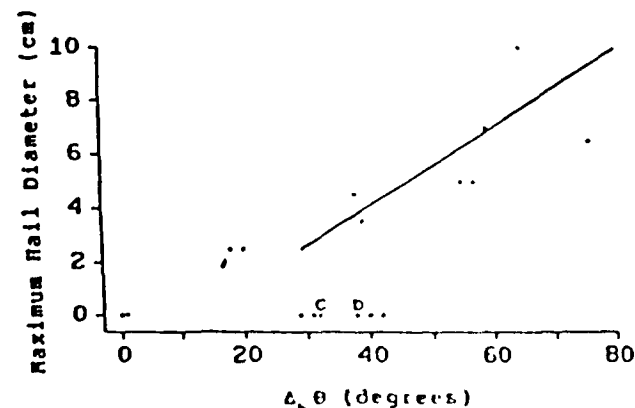


Figure 4). Same as in Fig. 2 but for values of  $\Delta\theta$ . Shown are maximum 15 min. persistence values of  $\Delta\theta$  integrated from 3-10 km AGL.

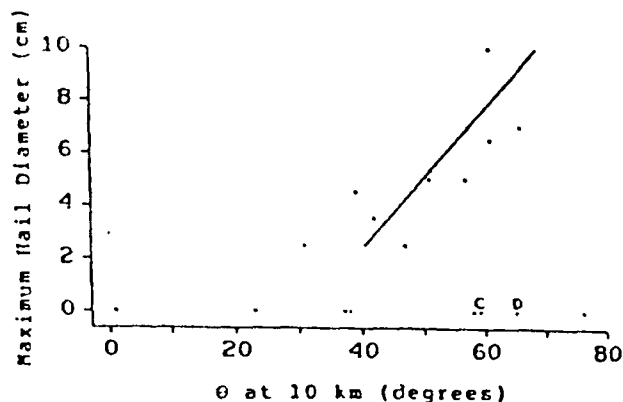


Figure 5). Same as in Fig. 2 but for values of  $\theta$  at 10 km AGL. Shown are 5 min. persistence values.

averaged over 15 min. Greater convergence is observed at lower levels. Also, all of the hailers have a significant component of divergence below 10 km height. This is not true of the non-hailers.

## 5. DISCUSSION AND CONCLUSIONS

We have examined some aspects of the mesocyclone to determine the usefulness for predicting and sizing hail events, and for distinguishing hailstorms from non-hailers. Upper level outflow ( $\Delta V$ ), rotational kinetic energy (RKE), excess rotational kinetic energy (ERKE) and the divergence profile ( $\Delta\theta$ ) were examined. With the exception of ERKE, each displays a linear relationship that varies with hail size among the hailers, and each offers lead times to hail events.

ERKE, a parameter that works well for identifying tornado potential, is found to be useless for identifying hail events. We conclude that the large shear associated with many tornadic mesocyclones is inconsequential to hail growth. In contrast, RKE delineates and forewarns very large hail events (diameters greater than 4 cm). This suggests that updraft rotation contributes to the growth of very large hail and agrees with the findings of Miller et al. (1988).

An interesting aspect of the study is that it includes cases where there was no reported hail. There is uncertainty whether hail actually fell in some of these cases, but a few of the "non-hailers" were well observed. These cases lead us to conclude that, except for very large hail, it does not appear to be possible to distinguish hailers from non-hailers with divergence or rotation. Other aspects of a storm must be considered for general hail prediction.

The divergence profile,  $\Delta\theta$ , performed the best of the parameters examined. It appears to offer excellent discrimination capability for very large hail (at least 5-cm diameter). Storms containing hail of this size are identified with an average lead time of 13 min. and are distinguished from all other storms including the non-hailers.

We conclude that the successful discrimination of hailers and non-hailers has more to do with the three-dimensional updraft structure than with actual magnitudes of the

flow. Updraft magnitude, which is related to outflow aloft, corresponds to a potential in hail size. It appears, however, that the three-dimensional flow structure must be in place for this potential to be realized, at least for very large hail.  $\Delta\theta$ , the divergence profile, is a means for quantifying the three-dimensional motion structure.

## 6. ACKNOWLEDGMENTS

I am grateful to Ralph Donaldson and Dr. Ian Harris of ST Systems Corp. (STX) for their critique of this work. They offered support and numerous useful suggestions.

## 7. REFERENCES

- Browning, K. A., 1963: The growth of large hail within a steady updraught. *Quart. J. R. Met. Soc.*, 89, 490-506.
- , and G. B. Foote, 1976: Airflow and hail growth in supercell storms and some implications for hail suppression. *Quart. J. R. Met. Soc.*, 102, 499-533.
- Burgess, D. W., V. T. Wood, and R. A. Brown, 1982: Mesocyclone evolution statistics. Preprints, 12th Conf. on Severe Local Storms, AMS, Boston, MA, 422-424.
- Donaldson, R. J., Jr., 1970: Vortex signature recognition by a Doppler radar. *J. Appl. Meteor.*, 9, 661-670.
- , and P. R. Desrochers, 1990: Improvement of tornado warnings by Doppler radar measurement of mesocyclone rotational kinetic energy. *Weather and Forecasting*, 5, xxx-xxx.
- Foote, G. B., H. V. Frank, A. J. Heymsfield, and C. G. Wade, 1982: The 22 July 1976 case study: hail growth, Vol. II, Case Studies of the National Hail Research Experiment. Colorado Assoc. Univ. Press, Boulder, CO, 181-194.
- JDOP Staff, 1979: Final Report on the Joint Doppler Operational Project (JDOP) 1976-1978. NOAA Tech. Memo., ERL NSSL - 86, 84 pp.
- Knight, C. A. and N. C. Knight, 1973: Hailstone embryos and hailstone models. Preprints, 8th Conf. on Severe Local Storms, AMS, Boston, MA, 77-79.
- Lemon, L. R., 1978: On the use of storm structure for hail identification. Preprints, 18th Conf. on Radar Meteor., AMS, Boston, MA, 203-206.
- Miller, L. J., J. D. Tuttle, and C. A. Knight, 1988: Airflow and hail growth in a severe northern high plains supercell. *J. Atmos. Sci.*, 45, 736-762.
- Nelson, S. P., 1983: The influence of storm flow structure on hail growth. *J. Atmos. Sci.*, 40, 1965-1983.
- , and S. K. Young, 1979: Characteristics of Oklahoma hailfalls and hailstorms. *J. Appl. Meteor.*, 18, 339-347.
- Rogers, R. R., 1979: A Short Course in Cloud Physics. Pergamon Press, Oxford, 235 pp.
- U.S. Department of Commerce, 1977-1987: Storm Data. Vols. 19, 20, 25, & 29, Environmental Data Service, NOAA, Asheville.
- Witt, A. and S. P. Nelson, 1984: The relationship between upper-level divergent outflow magnitude as measured by Doppler radar and hailstorm intensity. Preprints, 22nd Conf. on Radar Meteor., AMS, Boston, MA, 108-111.
- Ziegler, C. L., P. S. Ray, and N. C. Knight, 1983: Hail growth in an Oklahoma multicell storm. *J. Atmos. Sci.*, 40, 1768-1791.

**B-4: Papers on Hurricane Severity**

Donaldson Jr., R.J. and F.I. Harris, 1989: "Estimation by Doppler radar of curvature, diffluence and shear in cyclonic flow. Jour. of Atmos. and Oceanic Tech., 6, 26-35.

Donaldson Jr., R.J., 1989: Potential - Vortex Fit. Preprints, 24th Conf. on Radar Meteor. 186-189.

Harris, F.I., D.J. Hamann, and R.J. Donaldson Jr, 1989: Hurricane monitoring with Doppler radar: A simulation. Preprints, 24th Conf. on Radar Meteor., 203-206.

Ruggiero, F.H., and R.J. Donaldson Jr., 1989: Features resembling single Doppler vortex signatures observed in an extratropical cyclone. Preprints, 24th Conf. on Radar Meteor., 240-243.

Reprinted from JOURNAL OF ATMOSPHERIC AND OCEANIC TECHNOLOGY, Vol. 6, No. 1, February 1989  
American Meteorological Society

**Estimation by Doppler Radar of Curvature, Diffluence, and Shear in Cyclonic Flow**

**RALPH J. DONALDSON, JR. AND F. IAN HARRIS**



The U.S. Government is authorized to reproduce and sell this report. Permission for further reproduction by others must be obtained from the copyright owner.

## Estimation by Doppler Radar of Curvature, Diffluence, and Shear in Cyclonic Flow

RALPH J. DONALDSON, JR. AND F. IAN HARRIS

*ST Systems Corporation, Lexington, Massachusetts*

(Manuscript received 14 July 1987, in final form 18 March 1988)

### ABSTRACT

The potential for single-Doppler radar determination of wind field characteristics in cyclonic flow is examined. The influence of the four independent first-order derivatives of a wind field, namely curvature, diffluence, downwind shear, and crosswind shear, upon the Doppler radial velocities is studied. Simple models of wind fields containing each of the derivatives defined in natural coordinates are presented. When only one derivative is present at a time, it has been found that there are unique signatures for diffluence and downwind shear and qualitatively similar signatures for curvature and crosswind shear. With a model incorporating all four derivatives, techniques are developed for the recovery of these derivatives. A method is also presented that corrects the mean speed estimate. It is concluded that in most cases the recovery of the downwind shear, diffluence, the sum of curvature and crosswind shear, and mean wind is possible to within 5 percent of the true values.

Application of these techniques to radar data collected from Hurricane Gloria is discussed. A storm strength indicator based on shearing deformation and distance of cyclone center yielded signs of the declining trend of the storm an hour or two before this trend manifested itself significantly in the wind speed as estimated by the Doppler radar, therefore suggesting potential as a forecast tool.

### 1. Introduction

Wind field analysis through use of a single-Doppler radar was first suggested by Probert-Jones (1960). He observed the component of motion of snow along his radar beam at two different azimuth angles and deduced the wind speed and direction appropriate to both azimuths. The Velocity Azimuth Display (VAD) scan was offered by Lhermitte and Atlas (1961). It is a simple and efficient technique for systematic estimation of wind speed and direction when suitably reflective wind tracers surround the radar. In the VAD mode, the radar antenna is set into a conical scan about a vertical axis, at a fairly low elevation angle in order to prevent excessive contribution to the Doppler velocity measurements by precipitation fall speeds. These measurements, recorded at a particular range during a complete 360° scan in azimuth, provide information on the wind field along the VAD scanning circle at a height given by range and elevation angle.

Both Probert-Jones and Lhermitte and Atlas recognized the underlying assumption in their techniques of a horizontally uniform wind vector throughout the area of observation. Eventually the uniformity assumption was replaced by a less restrictive assumption of linearity. Browning and Wexler (1968) extended the VAD technique to a consideration of nonuniform wind fields that vary linearly in the horizontal plane. A linear

wind field is also a necessary assumption in the generalized VVP method (Volume Velocity Processing) developed by Waldteufel and Corbin (1979).

The assumption of linearity utilized in all of the above estimation techniques tends to break down when intense cyclonic storms such as hurricanes are considered. Observations of such storms by ground-based Doppler radars are limited, but there are strong suggestions of nonlinear effects (e.g., Donaldson et al. 1978). Passarelli (1983) explored the opportunities for analysis by single-Doppler radar of nonlinear wind fields. Inspired by his commentary, Donaldson and Harris (1984) initiated a study to assess the effects of variable wind curvature and linear wind field gradients upon VAD patterns through simulations. Their results were encouraging and provided the motivation for this in-depth study to examine all four first-order derivatives of the winds in cyclonic flow, with curvature inversely proportional to distance from its center, and to develop methods for recovery of these derivatives, whenever possible.

### 2. First derivatives of the wind field

The analysis presented here considers first-order spatial derivatives of wind velocity in a horizontal plane. Because the focus of this study is upon cyclones, wherein variable curvature is likely, the derivatives are expressed most conveniently in natural coordinates referred to the streamlines. In the natural coordinate system the  $s$ -axis is tangent to a streamline with  $s$  increasing downwind, the  $n$ -axis is normal to a streamline

Corresponding author address: Mr. Ralph J. Donaldson, ST Systems Corporation, 109 Massachusetts Avenue, Lexington, MA 02173.

with  $n$  increasing to the left of the wind vector and  $V$  is wind speed at the origin of the natural coordinate axes. A change in wind direction is denoted by the angle  $\psi$ , which is positive toward the  $n$ -axis. Both speed and direction may vary along either of the coordinate axes; thus there are four independent first-order derivatives:  $\partial V/\partial s$  (downwind shear),  $\partial V/\partial n$  (crosswind shear),  $V\partial\psi/\partial s$  (curvature), and  $V\partial\psi/\partial n$  (diffluence).

It is well known (e.g., Petterssen 1956) that the kinematic properties of a wind field are given by sums and differences of its first-order derivatives. Expressed in natural coordinates, the kinematic properties are:

$$\text{Divergence} = \partial V/\partial s + V\partial\psi/\partial n \quad (1)$$

$$\text{Stretching Deformation} = \partial V/\partial s - V\partial\psi/\partial n \quad (2)$$

$$\text{Shearing Deformation} = V\partial\psi/\partial s + \partial V/\partial n \quad (3)$$

$$\text{Vorticity} = V\partial\psi/\partial s - \partial V/\partial n \quad (4)$$

The first three of these kinematic properties may be calculated from the Doppler VAD patterns. Caton (1963) showed that divergence is the net horizontal outflow integrated throughout the radar scanning circle divided by its radius. Browning and Wexler (1968) showed how the two components of deformation can be determined from the amplitude and phase of the second-order Fourier harmonic of the Doppler VAD pattern, assuming that the wind field derivatives can be considered as constant throughout the radar scanning circle.

Our examination of the wind field derivatives is intended to provide an aid for diagnosis of hurricanes and other intense cyclonic storms. Consequently, we have expressed curvature as inversely proportional to distance from a center of curvature, as a highly simplified first approximation to flow around a cyclone. Also, we have expressed diffluence as inversely proportional to distance from a virtual streamline apex, in order to preserve streamline continuity. We shall test the range of applicability of the Browning and Wexler technique in a wind field with curvature and diffluence varying according to our simple model of cyclonic flow.

It is convenient to reference the radar observations of Doppler velocity, defined as the scalar component of wind velocity along the radar beam, to a polar coordinate system with origin at the radar, and position defined by range  $r$  and azimuth angle  $\alpha$ . Following geographical convention, and postulating for the moment a mean westerly wind, we align the coordinate system so that the wind across the radar site is moving toward  $\alpha = 90^\circ$  and the orthogonal direction to the left of the wind is  $\alpha = 0^\circ$ . Stated in Cartesian coordinates, these directions are along the  $x$  axis and  $y$  axis, respectively. For the sake of simplicity we assume that radar elevation angles and vertical motions are sufficiently small so that their neglect introduces errors of negligible importance in comparison with contribu-

tions from other sources. An estimated correction for contamination by vertical motions could be introduced, if necessary.

Figure 1 depicts each of the first derivatives, combined with uniform translation from left to right, in the context of the radar scanning circle. The radius of the radar scanning circle is  $r$ , and  $F$  and  $R$  represent distances to the centers of diffluence and curvature, respectively. Initially, we shall examine the Doppler VAD patterns specific to each one of the wind fields illustrated in Fig. 1. In later sections combinations of the wind field derivatives and their resultant VAD patterns will be studied, including the general case in which all four derivatives are present.

#### a. Downwind shear

Figure 2 illustrates the geometry of the radar scanning circle (dashed) of radius  $r$  observing a wind field with both downwind and crosswind shear. The wind speed at the radar site is  $V_0$ . In the case of downwind shear, the wind speed increases from a minimum of  $V_0(1 - d)$  at distance  $r$  upwind from the radar to  $V_0(1 + d)$  at distance  $r$  downwind from the radar. Accordingly, the shear is  $V_0 d/r$ . The dimensionless parameter  $d$  is defined as the fractional increase in wind speed from radar site downwind to the VAD scanning circle.

At any point on the radar scanning circle, this wind field has a speed of

$$V(\alpha) = V_0(1 + d \sin \alpha) \quad (5)$$

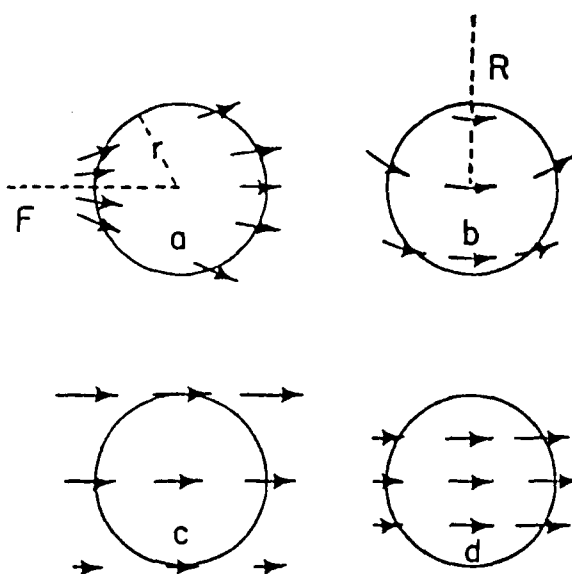


FIG. 1. Schematic depiction of the four first derivatives of the horizontal wind field: (a) Diffluence, (b) Curvature, (c) Crosswind shear, and (d) Downwind shear. Each derivative is superimposed on a radar scanning circle of radius  $r$ . Arrows indicate wind vectors representing the sum of a derivative and a constant translation toward the right of each sketch. (From Ruggiero and Donaldson 1987).

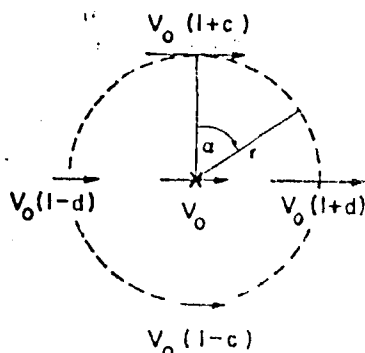


FIG. 2. Schematic depiction of linear wind field model with both downwind and crosswind shear. Arrows represent wind vectors, dashed line is radar scanning circle of radius  $r$ , with location on circle given by azimuth angle  $\alpha$ . (From Donaldson and Harris 1984).

and a uniform direction toward  $\alpha = 90^\circ$ . Accordingly, the Doppler velocity  $V_D$ , the component of wind along the radar beam, is

$$V_D(\alpha) = V(\alpha) \sin \alpha = V_0(\sin \alpha + d \sin^2 \alpha). \quad (6)$$

A visual examination of the VAD pattern readily reveals the presence of downwind shear by noting a difference in magnitude of the maximum and minimum values of Doppler velocity. These extrema occur at  $\alpha = 90^\circ$  and  $270^\circ$ , respectively, for the simple case of downwind shear expressed in Eq. (6), yielding a straightforward method for evaluation of  $d$ :

$$d = [V_D(\max) + V_D(\min)] / [V_D(\max) - V_D(\min)]. \quad (7)$$

#### b. Crosswind shear

The wind speed at any point on the radar scanning circle for the case of pure crosswind shear, with uniform wind direction toward  $\alpha = 90^\circ$ , is

$$V(\alpha) = V_0(1 + c \cos \alpha). \quad (8)$$

The shear toward the left of the wind direction is  $V_0 c/r$ , where  $c$  is the dimensionless parameter of crosswind shear and is defined as the fractional increase in wind speed over a distance  $r$  normal and to the left of wind direction. Under these conditions the Doppler velocity measured by the radar is

$$V_D(\alpha) = V(\alpha) \sin \alpha = V_0(\sin \alpha + c \sin \alpha \cos \alpha). \quad (9)$$

The most prominent effect of crosswind shear on a visual display of the Doppler VAD pattern is a deviation from diametric opposition of the locations of the maximum and minimum Doppler velocities. Unfortunately, the cause of this effect is not unique, because later discussion will demonstrate that a curved wind field produces a pattern rather similar in appearance. Figure 3 illustrates this deviation, which is measured

by the angle  $\delta_D$  on the downwind side of the pattern, and  $\delta_U$  on the upwind side. (The  $\epsilon$  angles will be discussed later in the section on diffluence.)

The  $\delta$  angles are useful for an immediate visual recognition of the presence of crosswind shear and/or curvature. Also, in cases where data coverage is not complete around the VAD circle but the  $\delta$  angles are clearly displayed, their magnitude provides a qualitative indication of the combined effects of crosswind shear and curvature. For example, if crosswind shear is the only wind field derivative,  $\delta_D = \delta_U$ , and these angles may be determined by differentiation of (9) with respect to  $\alpha$  to find the angular locations of the Doppler velocity extrema, which have a complementary relationship to the two identical  $\delta$  angles. This process yields

$$\sin \delta = [(1 + 8c^2)^{1/2} - 1]/4c \quad (10)$$

and can also be expressed more compactly as

$$c = \sin \delta / \cos 2\delta. \quad (11)$$

Note that  $c$  and  $\delta$  have the same sign in (10) and (11), and therefore the Doppler velocity extrema are displaced toward the direction of positive crosswind shear.

#### c. Curvature

Following the discussion of Donaldson and Harris (1984), we have assumed that curvature is inversely proportional to distance from a center of curvature that has a fixed position relative to the radar location. This assumption of variable curvature but fixed center of curvature has two distinct advantages: it provides a simple depiction of wind field curvature around a cyclone, and it defines geometric relationships between the wind field and the radar scanning circle that enable calculation of Doppler velocities by straightforward trigonometric manipulation.

The geometry of a radar scanning a curved wind field is portrayed in Fig. 4. (Ignore for the moment

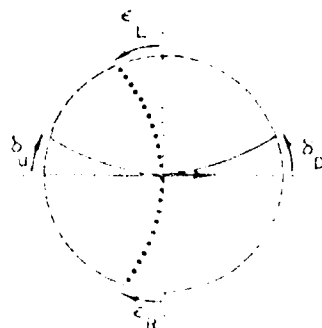


FIG. 3. Illustration defining the angles  $\delta_U$ ,  $\delta_D$ ,  $\epsilon_U$ , and  $\epsilon_D$ . Dashed line is radar scanning circle, dotted lines indicate directions along and normal to wind vector (arrows) at the radar, solid line is locus of minimum or maximum Doppler velocity, small circles show loci of zero Doppler velocity.

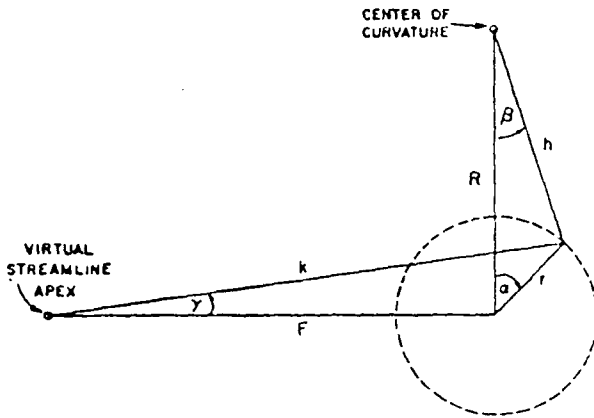


FIG. 4. Portrayal of geometric relationships required for specification of curvature and diffuence and their Doppler velocities. Dashed line is radar scanning circle, with  $\alpha$  as the azimuth angle of any arbitrary point on this circle.  $R$  and  $h$ , with inclusive angle  $\beta$ , are distances from center of wind field curvature to radar and to the arbitrary point on the radar scanning circle, respectively.  $F$  and  $k$ , with inclusive angle  $\gamma$ , are distances from virtual streamline apex to radar and to the same arbitrary point, respectively.

distances  $F$  and  $k$  and angle  $\gamma$ ; these will enter our discussion of diffuence in the next section.) The distance  $r$  is the radius of the radar scanning circle and  $R$  is the distance from the radar to the center of curvature of the wind field. The radar scanning angle  $\alpha$  is oriented so that the center of curvature is in the direction  $\alpha = 0^\circ$ . The wind direction at the radar site is toward  $\alpha = 90^\circ$ , appropriate to cyclonic curvature in the Northern Hemisphere. The variable  $h$  is the distance from center of curvature to any point on the radar scanning circle. This point is also located by the angle  $\beta$  measured from the line  $R$  joining the center of curvature and the radar. The angle  $\beta$  is positive for the downwind semi-circle, where  $0^\circ < \alpha < 180^\circ$ . Our analysis requires the assumption that  $r < R$ , and this is easily granted because  $r$  is under human control. The wind speed  $V_0$  is assumed uniform.

The curved wind field can be expressed in Cartesian coordinates as the vector sum of components  $u$  and  $v$ , where  $u$  is directed along  $\beta = 90^\circ$  and  $v$  along  $\beta = 180^\circ$ . Inspection of Fig. 4 readily shows that  $u = V_0 \cos \beta$  and  $v = V_0 \sin \beta$ . The radar can detect motion only along its beam. Accordingly, at any location on the radar scanning circle the Doppler velocity  $V_D$  is given by wind components along the direction  $\alpha$ . Therefore,

$$V_D(\alpha) = u \sin \alpha + v \cos \alpha \\ = V_0(\sin \alpha \cos \beta + \cos \alpha \sin \beta). \quad (12)$$

Through trigonometric solution of the right triangle in Fig. 4 that has  $h$  as hypotenuse and  $\beta$  as one of its angles, and after some algebraic manipulation, we find that  $h = R\rho^{1/2}$ , so that (12) can be expressed simply as a function of radar scanning angle  $\alpha$  and a dimension-

less parameter  $r/R$  relating the radii of radar scanning circle and curvature:

$$V_D(\alpha) = \rho^{-1/2} V_0 \sin \alpha, \quad (13)$$

where  $\rho = 1 + (r/R)^2 - 2(r/R) \cos \alpha$ . Note that  $V_0 \sin \alpha$  in (13) is the VAD pattern of a uniform linear wind directed toward  $\alpha = 90^\circ$ , so the factor  $\rho^{-1/2}$  is the modification of the VAD effected by curvature varying inversely with distance to the center of curvature.

The increment of direction per unit distance along a streamline ( $\partial\psi/\partial s$ ) for a circularly curved wind field is the inverse of the radius of curvature. Consequently, the curvature term appearing in (3) and (4) is evaluated in our model wind field as  $V_0/h = V_0/R\rho^{1/2}$  at any point on the radar scanning circle. The curvature term at the radar site, where  $r = 0$  and  $\rho$  reduces to unity, is simply  $V_0/R$ .

The effect of curvature on the Doppler VAD pattern is qualitatively similar to the effect of crosswind shear: the maximum and minimum Doppler velocities are displaced toward the center of curvature. The effect is illustrated by the  $\delta$  angles of Fig. 3. If curvature is the only wind field derivative, the upwind and downwind  $\delta$  angles are equal and may be determined by differentiation of (13) with respect to  $\alpha$ . An alternate and simpler method for calculation of  $\delta$  starts with the reflection that the extrema in the VAD pattern of a curved wind field without speed gradients occur at the two angles where the wind direction is aligned with the radar beam. Therefore, the angular locations of the extrema are obtained by setting  $V_D = \pm V_0$  in (13) and solving for  $\alpha$ . The solution is  $\cos \alpha = r/R$ , and since  $\delta$  is complementary with the angular location of a maximum or minimum in the VAD pattern,

$$r/R = \sin \delta. \quad (14)$$

#### d. Diffuence

Diffuence, like curvature, is characterized by non-uniform wind direction. Unlike curvature, the diffuent directional shift is along a line normal to a streamline. Heretofore, the quantitative measurement of diffuence by a single Doppler radar has not been considered explicitly, although Baynton et al. (1977) showed that the presence of diffuence is very easily recognized in a Doppler VAD pattern by an asymmetric locus of zero-Doppler velocity. Since the zero-Doppler locus indicates wind directions normal to the radar beam, any deviation of the two branches of this locus from opposition at the same range reveals a cross-flow difference in wind direction at the corresponding height.

A field of constant translation with constant diffuence as its only derivative does not appear to be a realistic possibility within a horizontal plane. We were not able to envision continuous streamlines through a uniformly diffuent field unless the streamlines were also curved, with curvature increasing with the cu-

mulative effect of diffluence. Consequently, we have selected a diffluence model in which linear streamlines radiate from a fictitious virtual streamline apex. The diffluent wind vectors are sketched in Fig. 1(a), and geometrical relationships of the virtual streamline apex with the radar scanning circle are depicted in Fig. 4. The distance from streamline apex to radar is  $F$ , and to any point on the radar scanning circle is  $k$ . The angle between the  $F$  and  $k$  lines is  $\gamma$ , considered positive in the counterclockwise direction. The coordinates  $r$  and  $\alpha$  of the radar scanning circle are identical to the case for curvature, with coordinate axes aligned so that wind direction at the radar site is toward  $\alpha = 90^\circ$ .

An expression for a diffluent wind field and its Doppler velocity measured by a radar in VAD scanning mode can be generated in a manner analogous to the derivation employed in the previous section for our curved wind field model. The variable diffluent wind field can be expressed in Cartesian coordinates as the vector sum of components  $u$  and  $v$ , where  $u$  is directed along  $\gamma = 0^\circ$  and  $v$  along  $\gamma = 90^\circ$ . In the absence of shear the wind speed has a uniform value  $V_0$ , and with wind direction dependent only on diffluence, Fig. 4 shows that  $u = V_0 \cos \gamma$  and  $v = V_0 \sin \gamma$ . Since the radar detects motion only along its beam, the Doppler velocity  $V_D$  at any point on the radar scanning circle is given by wind components along the beam direction  $\alpha$ . Therefore,

$$\begin{aligned} V_D(\alpha) &= u \sin \alpha + v \cos \alpha \\ &= V_0(\sin \alpha \cos \gamma + \cos \alpha \sin \gamma). \end{aligned} \quad (15)$$

Substitution for  $\gamma$  in (15) may be accomplished by trigonometric solution of the right triangle in Fig. 4 that has  $k$  as hypotenuse and  $\gamma$  as one of its angles. It is helpful to express  $k = F\phi^{1/2}$ , where  $\phi = 1 + (r/F)^2 + 2(r/F) \sin \alpha$ . By means of these manipulations, (15) may be expressed as a function of radar scanning angle  $\alpha$  and a dimensionless parameter  $r/F$  relating radius of the radar scanning circle  $r$  to the distance  $F$  from radar to the virtual streamline apex:

$$V_D(\alpha) = \phi^{-1/2} V_0 (\sin \alpha + r/F). \quad (16)$$

Note that (16) reduces to the VAD pattern of a uniform linear wind directed toward  $\alpha = 90^\circ$  when  $F$  is infinitely distant, indicating a condition of zero diffluence. Also, for a confluent, or negatively diffluent, wind field the virtual streamline apex would be downwind or to the right of the radar in Fig. 4, and  $F$  would be considered negative.

The diffluence term in Eqs. (1) and (2),  $\partial\psi/\partial n$ , may be evaluated in either of two ways. In our diffluent model wind field, diffluence is dependent only on distance  $k$  from the virtual streamline apex. This condition requires that  $\partial\psi/\partial n$  be constant along any curve normal to a streamline. Therefore we can easily integrate  $\psi$  from 0 to  $\psi_1$ . The corresponding integration for  $n$  is a circular arc length with angle  $\psi_1$  and radius equal to

distance  $k$  on Fig. 4 from any given point on the radar scanning circle to the virtual streamline apex. Accordingly, the diffluence term is  $V_0\psi_1/\psi_1 k = \phi^{-1/2} V_0/F$ , recalling that  $k = F\phi^{1/2}$ . At the radar site  $\phi$  reduces to unity and the diffluence term is simply  $V_0/F$ .

The other method for evaluating diffluence is calculation of divergence under the condition of uniform wind speed  $V_0$ , which requires  $\partial V/\partial s = 0$  in Eq. (1). We can do this by calculating the net outflow from a small area of width  $\Delta s$  with curved sides everywhere normal to the diffluent wind field and subtending an angle  $\psi_1$ . In our diffluent wind field model we set the radius of one curved side as  $k$  and the other (downwind) side as  $k + \Delta s$ . In this way we relate the calculation of divergence to radar parameters, because  $k$  terminates at any arbitrary point on the radar scanning circle. The inflow to this curved area is  $V_0 k \psi_1$  and outflow is  $V_0(k + \Delta s)\psi_1$ , with no flow across the narrow sides of width  $\Delta s$  because these sides are oriented along the direction of flow. The size of the area in question is infinitesimally larger than  $k\psi_1 \Delta s$ . Consequently the divergence, and also the diffluence, is  $\{V_0(k + \Delta s)\psi_1 - V_0 k \psi_1\}/k\psi_1 \Delta s = V_0/k = \phi^{-1/2} V_0/F$ , which is identical to the previous calculation.

The easily recognizable signature of diffluence in the Doppler VAD pattern is a departure from opposition of the locus of zero Doppler velocity on either side of the mean wind vector, as illustrated in Fig. 3 by the angles  $\epsilon_L$  and  $\epsilon_R$ . Subscripts  $L$  and  $R$  denote the deviation from normal to the mean wind on its left and right sides. Diffluence is indicated by skewing upwind of the zero Doppler locus, as depicted in Fig. 3. A skewing downwind of the zero Doppler locus would indicate confluence, in which case the  $\epsilon$  angles would be considered negative by our convention. In the absence of curvature, the two  $\epsilon$  angles are equal, regardless of the presence or absence of crosswind and/or downwind shear.

The  $\epsilon$  angles may be easily evaluated by solving Eq. (16) for  $\alpha_0$ , the zero-crossing angles of the radar scan. For all values of  $(r/F) < 1$ ,  $\phi > 0$  and the solution is  $\sin \alpha_0 + r/F = 0$ . From our definition of  $\epsilon$  as portrayed in Fig. 3,  $\epsilon_L = -\alpha_{0L}$  and  $\epsilon_R = \alpha_{0R} - \pi$ . Consequently  $\sin \epsilon_L = -\sin \alpha_{0L}$  and

$$r/F = \sin \epsilon. \quad (17)$$

This is a useful relationship for achieving a quick estimate of the sign and magnitude of diffluence from a cursory examination of the Doppler VAD pattern, because the Doppler velocity changes most rapidly with radar scanning angle at a zero crossing. On this account the zero crossing angle is least likely to be affected by small-scale perturbations in the wind field.

### 3. Combination of curvature and crosswind shear

Donaldson and Harris (1984) examined the interaction combination of curvature and crosswind shear,

in which both derivatives are readily recognized by a  $\delta$  signature in the VAD pattern, as given by Eq. (10) or (11), and (14), and both derivatives contribute to the shearing deformation. This earlier analysis, with slightly different notation, is reproduced here. As in the previous section, we postulate flow around a cyclone, with curvature varying inversely with distance from the center of circulation.

In combination with curvature, the crosswind shear has a variable direction because it is normal to the curved streamlines and directed toward the center of curvature. However, the wind vector and its Doppler velocity may be defined through the geometry of Fig. 4. The wind speed at any point on the VAD circle is a linear function of  $h = R\rho^{1/2}$ , the distance from center of wind field curvature to an arbitrary location observed by the radar. The speed function may be determined by assigning  $V = V_0$  at the radar and noting, through Eq. (8), that  $V(h) = V_0(1 + c)$  for  $\alpha = 0^\circ$ ; and at this point on the radar scanning circle Fig. 4 shows that  $r = R - h$ . Accordingly,

$$V(h) = V_0[1 + c(R - h)/r] \\ = V_0[1 + c(r/R)^{-1}(1 - \rho^{1/2})]. \quad (18)$$

The direction of the wind field is identical to the case of curvature without shear, so the Doppler velocity of the curvature-crosswind shear combination is similar to (13), but with  $V(h)$  substituted for  $V_0$ :

$$V_D(\alpha) = \rho^{-1/2} V_0[1 + c(r/R)^{-1}(1 - \rho^{1/2})] \sin \alpha. \quad (19)$$

A remarkable simplification of (19) occurs in the case of solid rotation, wherein rotational speed increases linearly with distance from the center of curvature. If the radar scanning circle is entirely within the region of solid rotation (e.g., within the area bounded by the eye wall of a hurricane), we may write  $V_0/R = V_0(1 + c)/(R - r)$ , which reduces to

$$c(\text{solid rotation}) = -r/R. \quad (20)$$

Substitution of this relationship into (19) reduces its bracketed factor to  $\rho^{1/2}$ , finally leaving  $V_D(\alpha) = V_0 \sin \alpha$ . Within solid rotation, the effects on Doppler velocity of curvature and crosswind shear cancel exactly, and the resultant VAD pattern is identical to that observed with pure translation.

Potential vortex flow, with wind speed inversely proportional to distance from a cyclone center, is another regime of special interest. This type of flow may be a better approximation to a hurricane wind field, beyond the radius of maximum wind speed, than is a linear crosswind shear.

In potential vortex flow the product of wind speed around a circulation center and distance from this center is constant. Consulting Fig. 4, then, we see that the wind speed at any point on the radar scanning circle is

$$V(\alpha) = V_0 R/h = V_0 \rho^{-1/2}, \quad (21)$$

where, as before,  $V_0$  is wind speed at the radar location. The Doppler velocity, with wind field direction identical to the case of curvature, is given by (13) with wind speed function (21) substituted for the constant speed  $V_0$  of (13):

$$V_D(\alpha) = \rho^{-1/2} V_0 \rho^{-1/2} \sin \alpha = \rho^{-1} V_0 \sin \alpha. \quad (22)$$

Differentiation of (22) with respect to  $\alpha$  reveals, as expected, considerably greater deviation of the Doppler velocity extrema from the mean wind vector, than in the simple relationship (14) for curvature with uniform wind speed:

$$\sin \delta = 2(r/R)/[1 + (r/R)^2]. \quad (23)$$

#### 4. An approximation for the combination of all four wind field derivatives

When both curvature and diffluence are present the simple trigonometric relationships of Fig. 4 for either curvature or diffluence alone are not valid. The lines  $F$  and  $R$  joining the radar location with virtual streamline apex and center of curvature, respectively, are no longer straight, and the angles  $\gamma$  and  $\beta$  are no longer defined in terms of right triangles. Also, these two angles are interdependent. An exact solution for the wind field and its Doppler velocity could not be derived. Therefore, approximations were sought relating  $\beta$  and  $\gamma$  to radar parameters. By inductive reasoning, we proposed that

$$\sin \beta \approx (k - F)/h \quad \text{and} \quad \sin \gamma \approx (R - h)/k \quad (24)$$

would be reasonable approximations, retaining the definitions for  $h = R\rho^{1/2}$  and  $k = F\phi^{1/2}$  used in the earlier analysis of single derivatives, with  $\rho$  as before equal to  $1 + (r/R)^2 - 2(r/R) \cos \alpha$  and  $\phi = 1 + (r/F)^2 + 2(r/F) \times \sin \alpha$ .

The approximations stated in (24) approach equality as  $F \gg r$  (for  $\sin \beta$ ) and as  $R \gg r$  (for  $\sin \gamma$ ). Reference to Fig. 4 shows that each approximation converges to its exact independent form as the other term vanishes. That is,  $(k - F) \rightarrow r \sin \alpha$  as  $F \rightarrow \infty$  and  $(R - h) \rightarrow r \cos \alpha$  as  $R \rightarrow \infty$ . At the approach of these limits, the centers of rotation and diffluence are separated by  $90^\circ$  as seen from the radar.

We propose now to use the approximations of (24) to develop an expression for the VAD pattern when all four wind field derivatives of our model are present. We will then test the accuracy of the wind field derivatives recoverable by Fourier analysis from this expression, and suggest a range of parameter values wherein the Browning and Wexler technique can be used for successful practical analysis of cyclonic wind fields that may incorporate nonuniform derivatives.

The angles  $\beta$  and  $\gamma$  indicate the changes in wind direction owing to curvature and diffluence, respectively. When both of these derivatives are present, but with no shear, the Doppler velocity of the VAD pattern is

$$V_D(\alpha) = V_0 \sin(\alpha + \alpha_0 + \alpha_1 r) \quad (27)$$

where, as before,  $V_0$  is wind speed in direction  $\alpha_0$ . Substitution of the approximations of (25) and (26) eventually yields an expression for wind speed  $V_D$  with both curvature and diffuence present, but with no shear. This expression is stated in terms of the radar coordinates  $r$  and  $\alpha$  and the dimensionless parameters  $r/R$  and  $r/F$  of curvature and diffuence:

$$V_D(\alpha) \approx V_0 \sin\{\alpha + \sin^{-1}[(r/R)(r/F)^{-1/2}(\phi^{1/2} - 1)] + \sin^{-1}[(r/F)(r/R)^{-1/2}(1 - \phi^{1/2})\phi^{1/2}]\} \quad (28)$$

The next step in the problem is approximation of the two shears when there is both curvature and diffuence. Consider first downwind shear. Along the curved streamline that crosses the radar location, an expression is required for streamline length from radar to scanning circle. The product of downwind shear  $V_0 d\alpha/dr$  and the length of this curved streamline segment defines the wind speed at the points where this streamline and  $\alpha$  intersects the radar scanning circle. Finally, a general expression is required for wind speed at any point on the radar scanning circle, reducible to the simple expression  $V(\alpha) = V_0(1 + d \sin \alpha)$  for linear, parallel streamlines as both curvature and diffuence approach zero.

The distance along a curved streamline from radar location to scanning circle is only slightly greater than the radius  $r$  of the scanning circle. In fact, it can be demonstrated that the difference is only 1% for the fairly large value of  $r/R = 0.5$ . Even at the limiting value of  $r/R = 1$ , the difference is only 5%. Consequently, the approximation of  $r$  for streamline distance from radar to scanning circle is acceptable for all permissible values of  $r/R$ . By a similar argument,  $r$  is a suitable approximation, throughout all permissible values of  $r/F$ , for distance from the radar location to the intersection of the radar scanning circle with the streamline-normal curve for diffuence alone.

Next, a reasonable approximation is needed for distance downwind from radar location to any point on the radar scanning circle, a distance  $k$  (measured in the left direction) to this same arbitrary point (see Fig. 4). It appears that  $k \approx F$  approaches the downwind distance, and  $R \approx h$  approaches the crosswind distance, as  $r \rightarrow \infty$  and  $r/F \rightarrow 0$ . For  $F \rightarrow \infty$  and  $R \approx h \rightarrow r$ , the two distance approximations merge smoothly into the distance  $r$  wherein curvature and diffuence are both zero.

It is now possible to express wind speed  $V_D$  on the radar scanning circle in terms of radar coordinates and the dimensionless parameters of curvature and diffuence. The increment  $\alpha_1$  in (27) is the distance to scanning circle is the appropriate distance  $k$  defined by the appropriate distance  $r$  in (28):

$$\text{downwind } V_D(\alpha) = V_0 \sin(\alpha + \alpha_0 + \alpha_1 k) \quad (29)$$

$$\text{crosswind } V_D(\alpha) = V_0 \sin(\alpha + \alpha_0 + \alpha_1 R) \quad (28)$$

where  $\alpha_1$  is a function of position on the radar scanning circle,  $\alpha_1 = V_0^{-1} dV_D/d\alpha$  at the radar multiplied by the product of two shear-dependent factors implicit in (27) and (28). Also, substitution of  $R$  for  $r$  and  $\phi^{1/2}$  for  $\phi$  reduces all variables to radar coordinates and parameters of the wind field derivatives. Finally, substitution of the resultant speed function for  $V_D$  in (29) provides a general approximation for Doppler velocity  $V_D \cos \theta$  of four derivatives of our model wind field for  $\theta = 0$ . The final expression is

$$\begin{aligned} V_D \cos \theta &= V_0 \{ [1 + \phi(r/R)^{-1/2}(1 - \phi^{1/2})] \\ &\times [1 + d(r/F)^{-1/2}(\phi^{1/2} - 1)] \\ &\times \sin\{\alpha + \sin^{-1}[(r/R)(r/F)^{-1/2}(\phi^{1/2} - 1)] \\ &\times \sin^{-1}[(r/F)(r/R)^{-1/2}(1 - \phi^{1/2})\phi^{1/2}]\} \}. \end{aligned} \quad (29)$$

It is not difficult to demonstrate that (29) reduces to one of the exact forms (13) or (16) when either diffuence or curvature is not present and there is no shear, or to (6) or (9) when both curvature and diffuence are absent but either downwind or crosswind shear is present. With no diffuence,  $r/F = 0$  and  $\phi^{1/2} = 1$ . Simple substitution of these values in (29) would result in  $\phi^{1/2}$  in one of its factors. In order to avoid this indeterminacy, some considerations are required. Recall that  $\phi = 1 + (r/F)^2 + 2(r/F) \sin \alpha$ . As diffuence approaches zero,  $\phi$  approaches very large values, at which  $\phi^{1/2} \approx 1 + (r/F) \sin \alpha$ ,  $\phi^{1/2} \approx 1 + (r/F) \sin \alpha$ , and  $(r/F)^{-1/2}(\phi^{1/2} - 1) \approx \sin \alpha$ . Similarly, as curvature approaches zero and  $R$  approaches very large values,  $(r/R)^{-1/2}(1 - \phi^{1/2}) \approx \sin \alpha$ . Therefore, for zero diffuence (and, therefore, zero curvature), the directional factor  $\sin^{-1}\{—\}$  in (29) reduces to  $\sin^{-1}[\sin \alpha] = \alpha$  and  $\sin^{-1}[(r/F)^{-1/2}(\phi^{1/2} - 1)]$  and  $\sin^{-1}[(r/R)^{-1/2}(1 - \phi^{1/2})\phi^{1/2}]$  can be written in a form  $\sin^{-1}[\sin \alpha]$  and eventually simplified to  $\alpha$ . Similarly, for zero curvature (but not diffuence), the directional factor  $\sin^{-1}[\sin \alpha]$  reduces to  $\alpha$  and  $\sin^{-1}[(r/R)^{-1/2}(1 - \phi^{1/2})\phi^{1/2}]$  can be written in a form  $\sin^{-1}[\sin \alpha]$  and eventually simplified to  $\alpha$ . Finally, for zero shear,  $\phi^{1/2} = 1$  and  $\phi^{1/2} - 1 = 0$ . In this case, the directional factor  $\sin^{-1}[\sin \alpha]$  reduces to  $\alpha$  and  $\sin^{-1}[(r/F)^{-1/2}(\phi^{1/2} - 1)]$  can be written in a form  $\sin^{-1}[\sin \alpha]$  and eventually simplified to  $\alpha$ . As a result, (29) reduces to (13) or (16) for zero shear, to (6) or (9) for zero curvature, and to (2) or (5) for zero diffuence.

Figure 5 shows the variation of the wind speed  $V_D$  and the Doppler velocity  $V_D \cos \theta$  with the radar coordinate  $\alpha$  for the case of zero shear.

Figure 6 shows the variation of the wind speed  $V_D$  and the Doppler velocity  $V_D \cos \theta$  with the radar coordinate  $\alpha$  for the case of zero curvature. The solid line represents the case of zero diffuence, and the dashed line represents the case of zero diffuence and zero shear. The solid line represents the case of zero diffuence and zero shear, and the dashed line represents the case of zero diffuence and zero shear.

With neither curvature nor diffluence,

$$V_D(\alpha) = V_0[1 + c \cos \alpha][1 + d \sin \alpha] \sin \alpha. \quad (32)$$

It is satisfying to note that (30) with  $d = 0$  is identical to (19), which was derived along an approach somewhat different from the reasoning behind (30).

The validity of the general approximation (29) may be tested for any arbitrary combination of the dimensionless parameters ( $c$ ,  $d$ ,  $r/R$ ,  $r/F$ ) of the four wind field derivatives (crosswind shear, downwind shear, curvature, and diffluence). The method of testing first requires synthesis of the Doppler velocity function  $V_D(\alpha)$  for a complete VAD circle by insertion of the arbitrary parameter values in (29). The next step is a Fourier analysis of the synthesized  $V_D(\alpha)$  function, using the method developed by Browning and Wexler (1968). The Fourier coefficients of zeroth, first, and second order are  $a_0$ ,  $a_1$  and  $b_1$ , and  $a_2$  and  $b_2$ , respectively. In performing this analysis care is taken to assure that the wind vector at the radar location is directed toward  $\alpha = 90^\circ$ . With this precaution,  $b_1$  estimates the mean wind speed around the VAD scanning circle and  $a_1 = 0$  or very nearly so. Divergence is given by  $a_0/r$ , stretching deformation by  $-2a_2/r$ , and shearing deformation by  $2b_2/r$ . (The negative sign for the coefficient in stretching deformation is a result of our clockwise rotation of radar scanning angle  $\alpha$ .) We can now insert these Fourier estimates in the basic wind field relationships (1), (2), and (3), multiply all terms by  $r$ , and divide all terms by  $V_0$ , using  $b_1$  as an estimate for  $V_0$ , to obtain

$$a_0/b_1 = d + r/F, \quad (33)$$

$$-2a_2/b_1 = d - r/F, \quad \text{and} \quad (34)$$

$$2b_2/b_1 = r/R + c. \quad (35)$$

The final step in testing is a comparison of the left sides of (33) to (35), obtained by Fourier analysis of (29), with the appropriate combinations of the arbitrarily selected true values of wind field parameters on the right sides. Results of testing over a wide universe of parameter values ( $-0.1 \leq c \leq 0.4$ ,  $-0.3 \leq d \leq 0.1$ ,  $-0.1 \leq r/F \leq 0.3$ , and  $0 \leq r/R \leq 0.8$ ) indicated errors of less than 5% for  $r/R = 0.6$  or less and for  $r/F$  and  $d$  of opposite sign. Moreover, the validity of the approximation (29) was verified, even for  $r/R$  as large as 0.8, by continuity of the calculated Fourier coefficients  $b_1$  and  $b_2$  for all concurrent values of  $r/F$ , including  $r/F = 0$  for which an exact formulation (30) of  $V_D(\alpha)$  is applicable. Consequently, we have demonstrated that the technique of Browning and Wexler may be used for suitably accurate kinematic analysis of the wind field around a cyclone in which the magnitude of curvature varies inversely with distance from the center of curvature.

Results from testing our model indicate that, whenever variable curvature and/or variable diffluence are

present, the Fourier coefficients are underestimated. These errors tend to cancel in the ratio of coefficients on the left sides of (33) to (35). However, wind speed, as estimated by  $b_1$ , may be greatly underestimated: by 20 percent or more, for example, with  $r/R = 0.8$ . On the other hand, the mean magnitude of the two extrema of Doppler velocity  $V_m = [V_D(\max) - V_D(\min)]/2$  usually considerably overestimates wind speed in the presence of variable curvature and/or variable diffluence. Consequently, it was found empirically that the best estimate of wind speed is  $(b_1 V_m)^{1/2}$ . Within our universe of parameter value calculations,  $(b_1 V_m)^{1/2}$  averaged only 1% high, and all of the  $(b_1 V_m)^{1/2}$  values were in error by less than 5%.

### 5. Application to hurricane diagnosis

The techniques developed in the foregoing discussion are well adapted for estimation of the wind field derivatives in hurricanes, and may aid in detection of changes in hurricane intensity before evidence of such trends becomes apparent through local wind speed measurements. In application of this goal, the coordinate axes are aligned with the observed wind direction so that  $\alpha = 90^\circ$  is mean downwind, and the Fourier harmonics are calculated and entered in (33), (34), and (35). The sum and difference of (33) and (34) provide Fourier estimates of the parameters of downwind shear and diffluence. Accordingly,

$$d = (a_0 - 2a_2)/2b_1, \quad \text{and} \quad (36)$$

$$r/F = (a_0 + 2a_2)/2b_1. \quad (37)$$

Care must be taken, of course, to minimize observational errors, following the recommendations of Browning and Wexler (1968).

Unfortunately, there is no straightforward method for apportionment of the parameters of curvature and crosswind shear from their sum in (35). However, if we make the simple assumption that curvature of the wind field is inversely proportional to distance from a circulation center (for example, a hurricane eye), and if this distance  $R$  can be estimated reasonably well, we can solve (35) for  $\tilde{c}$ , defined as the parameter of *normative crosswind shear* that is required under this assumption as a contribution to the measured shearing deformation. The distance  $R$  from radar to circulation center is generally available for hurricanes, because the eye locations of threatening hurricanes are usually monitored at frequent intervals by aircraft and/or satellite. Therefore,

$$\tilde{c} = 2b_2/b_1 - r/R. \quad (38)$$

The normative crosswind shear is obtained by multiplying its parameter in (38) by  $V_0$ , the wind speed at the radar, and dividing by  $r$ , the radius of the VAD scanning circle. Accordingly, normative crosswind shear is



$$\partial V_0/r = (2b_1/b_2 + r/R)(V_m)^{1/2}/r, \quad (39)$$

using  $(b_1 V_m)^{1/2}$  as the best available estimate for  $V_0$ , where  $V_m = [V_L(\text{max}) - V_L(\text{min})]/2$ . In cyclonic storms, wherein curvature normally increases with decreasing distance to circulation center, the normative crosswind shear accounts for this increase and therefore is not subject to the dependence of the shearing deformation on the varying contribution of curvature owing solely to distance from radar to circulation center.

Ruggiero and Donaldson (1987) examined the trend of wind field derivatives in Hurricane Gloria during its 1985 journey across New England, using measurements recorded by the AFGL radar at Sudbury, MA. The radius of the VAD circle was 40 km, with elevation angle  $1.0^\circ$  and height above radar 800 m. Their most interesting result, depicted in Fig. 5, was a comparison of normative crosswind shear with wind speed at the radar.

Before landfall of Hurricane Gloria its maximum reported wind speed was  $65 \text{ m s}^{-1}$ , and warnings were issued about the devastation that could be inflicted if winds of such speed reached land. Fortunately, the hurricane had weakened by the time of landfall. Figure 5 shows that normative crosswind shear was observed to be near zero at 1600 UTC when Gloria entered Long Island, and actually decreased during the next 3 h to less than  $-2 \times 10^{-4} \text{ s}^{-1}$  as the hurricane approached. This is a surprising result, because crosswind shear in a normal hurricane would be expected positive toward the ring of maximum velocity surrounding the eye. However, if circulation around the hurricane decayed and the actual curvature parameter was reduced on that account to values substantially below  $r/R$ , a small positive crosswind shear could still be maintained even with negative values of normative crosswind shear. Evidently this was the case in Hurricane Gloria's encounter with New England; after the eye region entered the unambiguous velocity range of the radar, no signature of rotation could be detected. Also, as distance from radar to the hurricane center decreased from 251 km to 103 km over a 3 h period, Fig. 5 indicates that wind speed at the radar increased by only 1 km, suggesting a positive crosswind shear but with much smaller magnitude than would be expected in a normal hurricane. During the final half hour of the VAD measurements, wind speed actually decreased slightly.

This analysis of Hurricane Gloria led Ruggiero and Donaldson (1987) to propose that the normative crosswind shear (39) might be experimentally applied as a Storm Strength Indicator, or SSI. For example, in a normally active hurricane with a maximum wind speed of  $65 \text{ m s}^{-1}$ , the wind speed would increase by at least 10 m s $^{-1}$  as distance toward the eye wall decreased by 100 km. If circulation around the normally active hurricane is weak, the curvature field with magnitude varying inversely with distance from circulation center, the normative SSI would be at least  $10^{-4} \text{ s}^{-1}$ . Therefore, a negative SSI of  $-2 \times 10^{-4} \text{ s}^{-1}$

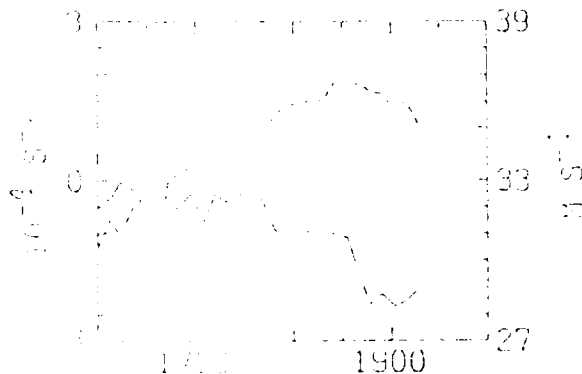


FIG. 5. Trend of wind speed (dashed curve, right-hand scale) and normative crosswind shear (solid curve, left-hand scale) at 800 m altitude in Hurricane Gloria (1985), derived from Doppler VAD measurements from AFGL radar at Sudbury, MA. Time scale along abscissa is in UTC. During these measurements the distance from radar to circulation center decreased from 251 km to 103 km (Adapted from Ruggiero and Donaldson 1987.)

suggest a storm of less than vigorous strength, and negative values of SSI probably indicate a decay of both circulation and wind speed. The example of Hurricane Gloria showed promise for forecasting the intensity of a storm advancing toward the radar. The measurement of SSI near zero at landfall, and trending negative thereafter, was confirmed by a negative trend in wind speed at the radar more than 2 h later.

In conclusion, the trend in Hurricane Gloria of the Storm Strength Indicator is an encouraging development for monitoring the intensity of circularly configured storms at distances remote from the radar site. This indicator may provide clues to the behavior of an advancing storm an hour or two before confirming information on wind speeds is measured at the radar. After the establishment of the NEXRAD system, this technique should be especially useful in assessing the threat to coastal areas by offshore hurricanes as well as intense extratropical storms.

#### a. Summary

The four first-order spatial derivatives of a wind field are divergence, convergence, downwind shear, and crosswind shear. In cyclonic flows, these derivatives are most conveniently expressed in natural coordinates referred to the circulation. Divergence, vorticity, stretching deformation, and shearing deformation are kinematic properties computed as sums and differences of pairs of first-order field derivatives; all of these properties can be calculated and synthesized by Fourier analysis of the Doppler velocity fraction measured by a radar scanning a cone of range in azimuth at constant range, followed by the Fourier analysis technique proposed by Bragg and Chisholm (1963). The recovery of each of these first-order derivatives when one or more of them are not directly measured is, however, not a straight-

forward proposition, and this question was explored in depth.

Simple models of each wind field derivative in turn were considered with a Doppler radar scanning in the VAD mode inserted into the wind field, in order to synthesize characteristic Doppler velocity functions of radar scanning angle. The models for curvature and diffluence do not have constant values throughout the wind field. Instead, the curvature is defined to be a variable, an inverse function of distance from a circulation center. A novel approach was used to model diffluence, by postulating a virtual (but fictitious) streamline apex. The synthesized Doppler velocity functions for each of the wind field derivatives reveal unique signatures for diffluence and downwind shear, but qualitatively similar signatures for curvature and crosswind shear.

For the natural, realistic situation wherein all four of the modeled wind field derivatives are present, an exact solution could not be found for the resultant Doppler velocity function. However, a suitable approximation was derived that reduced to an exact solution when either curvature or diffluence, or both, were eliminated. The validity of the approximation was tested over a wide-ranging set of parameter values of the four derivatives. For each set a Doppler velocity function was synthesized and then analyzed for the Fourier harmonics, which were then compared with the appropriate sums and differences of the derivatives. Results of the test showed that errors in recovery of the wind field derivatives were less than 5% except for unusual cases with diffluence and downwind shear not of opposite sign, or fairly high values of curvature for which distance from radar to center of curvature is less than twice the radius of the radar scanning circle. The test also revealed a substantial underestimate of wind speed by the magnitude of the first Fourier harmonic whenever diffluence and/or curvature were present. However, the square root of the product of this first harmonic and mean magnitude of the Doppler velocity extrema significantly reduced the error to a few percent. Consequently, there is confidence in most cases for the recovery from natural wind fields of downwind shear, diffluence, and the sum of curvature and crosswind shear, as well as wind speed.

A storm strength indicator (SSI), proposed earlier by Ruggiero and Donaldson (1987), is suggested as a promising index for remote and early detection of trends in hurricane intensity. In conditions suitable for Fourier analysis of the VAD pattern, the SSI is given by the shearing deformation minus an estimated curvature term that is inversely proportional to distance from radar to circulation center. During measurements conducted in New England in Hurricane Gloria (1985), the SSI showed decay after landfall of both circulation and wind speed toward the eye region an hour or two before confirmation by other, more direct radar measurements. This type of diagnosis, conducted at a radar

located on a coast, should be helpful in providing advance warning of the threat by destructive offshore cyclones.

**Acknowledgments.** We are pleased to take this opportunity to express our gratitude for the extensive assistance provided by our former colleague, Frank H. Ruggiero (now with AFGL). He programmed the Doppler velocity patterns for a wide variety of wind field models, provided Fourier analyses for these patterns, devised interpolative and averaging techniques for analysis of Doppler velocities in natural wind fields, and offered suggestions for the analysis of the Hurricane Gloria dataset. We are also grateful for data on this hurricane acquired by the AFGL Doppler radar at Sudbury, MA, under the direction of Kenneth M. Glover. A dedicated team of AFGL engineers and technicians deserve our highest appreciation for their successful round-the-clock efforts to complete major radar repairs in time to permit data acquisition in Hurricane Gloria. This team included Graham Armstrong, Alexander Bishop, T Sgt Richard Chanley, Edward Duquette, Douglas Forsyth (now at NSSL), 1st Lt Allan Sadoski and William Smith. We gratefully acknowledge the valuable criticisms and suggestions offered by a reviewer. Finally, we wish to thank Mrs. Sundie Meroth and L. A. McLaughlin for their careful efforts in preparing our manuscript. This work was supported under AFGL Contract F19628-82-C-0023.

#### REFERENCES

- Baynton, H. W., R. J. Serafin, C. L. Frush, G. R. Gray, P. V. Hobbs, R. A. Houze, Jr. and J. D. Locatelli, 1977: Real-time wind measurements in extra-tropical cyclones by means of Doppler radar. *J. Appl. Meteor.*, **16**, 1022-1028.
- Browning, K. A., and R. Wexler, 1968: The determination of kinematic properties of a wind field using Doppler radar. *J. Appl. Meteor.*, **7**, 105-113.
- Caton, P. G. F., 1963: Wind measurement by Doppler radar. *Meteor. Mag.*, **92**, 213-222.
- Donaldson, R. J., Jr., M. J. Kraus and R. J. Boucher, 1978: Doppler velocities in rain bands of Hurricane Belle. Preprints, *18th Conference on Radar Meteorology*, Atlanta, Amer. Meteor. Soc., 181-184.
- Donaldson, R. J., Jr., and F. I. Harris, 1984: Detection of wind field curvature and wind speed gradients by a single Doppler radar. Preprints, *22nd Conference on Radar Meteorology*, Zurich, Amer. Meteor. Soc., 514-519.
- Lhermitte, R. M., and D. Atlas, 1961: Precipitation motion by pulse Doppler. Proceedings, *Ninth Weather Radar Conference*, Kansas City, Amer. Meteor. Soc., 218-223.
- Passarelli, R. E., Jr., 1983: Wind field estimation by single Doppler radar techniques. Preprints, *21st Conference on Radar Meteorology*, Edmonton, Amer. Meteor. Soc., 526-529.
- Pettersen, S., 1956: *Weather Analysis and Forecasting*. Volume 1 2nd ed. McGraw-Hill, 428 pp.
- Probert-Jones, J. R., 1960: Meteorological use of pulsed Doppler radar. *Nature*, **186**, 271-273.
- Ruggiero, F. H., and R. J. Donaldson, Jr., 1987: Wind field derivatives: A new diagnostic tool for analysis of hurricanes by a single Doppler radar. Preprints, *17th Conference on Hurricanes and Tropical Meteorology*, Miami, Amer. Meteor. Soc., 178-181.
- Waldteufel, P., and H. Corbin, 1979: On the analysis of single-Doppler radar data. *J. Appl. Meteor.*, **18**, 532-542.

## POTENTIAL-VORTEX FIT

Philip J. Donaldson, 1989

ST Systems Corporation  
 Lexington, Massachusetts

### 1. INTRODUCTION

The estimation by single Doppler radar measurements of hazardous wind speeds in a hurricane may sometimes offer intractable difficulties. This task can best be accomplished if the hurricane eye is within the first unambiguous range interval (typically 115 km for the NEXRAD radars) and there is sufficient precipitation around the eye to provide tracers for the maximum velocities receding and approaching the radar. If the eye is located beyond the maximum unambiguous range it may be inaccessible to velocity measurement because it could be masked by much greater returned power from precipitation in the first trip, owing to the great extent of hurricane rain bands. If the radar has PRF flexibility, this situation may be alleviated somewhat by extending the maximum unambiguous range interval as far as necessary to include the hurricane eye region, as suggested by Harris et al. (1989). Baynton (1979) recommended an unambiguous range interval of 300 km for hurricane warnings. In an operational scenario, however, it is not clear at this time whether changing the PRF of the NEXRAD radars will be a viable option. Also, at great ranges resolution is impaired, and lower heights in the hurricane circulation are obstructed by the earth's curvature.

Regardless of the distance of the hurricane eye, it may be useful to acquire constant-height and constant-resolution samples in a limited area of the hurricane flow field from time to time. Accordingly, a simple technique is suggested, using the Browning and Wexler (1968) Fourier analysis scheme, to determine the extent to which a Doppler VAD (Velocity-Azimuth Display) pattern, measured entirely outside the radius of maximum wind speeds, fits a potential-vortex flow regime. In such a regime, curvature, as well as tangential speed of the wind, is inversely proportional to distance from a circulation center.

Despite known and suspected deviations from strict circular symmetry, it has been operationally useful to characterize the horizontal flow in mesocyclones as a Rankine combined vortex (Burgess et al., 1979), with an inner core in solid rotation surrounded by a potential-vortex annulus merging at a distant outer radius into the ambient environmental flow. As a working hypothesis, it is postulated that the tangential wind field around the most intense hurricanes and typhoons in their most active stage may also be approximated by a Rankine combined vortex. It is also postulated that the winds within a VAD circle may provide adequately representative samples of the considerably larger areal extent of the hurricane circulation.

### 2. SIMPLISTIC FORMULATION OF POTENTIAL-VORTEX FIT

Vorticity is curvature minus crosswind shear (considered to be positive toward the left of the wind vector). In the potential-vortex flow regime vorticity is zero, because at any given point in this regime the curvature and crosswind shear are of the same magnitude and sign. The shearing deformation is equal to the sum of curvature and crosswind shear, or to twice the curvature in potential-vortex flow wherein curvature and crosswind shear are equal. The shearing deformation in cyclonic flow may be estimated with reasonable accuracy, according to Donaldson and Harris (1988), by calculation of the second harmonic of the Doppler radar VAD pattern, as proposed by Browning and Wexler (1968). The first harmonic gives wind speed, also to reasonable accuracy in cyclonic flow. The curvature term may be estimated by distance  $R$  from radar to circulation center, given by outside information on location of the hurricane eye from aircraft, satellite, or conventional radar.

Initially we consider a simplified but unrealistic cyclonic circulation that is exclusively tangential, with no radial component toward the circulation center and no translational motion of the circulation field. We shall calculate a ratio hereby named Potential-Vortex Fit, or PVF, equal to the quotient of calculated shearing deformation divided by twice the estimated curvature term. If we align the coordinate axes of the VAD circle of radius  $r$  such that  $\alpha = 0^\circ$  is the azimuth of the circulation center at distance  $R$  from the radar, with  $\alpha$  increasing clockwise, then the tangential wind at the radar site is directed along azimuth  $\alpha = 90^\circ$ . With no radial or translational wind components,  $b_1$  (the first-order Fourier coefficient with argument  $\sin \alpha$ ) is tangential wind speed, and  $b_2$  (the second-order coefficient with argument  $\sin 2\alpha$ ) is half the shearing deformation multiplied by  $r$ . Consequently, shearing deformation is calculated to be  $2b_2/r$ , the curvature term is estimated as  $b_1/R$ , and we evaluate PVF as  $(2b_2/r)/(2b_1/R)$ , or

$$PVF = \frac{1}{2} R b_2 / r b_1 \quad (1)$$

A value of  $PVF = 1$  indicates that, within the VAD scanning region, the wind field of the cyclone is in a potential-vortex flow regime, and the tangential component of wind speed is likely to double at half the distance to circulation center. Values of PVF appreciably above unity would be anomalous and might indicate a local wind anomaly within the VAD circle, rather than a representative sample of the hurricane. A persistence check might be the key to discovering the size of the anomaly as it flows through the area scanned by the radar.

On the other hand, persistent values of PVF appreciably less than unity probably indicate decay of the hurricane or cyclone circulation. With zero crosswind shear but curvature still inversely proportional to distance from circulation center, the calculated value of PVF would be 0.5. Therefore persistent values of PVF below 0.5 would indicate diminished wind speeds toward the hurricane center and/or breakdown of circulation. Figure 1 depicts profiles of tangential wind speed for several contrasting PVF values, assuming that curvature remains inversely proportional to distance from the circulation center.

### 3. A MORE REALISTIC CALCULATION OF POTENTIAL VORTEX FIT

In the real world hurricanes and other cyclones generally move across the landscape (or seascape), and their circulation normally is comprised of radial as well as tangential components. Potential-Vortex Fit is a concept applicable only to tangential velocities, so the effects of translational and radial components must be removed from the total wind vector prior to calculation of PVF.

The wind field measured by the VAD technique is resolved by Fourier analysis into a radial component  $a'_1$  directed toward the circulation center of the cyclone, and a tangential component  $b'_1$  normal to  $a'_1$ . The primes indicate that components of storm translational velocity  $V_s$  contribute to the total wind,  $V_m$ , measured by radar. Figure 2 shows the relationship of these wind vectors and their components. The radial component  $a'_1$  is the first-order Fourier coefficient with argument  $\cos \alpha$  of the VAD function, with  $\alpha = 0^\circ$  toward the circulation center and  $\alpha$  increasing clockwise. The angles  $\alpha_m$  and  $\alpha_s$  are the directions of  $V_m$  and  $V_s$ , respectively, clockwise from  $\alpha = 0^\circ$ .

The tangential speed,  $b_1$ , of the cyclone circulation is the tangential component of measured velocity minus this same component of storm translational velocity:

$$b_1 = b'_1 - V_s \sin \alpha_s. \quad (2)$$

Similarly, the radial speed of the circulation is given by:

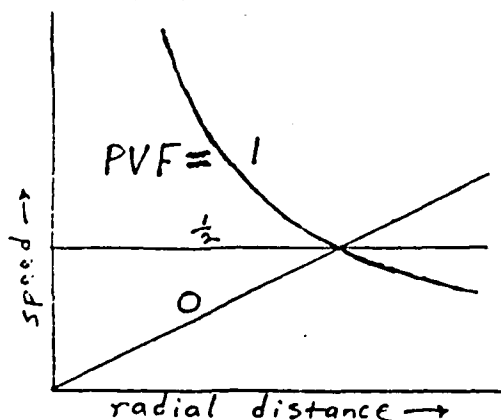


Figure 1: Radial profiles of tangential wind speed for a range of PVF values, assuming inverse proportionality of curvature with radial distance.

$$a_1 = a'_1 - V_s \cos \alpha_s. \quad (3)$$

Translational speed ( $V_s$ ) and direction ( $\alpha_s$ ) are estimated by motion of the eye of the storm. The magnitude ( $V_m$ ) and direction ( $\alpha_m$ ) of the total wind measured by radar are easily calculable from  $a'_1$  and  $b'_1$ .

Do the translational and radial components affect the shearing deformation of the tangential wind? We think not. Storm translation is considered to be uniform throughout the storm, and therefore has no spatial derivative. On the other hand, a radial velocity field accompanying a curved tangential field is certainly deformed by its confluent flow toward the circulation center, combined with any change of speed toward the eye wall. These derivatives of the radial field, however, contribute to stretching deformation, and have no effect on the tangential shearing deformation.

Consequently, Potential-Vortex Fit, expressed in directly observable terms in the presence of storm translational motion, is:

$$PVF = b_1 r / (b'_1 - V_s \sin \alpha_s). \quad (4)$$

### 4. RESULTS FROM HURRICANE GLORIA (1985)

Hurricane Gloria was observed for more than nine hours on September 27, 1985 by the AFGL Doppler radar located at Sudbury, Massachusetts. However, there was sufficient precipitation around the radar to enable high-quality VAD measurements for only a little more than three hours. The best data, with most complete coverage of the VAD circle, were found at the lowest elevation angle of  $1.0^\circ$ , and these were selected for calculation of PVF. The VAD radius,  $r$ , was 40 km, assuring freedom from contamination by ground clutter. This radius at  $1.0^\circ$  elevation fixed the VAD circle at a height of 900 m above sea level. The location of the hurricane eye was monitored in real time for most of the observational period, and its position was refined by post-analysis. Storm translational velocity was estimated by tracking its center, which moved toward geographical azimuth  $011^\circ$  to  $024^\circ$  at a speed of 18 to 14 m/s during the VAD observational period.

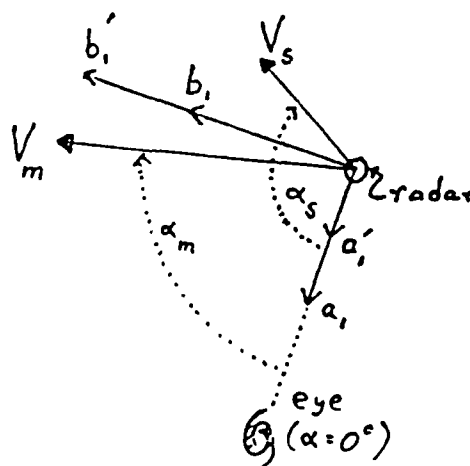


Figure 2: Vectors contributing to radial and tangential components of cyclone circulation. See text for discussion.

The PVF calculations started at 1559 UTC, very near the time of first landfall of the circulation center of Hurricane Gloria on the southern coast of Long Island, at a distance of 261 km from the radar. At 1916 UTC, when the PVF calculations terminated, the pressure center was 103 km distant, near Springfield, Massachusetts. The largest calculated values of PVF were 0.45, observed several minutes after second landfall on the Connecticut coast, and 0.44 at the time of first landfall. The lowest value of -0.02 was observed nearly three hours after first landfall, as the tattered remains of Gloria's eye was entering central Massachusetts.

Individual observations may not be representative samples of the hurricane structure, because there is always the likelihood that particular measurements of shearing deformation and wind speed could be contaminated by small-scale wind field anomalies along the VAD scanning circle. However, trends in PVF would certainly be revealed by averaging over a persistence time sufficient for small-scale features to transit the VAD circle. Accordingly, this persistence time for the hurricane Gloria observations is defined as the diameter of the VAD circle (80 km) divided by total wind speed at the radar (varying from 31 to 37 m/s), yielding 36 to 43 minutes. The observations, then, may be divided into five independent time periods, with average values listed in Table 1:

Time Period	PVF	$b_1$	R
1559-1636 UTC	0.284	23.1 m/s	244 km
1643-1719	0.326	24.4	205
1727-1756	0.304	25.3	172
1803-1833	0.152	25.7	144
1840-1916	0.142	23.1	118

Table 1: Average values, over indicated time periods, of PVF, tangential speed ( $b_1$ ) and distance from radar to circulation center (R) of Hurricane Gloria (1985).

The trends of the tabulated values are depicted in more detail in Fig. 3, which shows running means of five consecutive observations (a period of 30 minutes) of PVF and tangential wind speed. It is interesting to see that the peak value of PVF occurred about 40 minutes before tangential wind speed reached its maximum.

Earlier in its lifetime Hurricane Gloria had been considered an extremely dangerous storm. A couple of days before landfall, when Gloria was still over warm tropical waters, its maximum wind speed was estimated to be 65 m/s. However, the hurricane lost considerable energy as it traversed progressively cooler waters off the mid-Atlantic coast. Peak gusts at Islip, Long Island, for example, were only 38 m/s. The remarkably low values of PVF measured during the entire observational period are consistent with continued decay of circulation as Gloria moved overland.

The small but persistent increase in tangential wind speed during the first two hours of observation, as the hurricane approached, suggests a small positive value of crosswind shear. If this were true, and if wind field curvature were still inversely proportional to distance from radar to hurricane center, the values of PVF during these hours should be slightly greater than 0.5. However, all PVF values are notably less than 0.5, indicating a curvature function less than expected from inverse proportionality. During the final hour the very low values (under 0.2) for PVF and decreasing tangential speeds strongly suggest a marked breakdown in cyclonic circulation. This suggestion was confirmed when the pressure center of the hurricane entered the unambiguous range interval of the radar at 1851 UTC, and the center could be observed clearly. From this time onward no vortex signature nor any other indication of rotation was evident. Consequently, the observations of PVF in Hurricane Gloria appear to be a reliable indicator of the later stages of its progressive structural breakdown following landfall.

##### 5. SYSTEMATIC ERRORS

The coefficients  $b_1$  and especially  $b_2$  in the Fourier analysis of the VAD pattern are generally underestimated when the curvature of the wind field is inversely proportional to distance from a circulation center. What helps to save the day is the use of the ratio of  $b_2/b_1$  in the expression for PVF, so the resultant error is not as serious as the underestimate of  $b_2$  alone. The error also increases as  $r/R$  increases. For example, in a wind field with an inversely proportional curvature function but constant wind speed,  $b_2/b_1$  is underestimated by 20% for  $r/R = 1$ , by 10% for  $r/R = 0.8$ , but only by 3.4% for  $r/R = 0.5$ . Observations of PVF in Hurricane Gloria involved  $r/R$  ratios from 0.13 to 0.37. The  $r/R$  ratio is under control of the radar operator and seldom need be greater than 0.5, so the error from this source is quite acceptable.

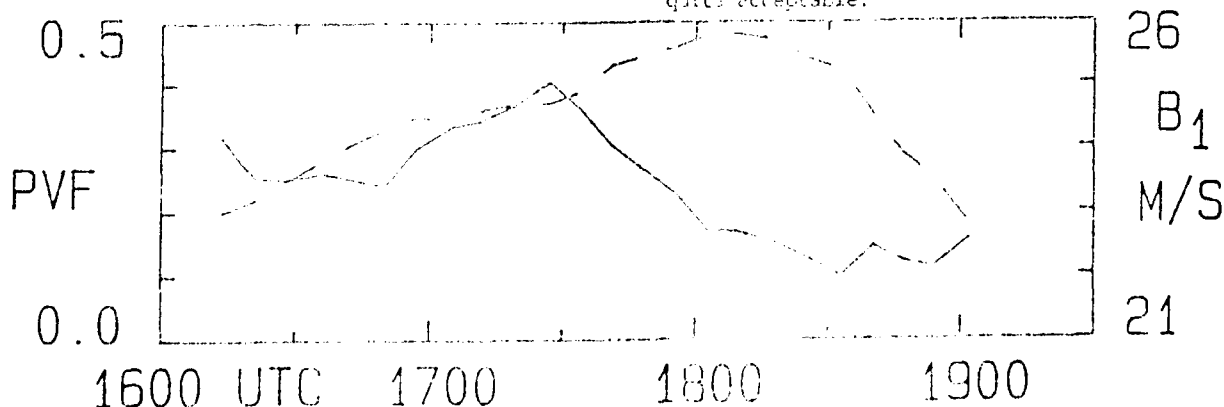


Figure 3: Time evolution of Potential Vorticity (solid line) and tangential wind speed (dashed line) in Hurricane Gloria.

An additional error could arise if the solidly-rotating hurricane core is much larger than expected and part of the VAD scan crosses into this region of diminished velocity. With  $r/R = 0.5$  and a  $90^\circ$  sector of the VAD scan sampling the core, the underestimate of  $b_2/b_1$  would range from 6% to 15%, depending on the velocity distribution outside the core. Errors would be less with smaller core-intersecting sectors and lower values of  $r/R$ . It may be difficult to determine whether the VAD circle and hurricane core of solid rotation intersect. However, if a  $90^\circ$  sector of the VAD circle intersects the hurricane core with  $r/R = 0.5$ , the core radius would need to be  $1.5r$ . This is not expected to occur frequently with the usual values selected for  $r$ , such as 40 km for the observation of Hurricane Gloria.

Location of the hurricane circulation center may be troublesome, especially during the decaying stages. Uncertainty in eye position will contribute an unknown error to storm translational speed ( $V_s$ ) and direction ( $\alpha_s$ ) as well as distance ( $R$ ) from radar to the circulation center. Another unknown error may arise from asymmetries in the circulation pattern. Finally, the small size of the VAD scanning circle relative to the total area of the hurricane raises the question of representativeness of the PVF calculations. This technique provided a useful diagnosis of Hurricane Gloria during the decay of its circulation, but confidence in PVF will require successful diagnosis of many more storms.

#### 6. RELATIONSHIP OF PVF TO STORM STRENGTH INDEX

Ruggiero and Donaldson (1987) proposed a storm strength index, or SSI, as a diagnostic tool for estimating hurricane intensity, using radar data remote from the hurricane eye. In its quantitative form, the SSI is evaluated by subtraction of the estimated curvature term (under the assumption that curvature varies inversely with distance  $R$  from hurricane center), from shearing deformation calculated around a VAD circle of radius  $r$ . Accordingly,

$$SSI = 2b_2/r - b_1/R. \quad (5)$$

The dimension of SSI is in  $s^{-1}$ , and can be regarded as a normative crosswind shear that would be required as a contribution to the observed shearing deformation in a storm with approximately circular streamlines around its center. The same calculations and assumption are used to formulate SSI and PVF, and so these two indices are related.

Multiplication of SSI by  $r/b_1$  yields a dimensionless parameter of normative crosswind shear, designated as  $\bar{c}$  by Donaldson and Harris (1988):

$$\bar{c} = 2b_2/b_1 - r/R. \quad (6)$$

Manipulation of equations (1) and (6) leads to an expression relating  $\bar{c}$  to PVF:

$$\bar{c} = (r/R)(2PVF - 1). \quad (7)$$

This can also be stated independently of the estimated curvature if the first- and second-order Fourier coefficients are involved:

$$\bar{c} = (b_2/b_1)(2 - 1/PVF). \quad (8)$$

Thus, for  $PVF = 1$ , as in a regime of potential-vortex flow,  $\bar{c} = r/R$  and also  $\bar{c} = b_2/b_1$ . At the other extreme, in solid rotation  $\bar{c} = -r/R$ , resulting in  $PVF = 0$ , which also requires zero shearing deformation. In the interesting case of  $PVF = 0.5$ ,  $\bar{c} = 0 = SSI$ ; and from equation (5) this condition requires equality of shearing deformation with estimated curvature.

Both these two indices, PVF and  $\bar{c}$ , would seem to be useful for assessment of hurricanes and large circularly-configured cyclones, especially when the eye region is beyond the first Doppler trip. The ratio PVF estimates the approach to Rankine normality of the cyclone circulation, as sampled throughout the circumference of the VAD scan. It can be regarded as an indicator of circulation vitality. The parameter  $\bar{c}$ , for a given PVF, will vary inversely with  $R$  (see equation 7) and on this account is not as representative as PVF throughout the cyclone. However,  $SSI = \bar{c}b_1/r$  is a convenient index for direct estimation of wind speeds toward the cyclone center, provided the assumed curvature function seems reasonable.

#### ACKNOWLEDGMENTS

I am very happy for this opportunity to express my gratitude to Frank Ruggiero of AFGL for his creative and effective programming of the computations required for analysis of the Hurricane Gloria data set, and to Ian Harris of STX for his encouragement and helpful suggestions. This work was supported under AFGL Contract F19628-87-C-0124.

#### REFERENCES

- Baynton, H. W., 1979: The case for Doppler radars along our hurricane affected coasts. *Bull. Amer. Meteor. Soc.*, **60**, 1014-1023.
- Browning, K. A. and R. Wexler, 1968: The determination of kinematic properties of a wind field using Doppler radar. *J. Appl. Meteor.*, **7**, 105-113.
- Burgess, D. W. and JDOP Staff, 1979: Final Report on the Joint Doppler Operational Project (JDOP) 1976-1978. NOAA Tech. Memo., ERL NSSL-86, 84 pp.
- Donaldson, R. J., Jr. and F. I. Harris, 1988: Estimation by Doppler radar of curvature, diffluence, and shear in cyclonic flow. *J. Atmos. Oceanic Technol.* (in press).
- Harris, F. I., D. J. Hamann, and R. J. Donaldson, Jr., 1989: Hurricane monitoring with Doppler radar: a simulation. This volume.
- Ruggiero, F. H. and R. J. Donaldson, Jr., 1987: Wind field derivatives: a new diagnostic tool for analysis of hurricanes by a single Doppler radar. Preprints, 17th Conf. on Hurricanes and Tropical Meteorology (Miami), AMS, Boston, MA, 178-181.

## Hurricane Monitoring with Doppler Radar: A Simulation\*

F. Ian Harris, Donald J. Hamann and Ralph J. Donaldson, Jr.

ST Systems Corporation (STX)  
109 Massachusetts Ave.  
Lexington, MA 02173

### 1.0 INTRODUCTION

With the imminent deployment of the NEXRAD network, the potential for routinely observing synoptic scale storms with Doppler radar is soon to be realized. Some of these large scale storms can have devastating wind conditions resulting in loss of life and property. Atlantic hurricanes, Pacific typhoons, and intense winter oceanic cyclones are notable examples of this type of storm. However, to date, observations of hurricanes and other large systems by ground-based Doppler radar have been extremely limited, making any useful algorithm development difficult and subsequent verification virtually impossible.

On September 27, 1985, data were collected from Hurricane Gloria by the Air Force Geophysics Laboratory Doppler radar located in Sudbury, MA. Analysis of these data has resulted in the development of techniques to assess the characteristics of these storms (Donaldson and Harris, 1988; Donaldson and Ruggiero, 1986; Ruggiero and Donaldson, 1987). At the time of first observation Gloria was dying, having just entered the south coast of Long Island. As a result, this data set is very limited and any analysis techniques developed from this storm must undergo much further testing to assess generality of the results.

Because of the lack of good observations from which to develop and test hurricane diagnostic algorithms, Wood and Brown (1987) of the National Severe Storms Laboratory constructed synthetic wind fields derived from an analytical model based somewhat on aircraft and land-based conventional radar observations. They have further taken these wind fields and derived Doppler radar radial velocity fields. We have acquired both the synthetic wind fields and the derived Doppler fields for this study.

The beauty of using synthetic data is the ability to test sensitivity of results to a variety of storm and sampling parameters. We are able to move the storm around the radar, place it at far and near ranges, and adjust such radar sampling parameters as pulse repetition frequency (PRF) and azimuthal and radial data resolution. The disadvantage is that we are not dealing with real data with all the inherent problems associated with uncertainty of estimates, the influence of ground clutter, the presence of smaller scale but real perturbations, the effects of sidelobes, etc. While these introduce complicating factors, there is still a value to performing evaluations in a controlled environment. If techniques do not work under these artificial conditions, they will never work in the real world.

In this paper, we establish the methodology for the use of synthetic data as an evaluation tool. Initial evaluations of some of the parameters derived from earlier studies of Hurricane Gloria will be discussed. However, the scope of this paper must be considered as preliminary at the time of this writing.

### 2.0 DIAGNOSTIC PARAMETERS

From the Hurricane Gloria studies, several useful parameters describing the wind field were derived, all based on detailed analyses of the Velocity Azimuth Display (VAD) of the data. From these wind field derivatives, three storm behavior indicators have been derived (Donaldson and Harris, 1984; Ruggiero and Donaldson, 1987; and Donaldson, 1989). Table I lists these parameters and their definitions. Table II defines terms, and their definitions, used in Table I. The parameters  $a_0$ ,  $a_1$ ,  $a_2$ ,  $b_1$ , and  $b_2$  are the coefficients of the Fourier components contained in the expression:

$$V_r = a_0 + a_1 \cos(\theta) + b_1 \sin(\theta) + a_2 \cos(2\theta) + b_2 \sin(2\theta) \quad (1)$$

where  $V_r$  is Doppler radial velocity and  $\theta$

\* This work was supported under AFGL Contract No. F19628-87-C-9124.

TABLE I

Windfield Derivatives and Storm Behavior Indicators Calculable from Single Doppler Radar Data.

PARAMETER	SYMBOL	FORMULATION
<u>Windfield Derivatives</u>		
Normative cross-wind shear	$S_c$	$2b_z/r - b_1/R$
Downwind shear	$S_D$	$(a_0 - 2a_z)/2r$
Diffluence	$D$	$(a_0 + 2a_z)/2r$
<u>Storm Behavior Indicators</u>		
Cyclonic Intensity Indicator	CII	$\sin(\delta) V_0/r$
Storm Strength Indicator	SSI	$2b_z/r - b_1/R$
Potential Vortex Fit	PVF	$\frac{b_z R/r}{b_1' - V_0 \sin(\alpha_0)}$

is azimuth angle measured clockwise from some reference direction, taken to be along the line from the radar to the center of the storm. This angle results in  $a_1$  being an estimate of the radial component and  $b_1$ , the tangential component of the wind.

The wind field derivatives in Table I differ from the terms usually used to describe wind fields, namely divergence, shearing and stretching deformation, and vorticity. However, this derivative set and that in Table I are related. Downwind shear ( $S_D$ ) and diffuence ( $D$ ) are calculated from sums and differences of divergence ( $a_0/r$ ) and stretching deformation ( $-2a_z/r$ ). Curvature and crosswind shear are similarly related to shearing deformation ( $2b_z/r$ ) and vorticity (incalculable from VAD analysis). Consequently calculations of downwind shear and diffuence are straightforward, as expressed in Table I, while that of crosswind shear is not. However, this latter term can be estimated as a normative value by adopting a reasonable assumption of inverse proportionality for curvature ( $b_1/R$ ) and subtracting this from shearing deformation. This results in the estimate of crosswind shear,  $S_c$ , as given in Table I, which is also identical to SSI, the Storm Strength Indicator proposed by Ruggiero and Donaldson (1987). The  $b_1'$  term in the PVF definition refers to the estimate of  $b_1$  in the presence of a storm translational velocity. See Donaldson (1989) for further discussion.

Computations are made by first taking a set of radial velocities around a 360° circle and performing a fit in a least-squares sense of Eqn. 1 to them.

Table II

Definitions of Terms Used in Table I.

PARAMETER	DEFINITION
$a_0, b_1$ , etc	Coefficients from Eqn 1.
$r$	Radius of the VAD circle
$R$	Distance from radar to center of curvature (storm center)
$\delta$	The mean angular deviation of the maximum and minimum Doppler velocities from diametric opposition
$V_m$	$(V_{max} - V_{min})/2$
$V_0$	$(b_1 V_m)^{1/2}$
$V_0$	Storm advection speed
$\alpha_0$	Storm advection direction

From the coefficients for this least-squares curve and the parameters in Table II, the derivatives and indicators listed in Table I are then computed.

### 3.0 MODEL DATA

The Wood and Brown (1987) model, herein to be referred to as the WB model, is a simple, quasi-axisymmetric circulation occupying a domain extending in the vertical from the surface to a height of 14 km and in the horizontal 300 km in both directions. Both velocity and reflectivity factor fields are specified by the WB model, although the latter has not yet been used in this study. The storm is moving northward at 5 m/s and has a ring of maximum winds about 28 km from the storm center, with the strongest winds (about 55 m/s) located in the forward right quadrant. This ring slopes outward in the vertical and has an associated zone of convergence in the low levels and a divergence region aloft, along with an updraft core throughout the depth of the storm. The velocity structure in the horizontal is very much like a Rankine - combined vortex, a common velocity model for mesocyclones in severe thunderstorms. Of course, the hurricane circulation is on a much larger scale than that of the mesocyclone.

### 4.0 ANALYSIS PROCEDURES

For this study, we have made our own calculations of Doppler radial velocity as a function of range from the radar and azimuth and elevation angle of the beam. The starting fields are the output Cartesian velocity component fields from the WB model. This allows us versatility in terms of placement of the storm relative to the radar and in the specification of the radar sampling parameters. Only one storm "snapshot" was used for this study.



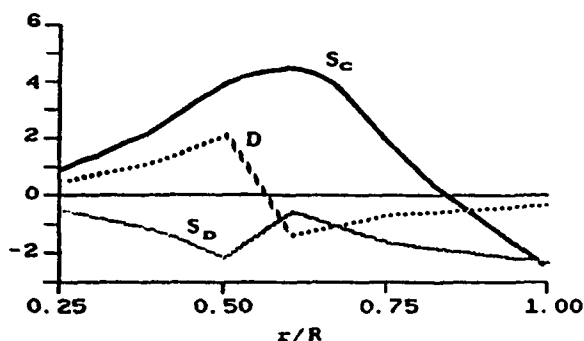


FIG. 1 Plot of Windfield Derivatives ( $S_c$ ,  $S_d$ , and  $D$ ) against  $r/R$ .  $r = 30$  km. Ordinate units are  $10^{-4} s^{-1}$  for  $S_d$  and  $D$  and  $10^{-4} s^{-1}$  for  $S_c$ .

Once the Doppler radial velocity fields are obtained, least-squares fits of Eqn 1 to the data are calculated at selected ranges. The Fourier coefficients are computed relative to the radar-storm axis line and then used to evaluate the parameters in Table I.

## 5.0 EFFECTS OF STORM LOCATION

### 5.1 Range Dependency

The storm was moved from south to north toward the radar in 10 km intervals with the radius  $r$  of the VAD circle fixed at 30 km. The wind field derivatives ( $S_c$ ,  $S_d$  and  $D$ ) are plotted in Fig. 1 versus the normalized range  $r/R$ . All three curves demonstrate considerable dependency upon  $r/R$ . At  $r/R = 1$  the radar is scanning through the center or eye of the storm and as the ratio decreases, the scan circle recedes from that center. There are two extreme points in the  $S_d$  and  $D$  curves: one at  $r/R$  of about 0.5 and one at about 0.6. It should be noted that the locations of these extrema cannot be considered to be precise in light of the coarseness of the  $r/R$  resolution used. However, the first extreme appears to correspond quite closely to the radius of maximum winds that occur around the storm eye. Outside of this radius (i.e. for  $r/R < 0.5$ ), both of the shears and the diffluence decrease as  $r/R$  decreases toward the value of

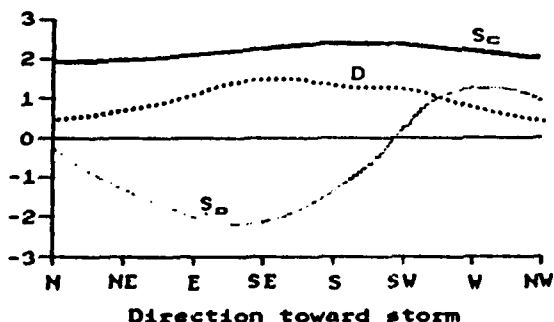


FIG. 3 Plot of Windfield Derivatives against Compass Points. Units of ordinate as in Fig. 1.

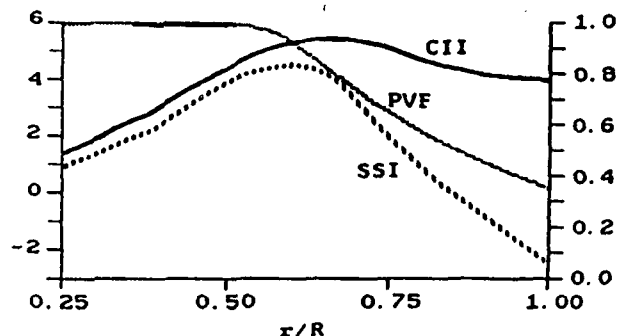


FIG. 2 Plot of Storm Behavior Indicators ( $CII$ ,  $SSI$ , and  $PVF$ ) against  $r/R$ . Units of left ordinate are  $10^{-4} s^{-1}$  for  $CII$  and  $SSI$  and of right ordinate, unity for  $PVF$ .

0.25, the minimum used in these calculations. For measurements collected within the hurricane periphery, we would expect the shears and diffluence to continue to approach zero with further reduction of  $r/R$ . On the other hand, within the radius of maximum wind ( $r/R > 0.5$ ) the expected behavior of these curves is harder to assess and explanations await further analysis.

In the plot of the storm behavior indicators in Fig. 2 we see less variability than in the windfield derivatives of Fig. 1. For  $r/R < 0.5$ ,  $PVF$  values are virtually invariant from 1, indicating perfect potential vortex flow. That we get such a value should not be surprising since the WB model has been designed such that this portion of the field resembles potential vortex flow. The  $SSI$  and  $CII$  each have a maximum at about  $r/R = 0.6$ , corresponding to the inner extrema seen in the curves of Fig. 1.

Some care must be taken at this point against placing too much emphasis on the significance of  $r/R$  of 0.5 and 0.6. If the first ratio is tied to the diameter of the ring of maximum winds, as is suggested above, then one might expect that if the ring diameter changes so would the  $r/R$  value for the peaks. However, this requires further investigation.

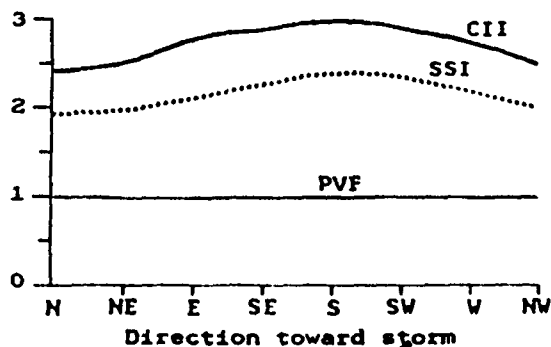


FIG. 4 Plot of Storm Behavior Indicators against Compass Points. Units of ordinates as in Fig. 2.

TABLE III

Long Range Computations. Locations and magnitudes of detected velocity extrema and detected diameter of ring of maximum winds. Elevation angle =  $0.5^\circ$ . Data resolution: range - 450 m; azimuth -  $0.5^\circ$ .

R (km)	$V_{max}$		$V_{min}$		Range (km)	Height (km)	Diameter (km)
	Magnitude (m/s)	Azimuth (deg)	Magnitude (m/s)	Azimuth (deg)			
250	41.5	187.0	-41.6	173.0	243.9	5.6	59.4
300	38.7	186.0	-39.0	174.0	289.4	7.5	60.5
350	31.2	185.5	-31.5	174.5	339.8	9.8	65.1
400	14.5	184.5	-19.8	175.5	383.0	12.0	60.1

## 5.2 Angular Dependency

In this study, the storm was moved around the radar, maintaining  $R = 75$  km. All analyses were performed at a VAD radius of  $r = 30$  km, yielding  $r/R = 0.40$ , outside the ring of maximum winds. In Fig. 3 the windfield derivatives are plotted as a function of direction expressed as compass points. The curve for downwind shear ( $S_D$ ) is the most variable of these parameters and appears to reflect the fact that the velocity field is not totally symmetric, but is at least symmetric about a WNW - ESE line. Both diffluence and normative crosswind shear are less directionally dependent.

The three storm behavior indicators plotted in Fig. 4 do not demonstrate a strong viewing angle dependency. This is particularly true of PVF. It remains relatively invariant at a value of  $1.0 \pm 0.01$ . This lack of viewing angle dependency will make these parameters much easier to interpret in terms of storm behavior. However, care must be taken in extrapolating these results to real situations where the storms may not be as symmetric.

## 6.0 IMPLICATIONS OF LONG RANGE VIEWING

With hurricanes it would be highly desirable to be able to make measurements when the storm is still at relatively far range. There are several factors that must be considered when assessing the utility of Doppler radar for such a task. These include:

- Compromises in range and velocity aliasing
- Beam filtering
- Azimuthal resolution
- Beam height versus storm height

We have made only a very preliminary examination of some of these factors. In particular, we assume that we have a very long wavelength and low PRF radar that has no problems with range and velocity aliasing. The storm is then moved outward from the radar to distances from 250 to 400 km and the peak velocities and their locations are examined (Table III). From these data, it would appear that the radar could detect the core couplet to 350 km. Beyond that range, problems arise primarily because the beam is so

high in the storm that it is above the more active portion of the circulation.

Beam filtering causes the underestimation of the amplitudes of perturbations with scales comparable to and less than the beam dimensions. At the ranges considered here, the ratio of the diameter of a  $1^\circ$  beam to the radius of the hurricane ring of maximum winds is at most 0.2. For that ratio, Brown and Lemon (1976) indicate about a 5% underestimate of the peak velocities, quite tolerable for most situations.

## 7.0 CONCLUSIONS

A preliminary study of the effectiveness of hurricane monitoring parameters has been presented. From the results to date it would appear that the windfield derivatives (diffluence and downwind and crosswind shear) may hold clues to the internal wind structure of the storm. On the other hand, of storm behavior indicators, the PVF is the least sensitive to storm viewing angle and to distance between storm and radar. The sensitivity of the CII and SSI to range but not viewing angle suggest that they may have some use in characterizing the nature of the profiles within hurricanes. However, it must be emphasized that any conclusions stated here must be considered very preliminary, subject to further testing and rumination. Quite obviously, there is still much to be done in utilizing synthetic data to evaluate hurricane diagnostic tools.

## ACKNOWLEDGEMENTS

We are very grateful to Vincent Wood and Rodger Brown for their efforts in first developing their very nice hurricane model and then providing us with model data. In addition, we wish to thank Paul Desrochers for his technical assistance in the preparation of this paper.

## REFERENCES

- Brown, R.A., and L.R. Lemon, 1976: 17th Conf. on Radar Meteor. 104-109.  
 Donaldson, R.J., Jr., 1989: Potential - Vortex Fit. This volume.  
 Donaldson, R.J., Jr., and F.I. Harris, 1984: 22nd Conf. on Radar Meteor. 514-519.  
 Donaldson, R.J., Jr., and F.I. Harris, 1988: J. Atmos. Oceanic Technol. (In press)  
 Donaldson, R.J., Jr., and F.H. Ruggiero, 1986: 23rd Conf. on Radar Meteor. 236-239.  
 Ruggiero, F.H. and R.J. Donaldson, Jr., 1987: 17th Conf. on Hurr. and Trop. Meteor. 178-181.  
 Wood, V.T. and R.A. Brown, 1987: 17th Conf. on Hurricanes and Trop. Meteor., 174-177.

P9.22

## Features Resembling Single-Doppler Vortex Signatures Observed in an Extratropical Cyclone

Frank H. Ruggiero

Air Force Geophysics Laboratory  
Hanscom AFB, MA

Ralph J. Donaldson Jr.\*

ST Systems Corporation  
Lexington, MA

### 1. INTRODUCTION

On 12 February 1988 from 0000 to 2200 UTC the Air Force Geophysics Laboratory (AFGL) Doppler weather radar observed a significant winter storm that passed through the New England region. For approximately 3.5 hr during the passage of the storm unusual features were noticed in the Doppler velocity Plan-Position Indicator (PPI) displays. These unexpected features took the form of velocity couplets of relatively weak but significant azimuthal shear resembling to some extent single-Doppler vortex signatures. The purpose of this paper is to provide a detailed description of the velocity features observed and suggest a possible interpretation of the physical process producing them.

### 2. RADAR OBSERVATIONS

The AFGL radar is located in Sudbury, Massachusetts (42.40°N, 71.48°W) and operates at a wavelength of 11.07 cm. During the observations described in this paper the radar operated with a maximum range of 115 km and a maximum unambiguous velocity of 27.65 m·s<sup>-1</sup>. The radar scanned at 0.5°, 1.5°, 2.5°, 3.5°, and 4.5° elevation angles.

The unique velocity features mentioned above were initially noticed at approximately 1630 UTC at the elevation angles of 0.5° and 1.5°. An example of the appearance of these features in the Doppler velocity PPI display is given in Figure 1. It can be seen that there is a pronounced inbound maximum located to the southeast of the radar. This is the result of the strong flow of warm moist air being advected from the south, which is typical when a surface low is located off the Mid Atlantic coast. The corresponding outbound velocity which would be expected to be found approximately 180° from the inbound maximum, if this southeast flow continued across and beyond the radar, does not

show up here because there is insufficient signal return at the corresponding range toward the northwest. The feature that makes the display interesting is the smaller area of minimum inbound velocity located to the westsouthwest of the maximum. There is no corresponding feature found on the opposite side of the display. This display is analogous to what would be seen when viewing a mesocyclone, with two important exceptions: 1) the shear is much weaker than minimal mesocyclonic shear; it is only on the order of 10<sup>-3</sup> to 10<sup>-4</sup> s<sup>-1</sup> and 2) in this example and in almost all the other observations of the velocity features there were no actual outbound velocities, just minimum inbound velocities. Eventually these features were visualized at all five of the elevation scanning angles. The features continued to be seen on the Doppler velocity PPI displays until approximately 1900 UTC.

Even though no actual outbound velocities were noted, the features might still be interpreted as vortex signatures if you consider the translation effect of the storm movement. An attempt was made to account for the storm motion by tracking some of the reflectivity features during the passage of the storm. A rough estimate derived from tracking reflectivity features around 1800 UTC resulted in an approximate storm motion of 22 m·s<sup>-1</sup> toward 15°. When subtracting this vector from the maximum and minimum inbound radial velocities in Figure 1 the result is an inbound velocity of -15 m·s<sup>-1</sup> and an outbound velocity of 17 m·s<sup>-1</sup>. Thus, from the frame of reference of the storm, the velocity features could actually represent a vortex signature.

In order to track the velocity features in time and space, locations for the center of maximum and minimum inbound velocities at each observation were defined. This was accomplished in a semi-objective method of subjectively locating the radial velocity contour that was 1 or 2 m·s<sup>-1</sup> above or below the respective minimum or maximum velocity feature. The location of the center of the contours was then estimated

\*Supported by AFGL contract No.  
F19628-87-C0124.

objectively by using velocity weighted averaging within the contours. From the period 1630 to 1830 UTC 45 of the maximum inbound features were located in this way while 47 of the minimum inbound features were identified. It should be noted that there is more inherent uncertainty in the position estimations for the maximum inbound velocities as compared to the minimum inbound velocities. This is because the maximum inbound velocity peaks were generally more rounded than the sharply defined peaks of the minimum inbound velocities.

During the observation of the velocity features they showed a general movement toward the radar. There is, however, an interesting development that occurred with both the maximum and

minimum features at 0.5° and 1.5° elevations. At particular times they seemed to jump back in range. That is, the features were moving closer to the radar and then they seemingly would all of a sudden be at least 20 km farther out than where they were in the previous volume scan. This was observed at 1712 UTC for the minimum inbound velocities and at approximately 1730 UTC for the maximum inbound velocities. After the jump back the features again continued to move closer to the radar. Corresponding to inward movement of the minimum inbound features before 1712 UTC was a westerly component. After 1712 UTC there was an easterly component to the movement of this feature. Throughout the entire observation time the maximum inbound

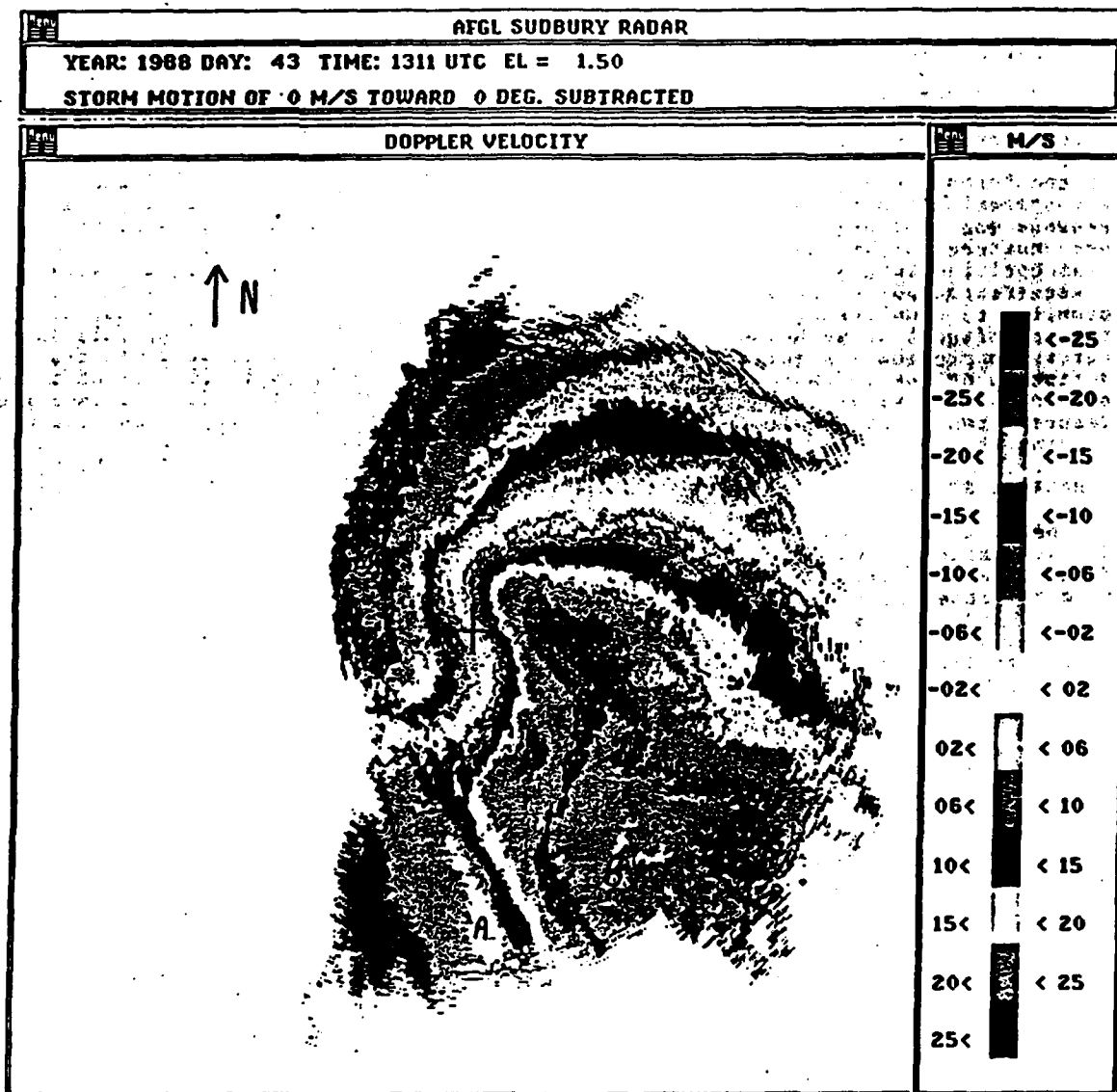


Figure 1. Doppler velocity Plan-Position Indicator display for 1811 UTC 12 February 1988. The cross in the center of the display is the location of the radar site. The letter A indicates the position of the minimum inbound Doppler velocity of  $-4 \text{ m} \cdot \text{s}^{-1}$  and B shows where the maximum inbound velocities of  $-33 \text{ m} \cdot \text{s}^{-1}$  are located.

features showed a general easterly component to their movement.

To observe the vertical structure of these features, consecutive observations at sequential elevation angles were compared. There were 23 cases for each of the minimum and maximum inbound velocity features where they could be tracked at sequential elevation angles. The average slope of the minimum inbound velocity was  $3.2^\circ$  above horizontal with the higher feature located on the average at an azimuth angle of  $284^\circ$  with respect to the lower feature. The average slope of the maximum inbound velocity was  $14.1^\circ$  above horizontal with the higher feature located on the average at an azimuth angle of  $330^\circ$  with respect to the lower feature. It should be mentioned, however, that there was much scatter in the slope data for both the minimum and maximum inbound velocity features.

### 3. DISCUSSION

Initially, upon observing the velocity features the authors thought that they might be looking at the center of circulation of the storm. However, review of the synoptic analysis of the period in question showed that the low center was located off the New Jersey coast, which is well out of the viewing range of the radar. The surface synoptic analysis at 1800 UTC showed the presence of a trough line that extended out of the low pressure center northeastward to cut across Cape Cod and follow the New England coast into Maine (dashed line on Figure 2). At 2100 UTC a developing stationary front was analyzed in approximately the same place as the trough had been located three hours previously. The synoptic conditions preceding the passage of the storm indicated that coastal front development as described by Bosart (1975) was possible. It would seem that the occurrence of the velocity features and the development of the coastal front at approximately the same time and location would indicate they are in some way related.

Just how the velocity features and the coastal front are related is not exactly clear. The velocity PPI display itself would suggest some sort of circulation. Although the maximum and minimum inbound velocity features do not lie over the surface trough (Figure 2) the azimuth angle of sloping of the features tends to be approximately normal to the trough line. The velocity features could be thought of as a signature of the flow on either side of the trough at the point within radar range where the flow on each side of the trough comes closest to being parallel to the radar beam. There are two problems, however, with this simple description. First, the orientation of the velocity features would seem to indicate an upper-level trough that is not parallel to the surface trough, and second, the narrowness of the inbound minimum indicates it is more locally concentrated than the broad flow one would expect to

find on the cold side of the trough.

In the case study presented in his paper Bosart (1975) reported that the coastal front was preceded by cyclonic relative vorticity and pressure troughing at the surface. In fact, in that particular case small circulation centers developed ahead of the main low (Bosart et al., 1972). Therefore a more elaborate explanation could be that the radar is observing a wave moving along the developing frontal zone. The surface analysis made during the time the velocity features were observed showed no indication of surface waves. However, the data resolution in the synoptic analysis is very coarse when compared with the resolution of the radar features. The presence of a wave could explain the relative position and orientation of the velocity features with respect to the analyzed trough line. A possible outline of the shape of the wave is denoted by the dotted line in Figure 2. It also should be noted that the motions of the maximum inbound features during all the observations and the minimum inbound features after 1712 UTC are consistent with a wave moving northeastward along the coastal front.

If indeed the features viewed in the velocity display are part of the coastal

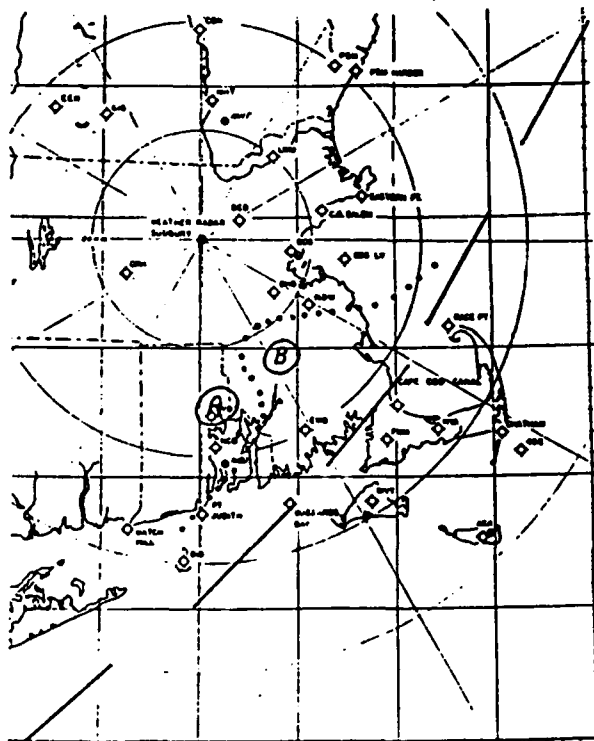


Figure 2. General depiction of the surface analysis and radar information for approximately 1800 UTC 12 February 1988. The long dashed line represents the position of the trough line as redrawn from the 1800 UTC surface analysis. A and B indicate the positions of the minimum and maximum inbound velocities respectively at 1811 UTC taken from Figure 1. The dotted line represents the possible location of a wave producing the observed velocity features.

front formation it is highly significant because previous work (Bosart, 1975) had indicated that it was just a boundary layer phenomenon. The average height of the velocity features observed was 2.43 km, which is well above the boundary layer.

#### 4. SUMMARY

To the authors' knowledge this is the first time that this type of velocity feature has been reported in association with coastal frontogenesis. Although the exact physical description of the process taking place is somewhat uncertain, the favored hypothesis at the moment is that the radar is viewing a wave that is moving along the developing frontal zone. Needless to say the short term forecast value of being able to detect the formation of a coastal front and the locations of pockets of cold and warm air during the passage of coastal winter storms is significant. Not only is the knowledge of the snow-rain line important but, as Bosart (1975) mentioned, the heaviest precipitation often occurs not far from the frontal zone on the cold side.

On 1 November 1988 another coastal storm was observed by the AFGL weather radar with the same type of features, only this time more pronounced. It is hoped that this and other future cases along with possible dual-Doppler studies would result in a more definitive explanation of the physical processes being viewed.

#### ACKNOWLEDGEMENTS

The authors would like to express their appreciation to the engineering and technical staff of the Ground Based Remote Sensing Branch of AFGL who are instrumental in keeping the radar and data processing equipment in excellent working order. In particular the authors would like to thank Graham Armstrong who showed the good sense to ride out the storm and keep the radar running while the rest of us tried to leave during the height of the storm with 20 cm of unplowed, wet snow in the parking lot.

#### REFERENCES

- Bosart, L.F., 1975: New England coastal frontogenesis. Quart. J. Roy. Meteor. Soc. 101, 957-978.
- Bosart, L.F., C.J. Vaudo, and J.H. Helsdon, 1972: Coastal frontogenesis. J. Appl. Meteor. 11, 1236-1258.